Accepted 14 Dec 1999 to The Astrophysical Journal Supplement Series
Preprint typeset using LaTeX style emulateapj

CALIBRATION OF NEBULAR EMISSION-LINE DIAGNOSTICS: I. STELLAR EFFECTIVE TEMPERATURES

M. S. Oey
Space Telescope Science Institute, 3700 San Martin Drive, Baltimore, MD 21218, USA; oey@stsci.edu
M. A. Dopita
Research School of Astronomy and Astrophysics, Institute of Advanced Study, The Australian National University, Private Bag, Weston Creek P.O., ACT 2611, Australia; mad@mso.anu.edu.au.
J. C. Shields
Ohio University, Dept. of Physics and Astronomy, Clippinger Research Labs. 251B, Athens, OH 45701-2979, USA; shields@helios.phy.ohiou.edu
R. C. Smith
Cerro Tololo Inter-American Observatory[1], Casilla 603, La Serena, Chile; csmith@noao.edu

Accepted 14 Dec 1999 to The Astrophysical Journal Supplement Series

ABSTRACT

We present a detailed comparison of optical H II region spectra to photoionization models based on modern stellar atmosphere models. We examine both spatially resolved and integrated emission-line spectra of the H II regions DEM L323, DEM L243, DEM L199, and DEM L301 in the Large Magellanic Cloud. The published spectral classifications of the dominant stars range from O7 to WN3, and morphologies range from Strömgren sphere to shell structure. Two of the objects include SNR contamination. The overall agreement with the predictions is generally within 0.2 dex for major diagnostic line ratios. An apparent pattern in the remaining discrepancies is that the predicted electron temperature is ~ 1000 K hotter than observed. [Ne III] intensities are also slightly *over*predicted, which may or may not be related. We model the shock emission for the SNR-contaminated objects, and find excellent agreement with the observations for composite shock and photoionized spectra. DEM L301's emission apparently results from both shocks and density-bounded photoionization. The existence of contaminating shocks can be difficult to ascertain in the spatially integrated spectra.

Our analysis of the complex DEM L199 allows a nebular emission-line test of unprecedented detail for WR atmospheres. Surprisingly, we find no nebular He II $\lambda4686$ emission, despite the fact that both of the dominant WN3 stars should be hot enough to fully ionize He I in their atmospheres. The nebular diagnostics are again in excellent agreement with the data, for stellar models not producing He^+-ionizing photons. The optical diagnostics are furthermore quite insensitive to the ionizing energy distribution for these early WR stars.

We confirm that the η' emission-line parameter is not as useful as hoped for determining the ionizing stellar effective temperature, $T_\star$. Both empirically and theoretically, we find that it is insensitive for $T_\star \gtrsim 40$ kK, and that it also varies spatially. The shock-contaminated objects show that η' will also yield a spuriously high $T_\star$ in the presence of shocks. It is furthermore sensitive to shell morphology. We suggest [Ne III]/Hβ as an additional probe of $T_\star$. Although it is abundance-dependent, [Ne III]/Hβ has higher sensitivity to $T_\star$, is independent of morphology, and is insensitive to shocks in our objects. These observations should be useful data points for a first empirical calibration of nebular diagnostics of $T_\star$, which we attempt for LMC metallicity.

Subject headings: galaxies: ISM — H II regions — Magellanic Clouds — stars: fundamental parameters — stars: Wolf-Rayet — supernova remnants

1. INTRODUCTION

Extragalactic H II regions are a vital probe of physical conditions in distant star-forming regions. The luminosities and distribution of H II regions are widely used to infer the magnitude and distribution of massive star formation. Likewise, the ratios of prominent emission lines in nebular spectra are commonly used as diagnostics to infer properties such as chemical abundances, gas density, electron temperature, and characteristics of the ionizing stellar population. The emergent nebular spectrum depends primarily on three parameters: stellar ionizing effective temperature ($T_\star$), ionization parameter (U), and metal abundance (Z). Hence, we need adequate constraints on two of these quantities to estimate the third. In practice, all three parameters are relatively complicated to obtain accurately, especially in distant extragalactic H II regions. Nebular photoionization codes (e.g., reviewed by Ferland et al. 1995) are therefore extensively used to interpret the observed emission-line spectra and constrain these properties. Yet, in spite of our heavy dependence on such codes, there has been little comparison of model H II regions with spatially resolved, spectrophotometric observations of objects having clearly determined stellar ionizing sources. The prototypical H II region for such comparisons is the Orion nebula (e.g., Baldwin et al. 1991; Walter

[1]National Optical Astronomy Observatories, operated by the Association of Universities for Research in Astronomy, Inc., under cooperative agreement with the National Science Foundation

et al. 1992), and studies of planetary nebulae (e.g., Liu & Danziger 1993) have also been useful in this regard. However, there have been almost no studies exploring the parameter space of ordinary H II regions with known stellar ionizing sources.

This omission is due primarily to the difficulty in determining accurate nebular parameters in Galactic H II regions, which suffer from large and variable extinction, distance uncertainties, and line-of-sight confusion. The problem is compounded by large angular size, and similar difficulties in obtaining reliable and complete stellar censuses for these regions. However, at a distance of ~ 50 kpc, the Large Magellanic Cloud (LMC) offers a great variety of H II regions that subtend a few arcminutes, are at a well-determined distance, and have low foreground extinction. For many of these nebulae, the associated massive star population has been examined in detail and the dominant stars classified with spectroscopic observations (e.g., Massey et al. 1995; Oey 1996a). We have therefore exploited these conditions to examine the emission-line diagnostics of four bright, LMC H II regions with respect to their known properties. The angular sizes are small enough that we are able to obtain spatially integrated observations by scanning a long slit across the objects, thereby reproducing observations of spatially unresolved H II regions in more distant galaxies. We have also obtained unscanned, spatially-resolved observations. Together, these data will clarify the dominant effects that are relevant to interpreting spatially unresolved observations, and test how well photoionization models reproduce actual nebular conditions. In this paper, we present the observations and examine the nebular diagnostic line ratios with respect to the stellar ionizing sources. A companion paper (Oey & Shields, in preparation; Paper II) will examine the diagnostics with respect to the chemical abundances.

We mentioned above that H II region emission-line spectra are determined primarily by the three parameters, $T_\star$, U, and Z. In practice, there are complicating factors associated with each of these. In the case of $T_\star$, the main problem is uncertainty in the actual energy distribution emitted in the Lyman continuum; we discuss this in greater detail below. With respect to U, the nebular density, morphology, and geometric relation to the ionizing stars will significantly affect the ionization parameter across the nebula. We will examine this effect in both this work and in Paper II. Finally, complications for Z are primarily ionization correction factors and variations in elemental ratios. Issues affecting the abundance determinations will be addressed primarily in Paper II.

2. OBSERVATIONS

In order to empirically explore the $T_\star$ parameter space, we selected LMC H II regions whose spectral types vary from O7 to WN3. The sample is summarized in Table 1: column 1 identifies the object from the Davies, Elliott, & Meaburn (1976; DEM) Hα catalog of the LMC; column 2 gives the corresponding identification from the Henize (1956) catalog; column 3 lists the ionizing Lucke & Hodge (1970) OB association; column 4 identifies the dominant ionizing stars; column 5 gives the corresponding spectral types; and column 6 gives the reference for the star ID and spectral types. Figures 1*a* – 4*a* show the Hα CCD images of the sample objects, obtained with the CTIO/U. Michigan 0.6/0.9-m Curtis Schmidt Telescope as part of the Magellanic Clouds Emission-Line Survey (Smith et al. 1998). Panels *b* and *c* of the same figures show the continuum-subtracted ratio maps of [O III]λ5007/Hα and [S II]λ6724/Hα, with darker regions corresponding to higher values. The spatial resolution of the images is 2.3″ px^{-1}.

As can be seen in the figures, the sample also includes a range of nebular morphology: DEM L323 (Figure 1) has beautiful, spherical morphology, and can be seen to be emerging from a neutral cocoon; DEM L243 (Figure 2) shows a slightly more irregular morphology, but with no apparent shells or filaments; DEM L199 (Figure 3) has a complex morphology that is a composite of large blobs, filaments, and shell structure; and DEM L301 (Figure 4) shows a strongly filamentary shell structure. To constrain the role of morphology, we chose DEM L323 for its "classical", spherical, Strömgren sphere morphology, in contrast to the extreme shell structure of DEM L301, while maintaining the same O3 spectral type for the ionizing stars.

Embedded or superimposed supernova remnants (SNRs) can strongly affect the emission-line properties in a predominantly photoionized H II region (e.g., Peimbert, Sarmiento, & Fierro 1991). Since the massive stars that ionize these nebulae expire as core-collapse supernovae, we do expect such associated SNRs to occasionally be found in H II regions. DEM L243 encompasses a well-known SNR (e.g., Shull 1983; Westerlund & Mathewson 1966), whose spatial area is delineated by the black circle in Figure 2. This nebula will be used to study the effect of an SNR on the emission-line properties of the surrounding H II region. In addition, it is likely that DEM L301 also has had recent SNR activity (Chu & Mac Low 1990; Oey 1996b).

We obtained spectroscopic observations of the H II regions in the sample using the 2.3-m telescope at Siding Spring Observatory of the Australian National University. The data were obtained during the nights of 1997 January 2 – 4. The Double-Beam Spectrograph permitted simultaneous observations of the blue and red spectral regions, providing a total wavelength coverage over the range 3500 – 9200Å. The dispersing element was a 300 line mm^{-1} grating in the blue, and a 316 line mm^{-1} grating in the red, with the beam split by a dichroic centered at 6200Å. We recorded the data with two SITE 1752 × 532 CCDs, whose 15μ pixels yield a spatial resolution of 0.91″ px^{-1}, and spectral resolution of about 5.5Å. The long slit length of 6.′4 was well-suited to sizes of the targets, which subtend several arcminutes in diameter.

Our standard stars for flux calibration were EG 21 and LTT 4364 (Stone & Baldwin 1983; Hamuy et al. 1992); observing conditions were not strictly photometric. Total exposure times ranged between one and two hours, depending on target surface brightness, with individual frames exposed for 900 – 1200 s. We observed all objects in the sample with at least two stationary slit positions, and three of the four targets were also observed by scanning the slit across the nebula. In order to avoid irregularities in the scan rate, the rate was set such that the desired region was scanned in a single pass. The data were reduced

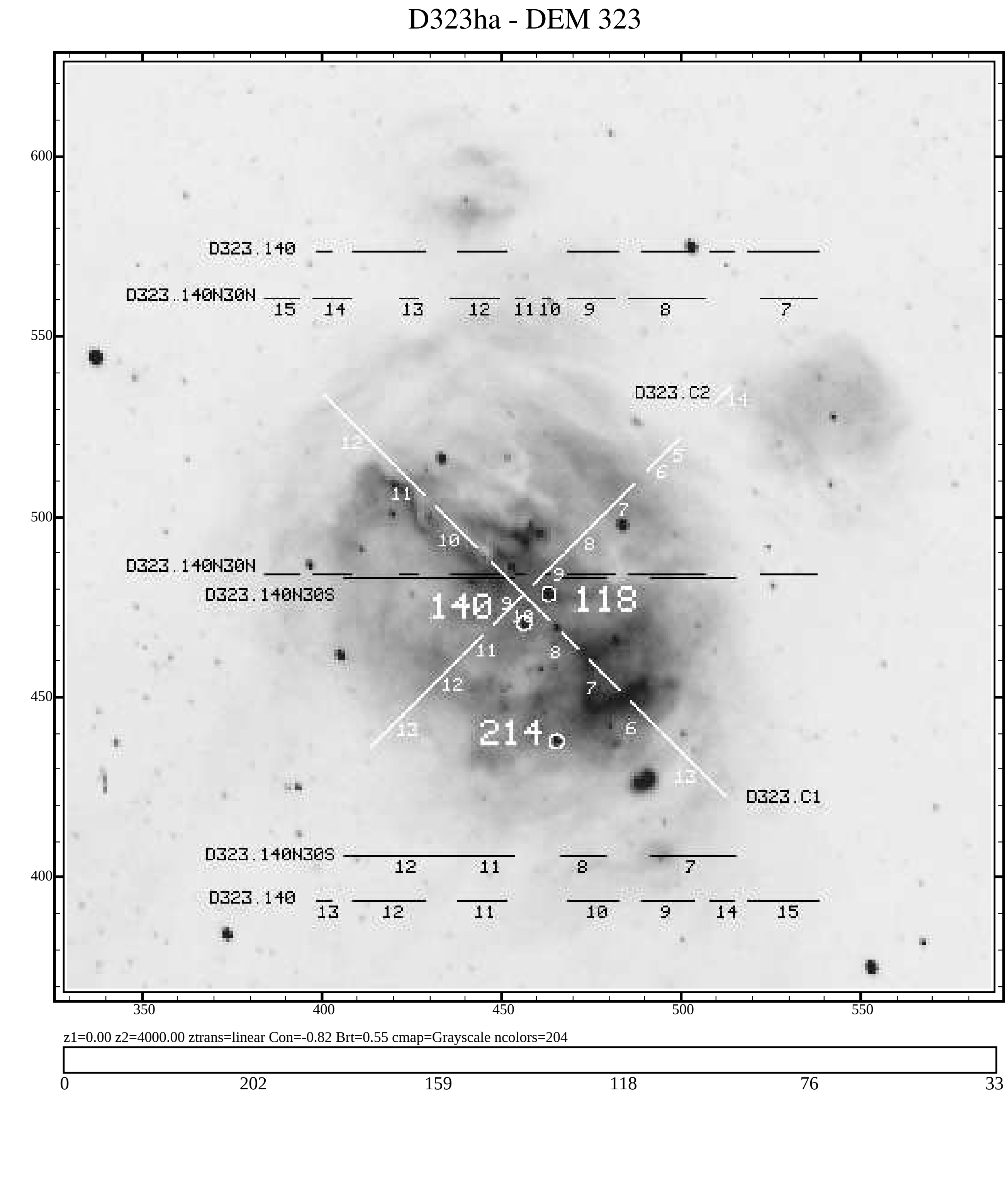

Fig. 1.— Hα image of DEM L323, with the dominant O3–4 stars identified. White lines indicate apertures on stationary slit positions and black lines show the end points of scans for scanned observations. North is up and east to the left. The pixel scale is marked along the edges, with 2.3″ px^{-1}. Panel *b* shows continuum-subtracted [O III]/Hα; panel *c* shows continuum-subtracted [S II]/Hα. The dominant stars are marked in each image.

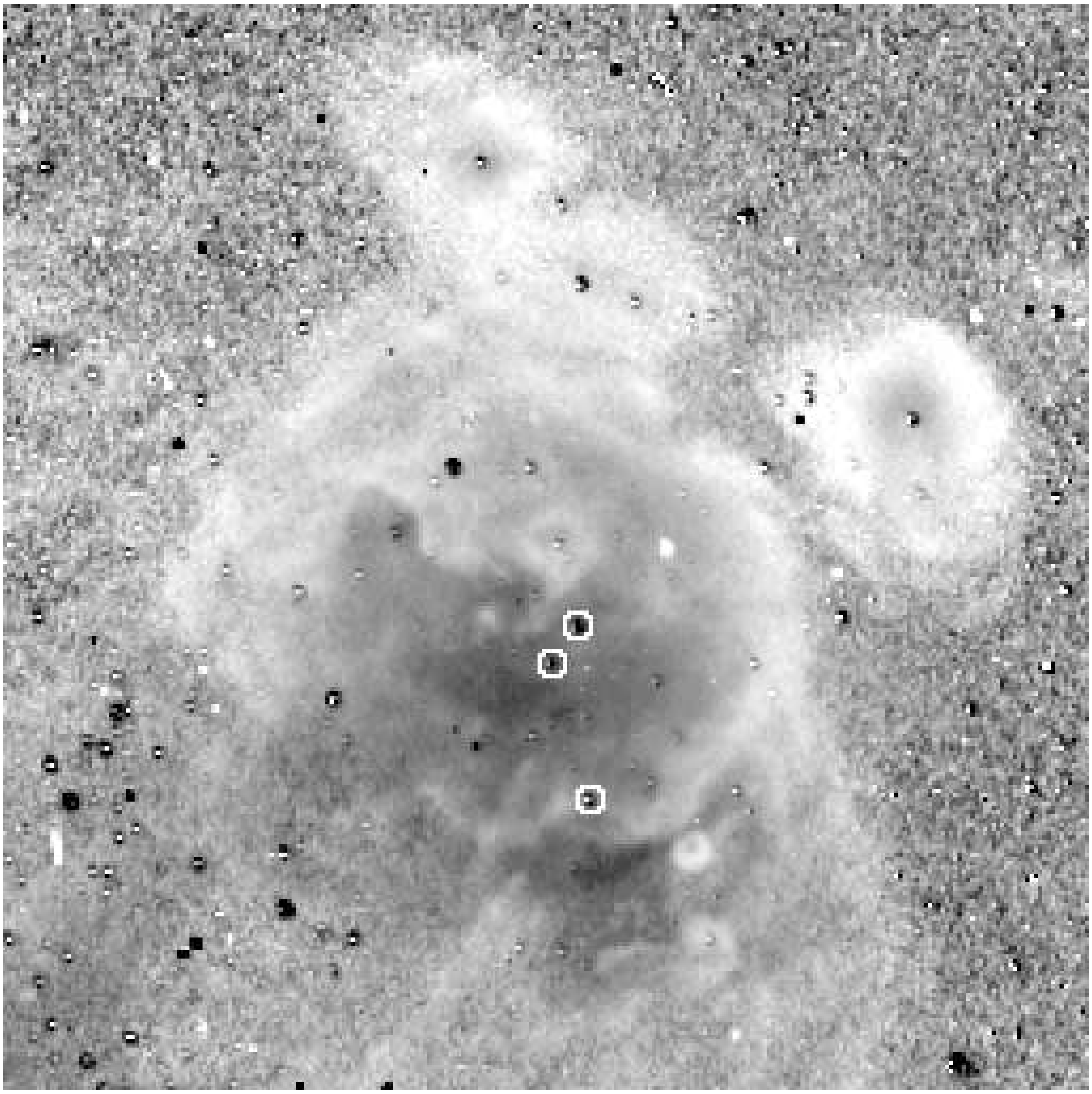

Fig. 1*b*.—

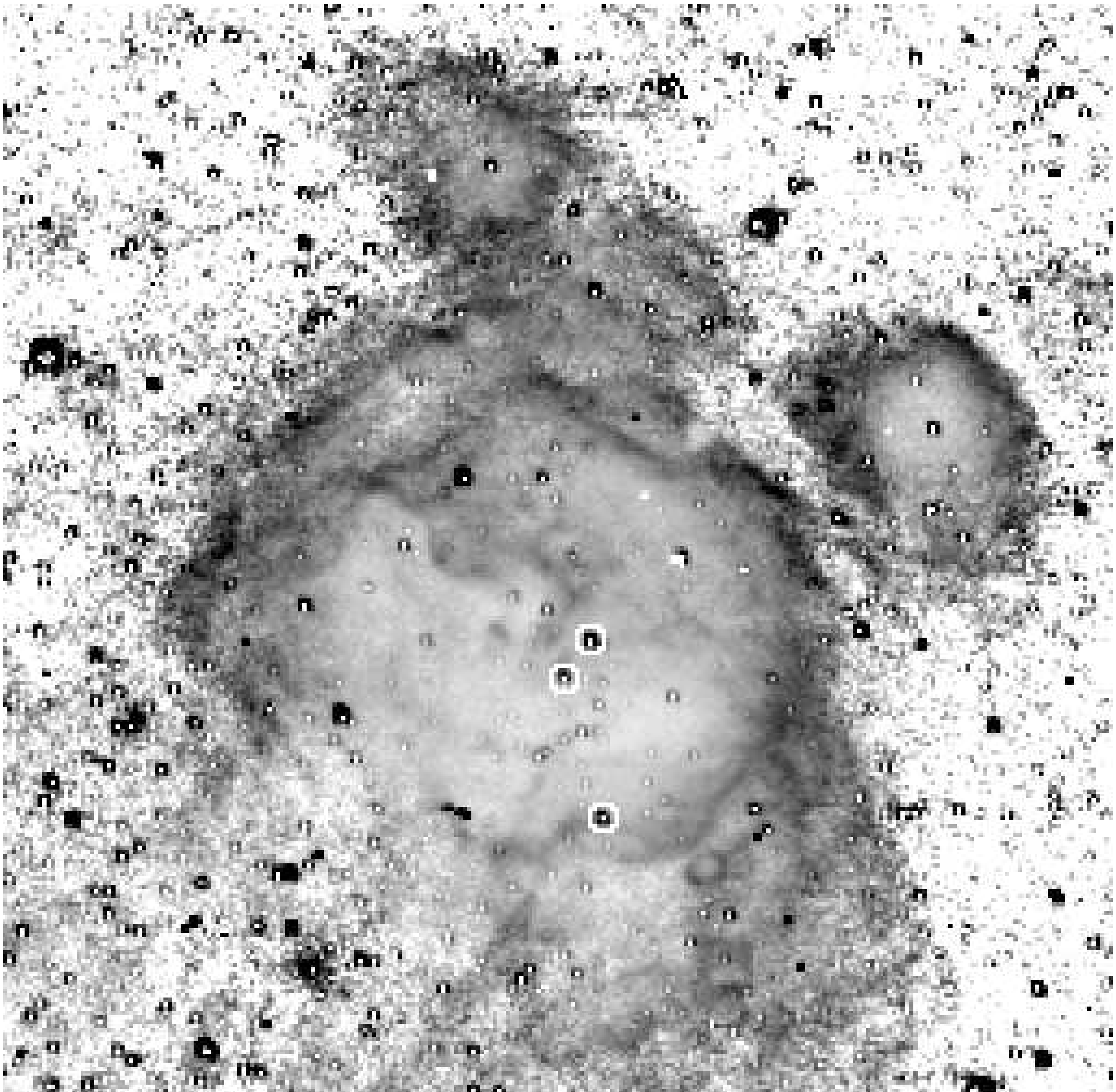

Fig. 1*c*.—

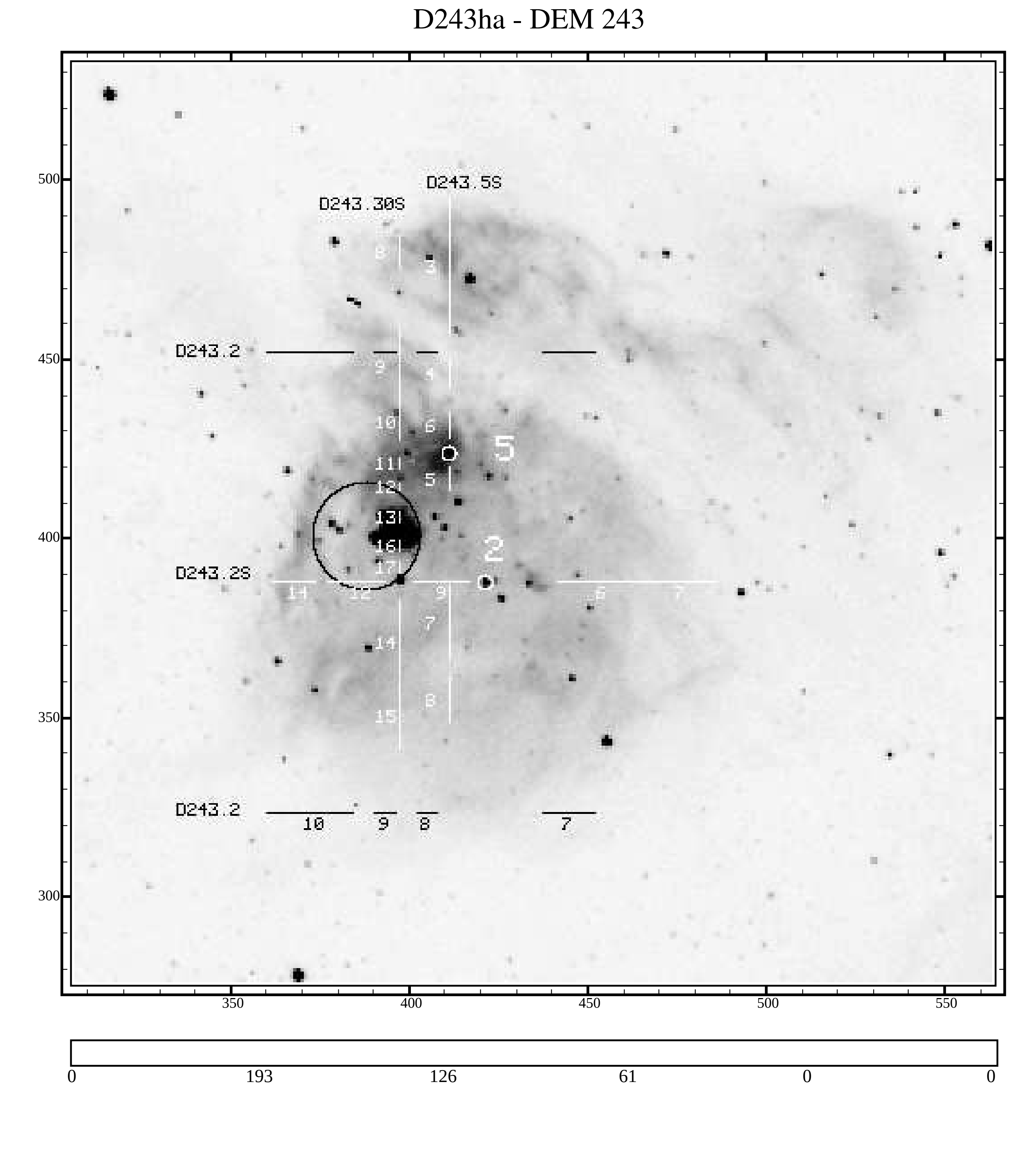

Fig. 2.— Hα image of DEM L243, with the dominant O7 stars identified. Line types are as in Figure 1. The black circle indicates the approximate boundary of the supernova blastwave seen in X-ray and radio continuum. Panel b shows continuum-subtracted [O III]/Hα; panel c shows continuum-subtracted [S II]/Hα.

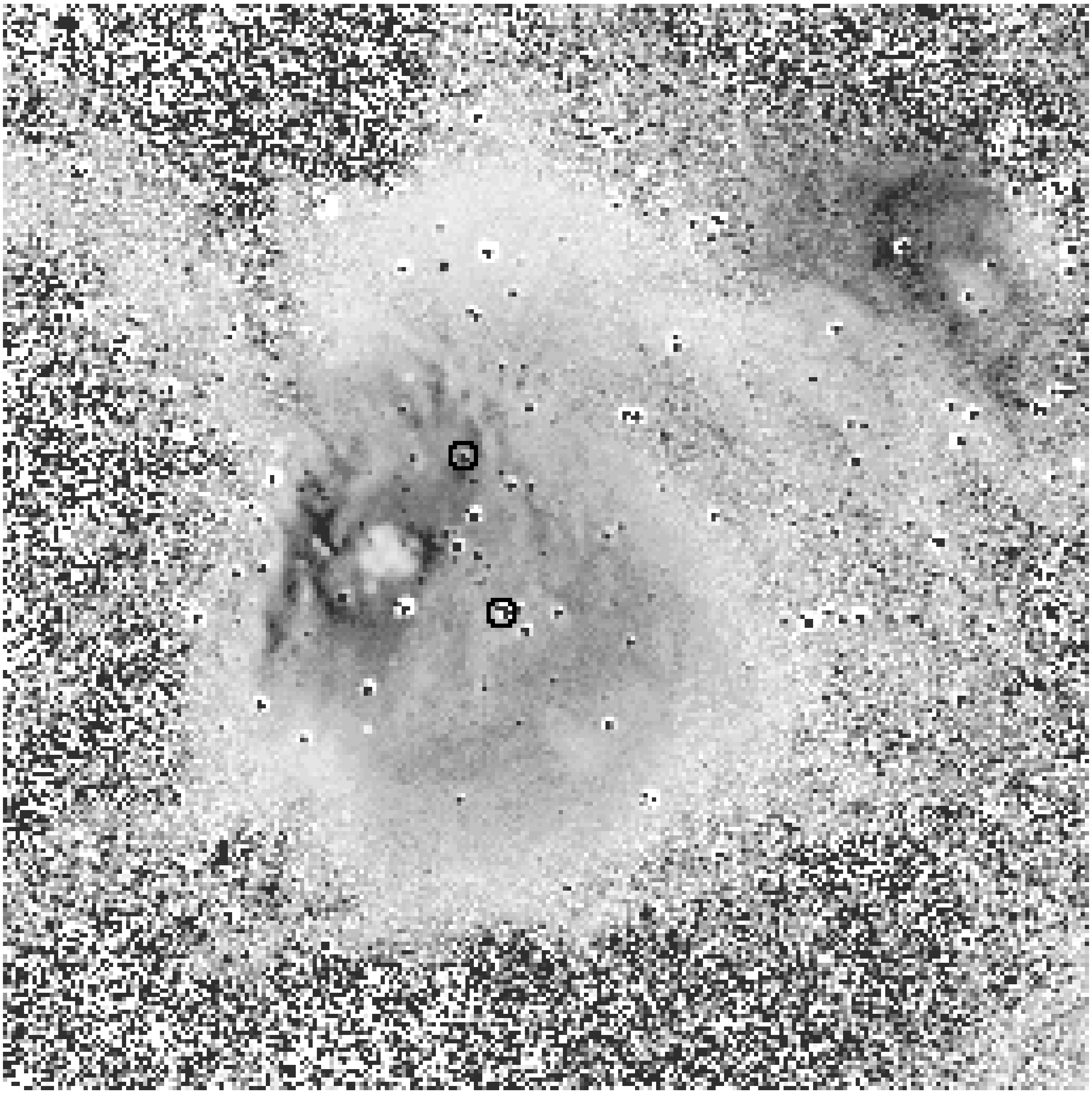

Fig. 2*b*.—

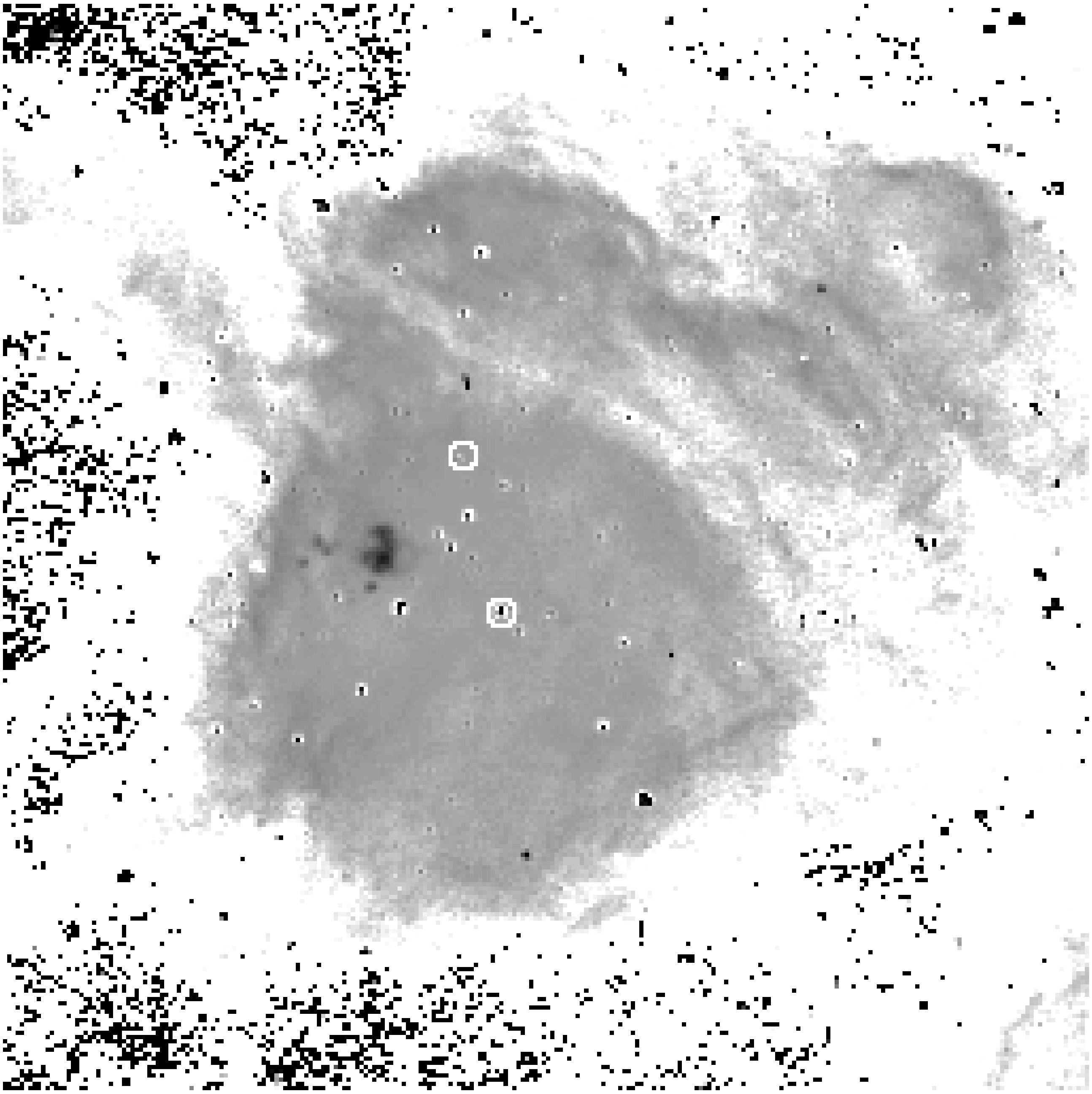

Fig. 2*c*.—

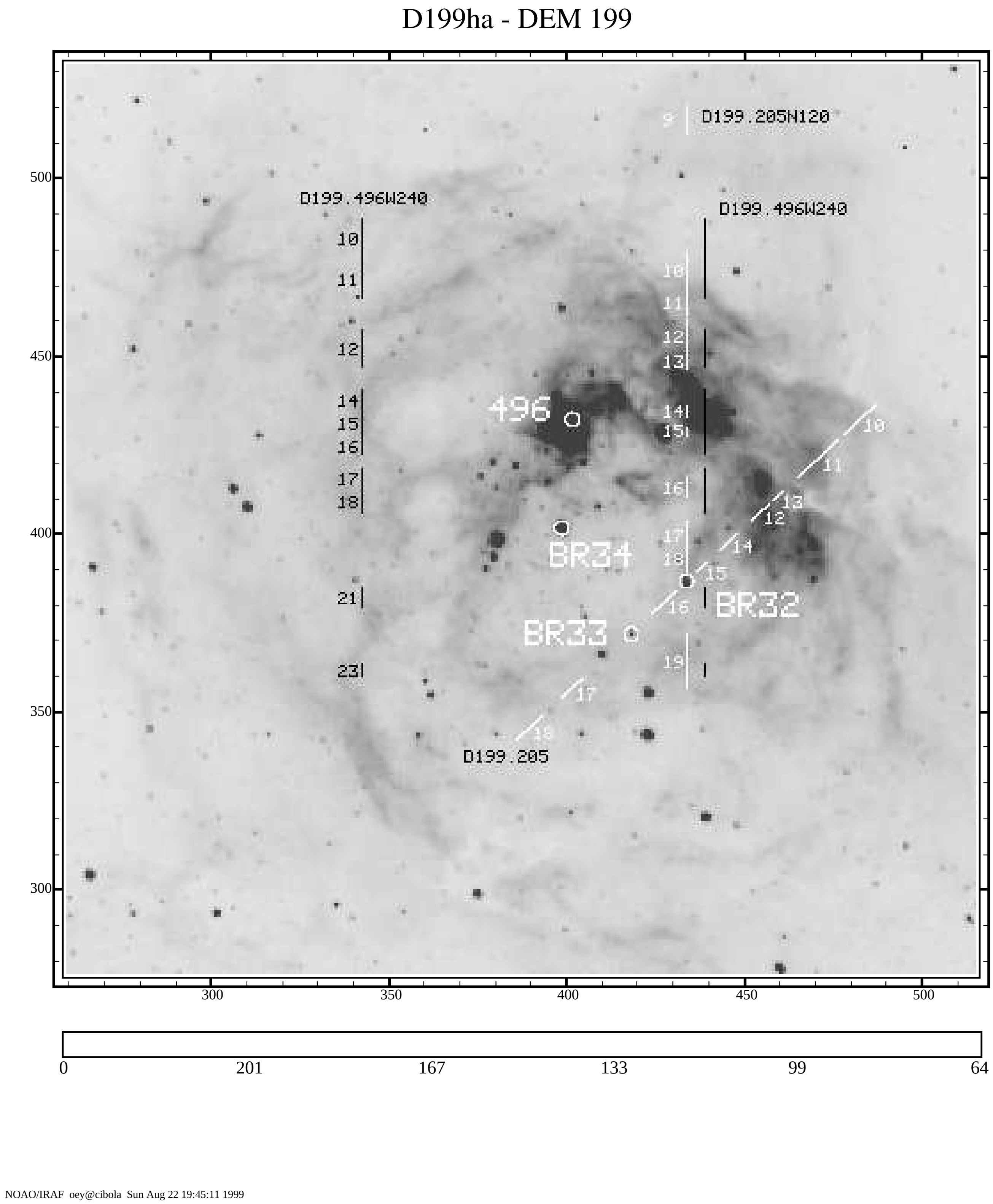

Fig. 3.— Hα image of DEM L199, with the dominant WR stars and O3–4 star identified (see Table 1). Line types are as in Figure 1. Panel *b* shows continuum-subtracted [O III]/Hα; panel *c* shows continuum-subtracted [S II]/Hα.

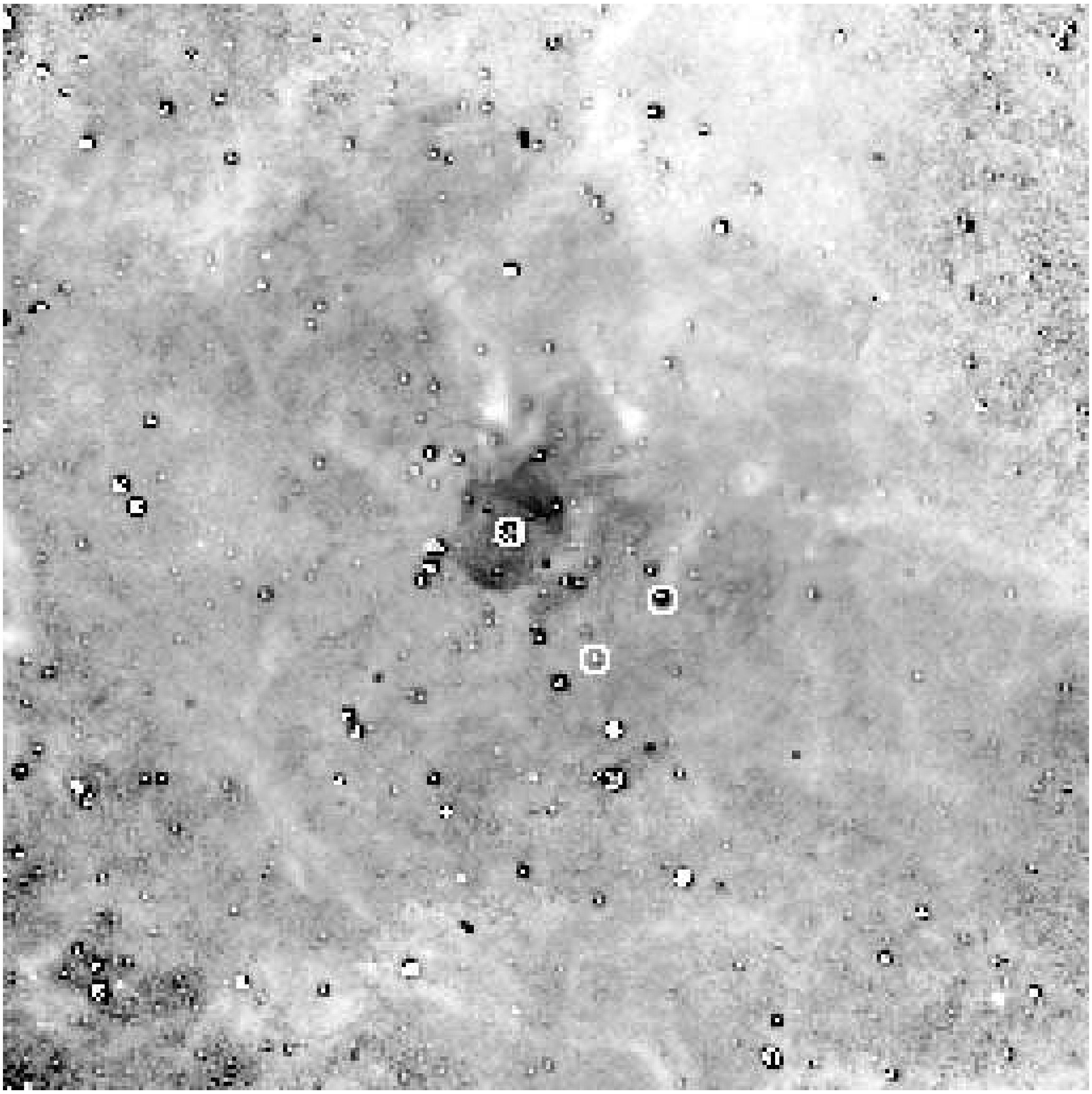

Fig. 3*b*.—

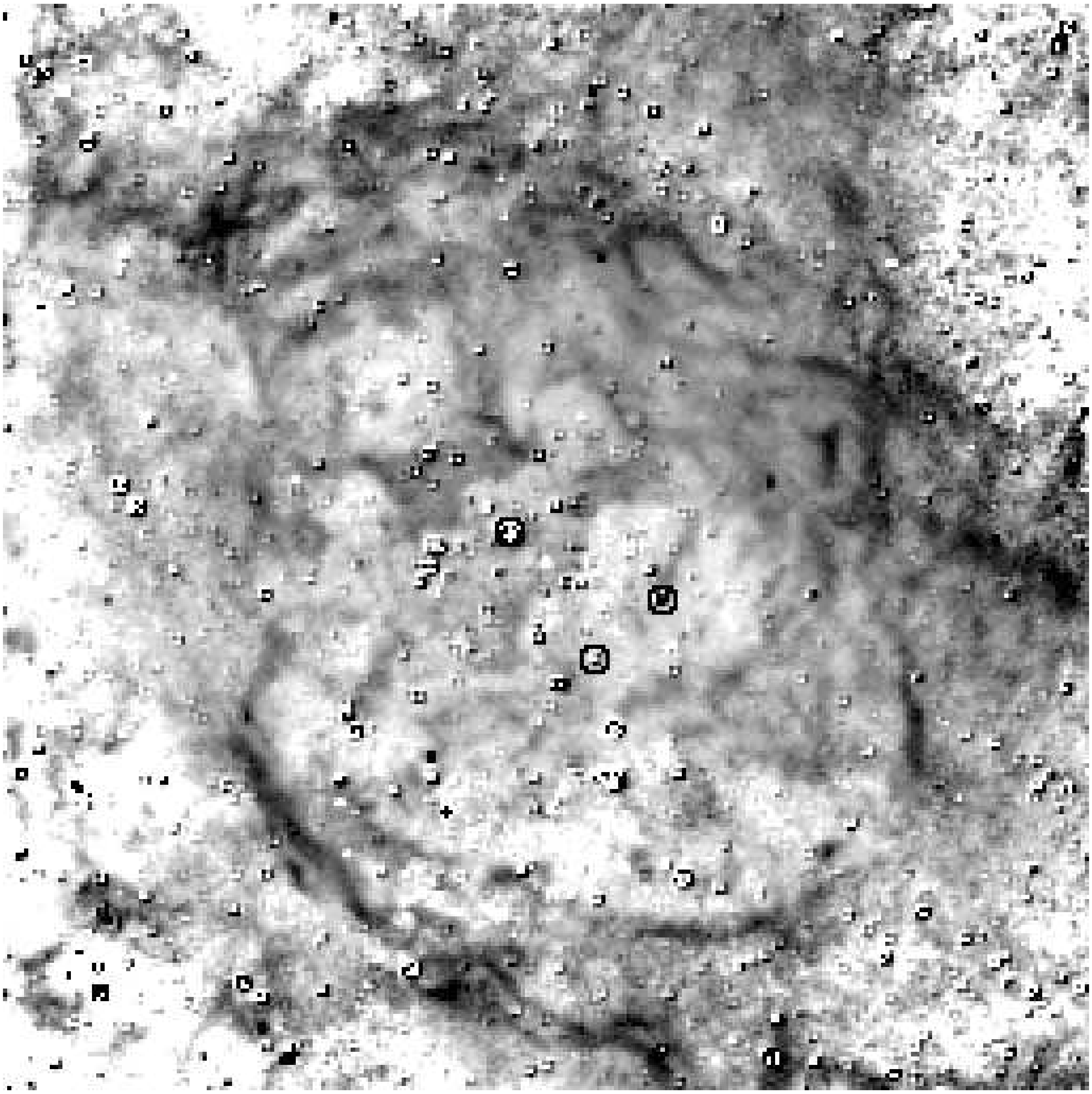

Fig. 3*c*.—

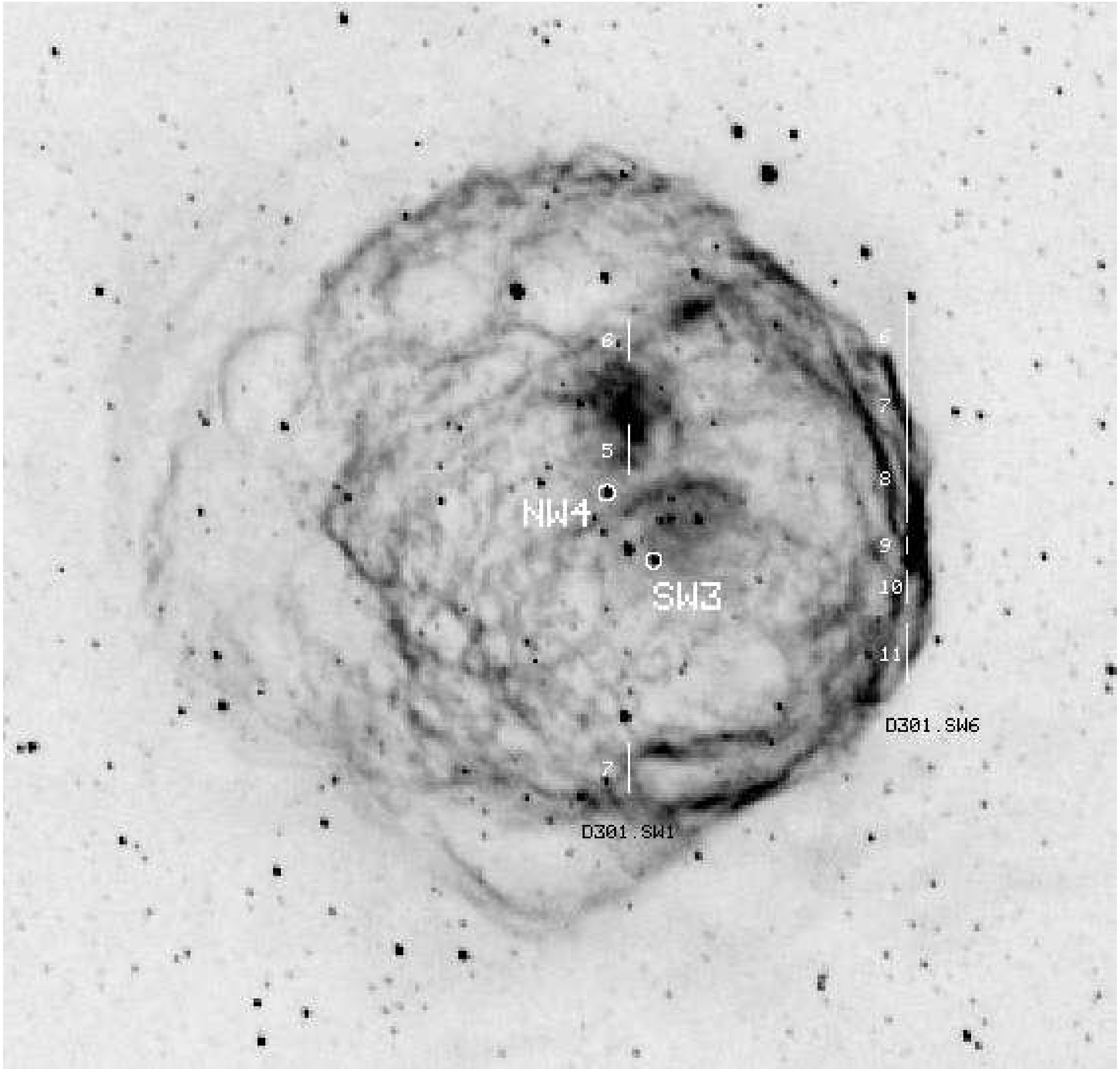

Fig. 4.— Hα image of DEM L301, with the dominant O3–5 stars identified. Line types are as in Figure 1. Panel *b* shows continuum-subtracted [O III]/Hα; panel *c* shows continuum-subtracted [S II]/Hα.

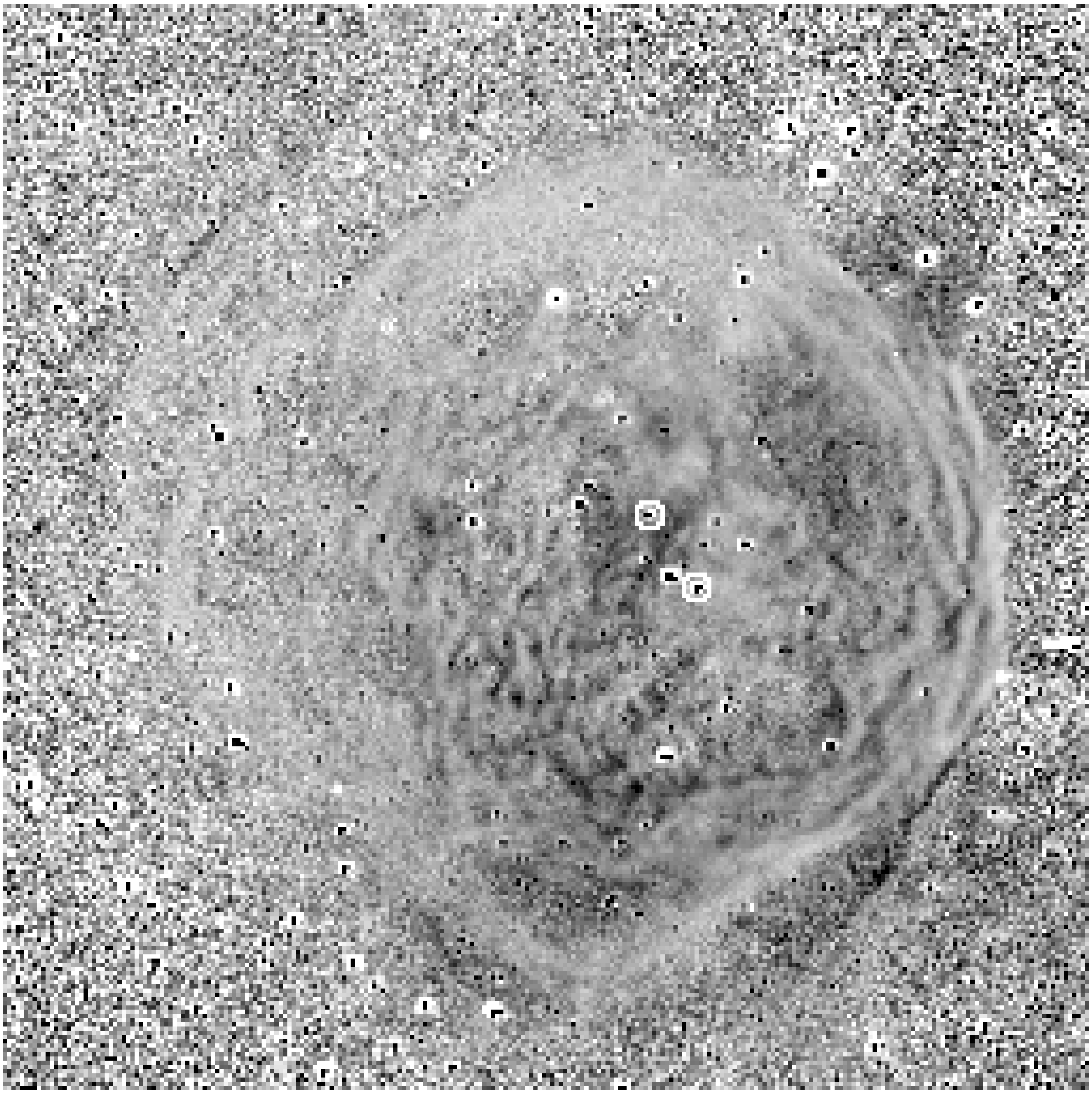

Fig. 4*b*.—

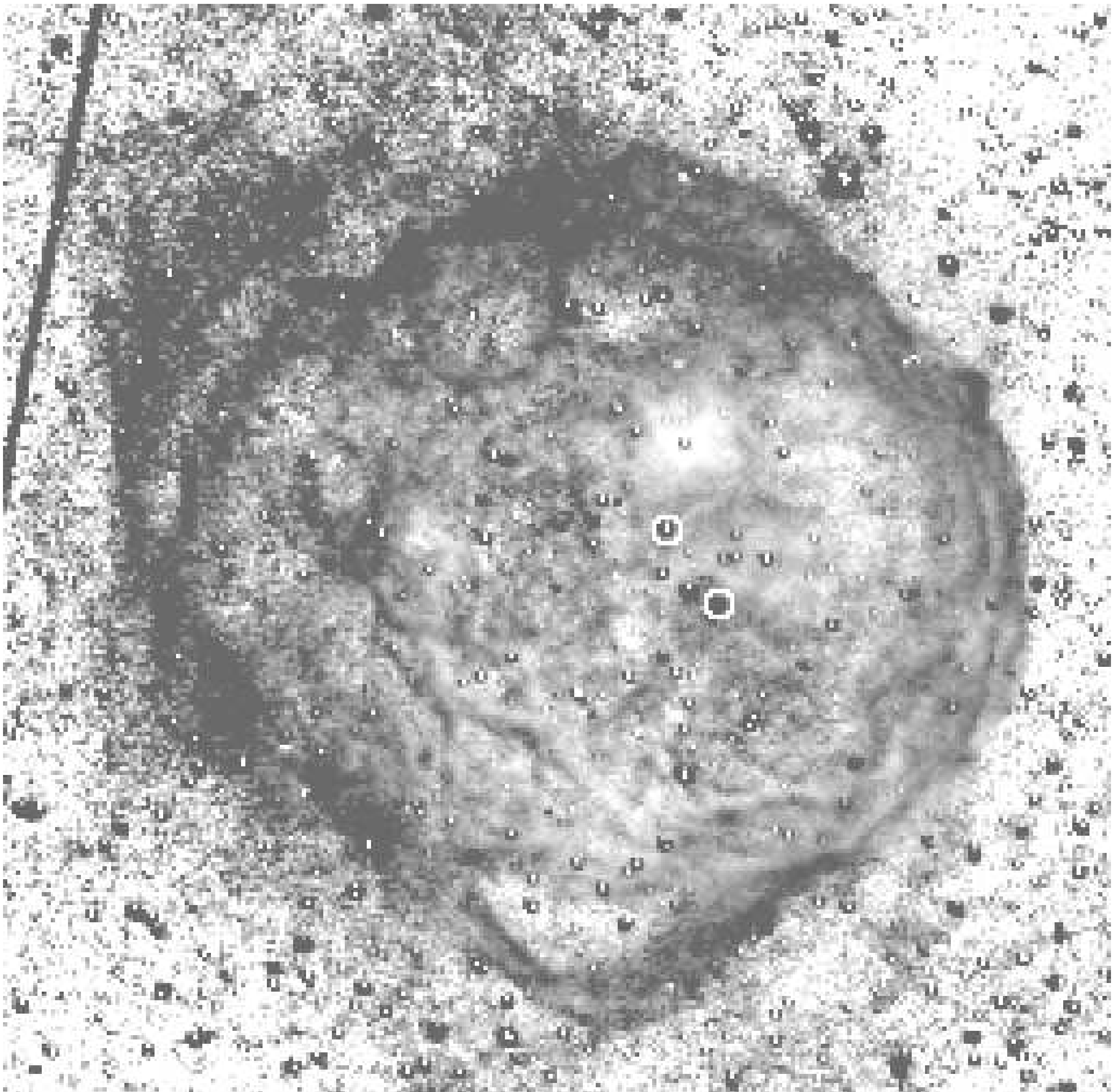

Fig. 4*c*.—

and extracted with IRAF[2] using standard longslit reduction techniques. Figures 1*a* – 4*a* show the slit positions of the observations; stationary positions are shown in white, and the endpoints of scanned positions are shown in black. The individual extracted apertures are indicated with their ID numbers. The scanned observations are integrated over the slit length where the nebular emission is detected, to produce a spectrum integrated over most of the nebular area, as described in § 4. All apertures extracted from the same slit observation had the background level determined from the same region. This corresponds to the lowest emission level in the aperture, and we caution that there is likely to be very low-level, diffuse nebular emission over these regions as well. This increases the uncertainty in background subtraction, but disproportionately affects the low ionization species.

For each extracted spectrum, we derived reddening corrections from the Balmer decrements Hα/Hβ, Hγ/Hβ, and Hδ/Hβ, and obtained a weighted mean correction c, where

$$\frac{I(\lambda)}{I(\mathrm{H}\beta)} = \frac{I_0(\lambda)}{I_0(\mathrm{H}\beta)}\ 10^{-c(f_\lambda - f_{\mathrm{H}\beta})} \quad . \qquad (1)$$

The ratios $\frac{I(\lambda)}{I(\mathrm{H}\beta)}$ and $\frac{I_0(\lambda)}{I_0(\mathrm{H}\beta)}$ are the observed and intrinsic line intensities with respect to Hβ, and f_λ and $f_{\mathrm{H}\beta}$ describe the reddening law, for which we adopt that of Savage & Mathis (1979). We then assigned three or four reddening zones for each object, based on the range of derived values. The adopted c for each aperture is then taken as that of the zone with the closest reddening value. These adopted reddenings are listed in Table 2 with the dereddened line intensities. Our adoption of the Galactic reddening law rather than LMC should not introduce significant errors; we note that an error of 0.05 in c corresponds to 4%, or < 0.02 dex difference across the interval Hβ to Hα.

We examined the possibility of contamination in the Balmer lines by absorption in underlying stellar continuum. This effect should be unimportant in the stationary slit positions, since the H II regions and stellar populations are fully resolved. However, the scanned observations include many stars. We treated these exactly as is done with observations of unresolved distant nebulae, and solved simultaneously for the reddening and a single absorption equivalent width (EW). The only observations that showed significant contamination by absorption were the scanned observations for DEM L243 and DEM L199. For DEM L199, we found an absorption EW of 2.4 Å, and for DEM L243 we found 1.1 Å. As described below, we extracted an additional scanned observation for DEM L243 which excludes the SNR-contaminated region; for this aperture we found an absorption EW of 1.4 Å.

Table 2 lists the reddening-corrected line intensities with respect to Hβ. We estimate that uncertainties in background subtraction, reddening correction, and flux calibration are typically around 5%; the listed errors in Table 2 are obtained from $\sqrt{0.05^2 + (\mathrm{S/N})^{-2}}$, where the S/N is that of the given line. Note that for the individual lines, Hβ is simply used as a scaling factor, therefore the errors do not represent the error in the line ratio with respect to Hβ, but are uncertainties for the individual line intensities only. However, we also list the diagnostic quantities $R23$ (Pagel et al. 1979), $S23$ (Christensen, Petersen, & Gammelgaard 1997), and η' (Vílchez & Pagel 1988) given by equations 3 – 5 in §3.1.2 below; the listed errors for these do represent those of the given line ratio.

We take the intensity of [S III]λ9532 to be 2.5× [S III]λ9069, as set by the relative transition probabilities (Osterbrock 1989). It is important to note that both of these near-IR lines are susceptible to absorption by telluric water vapor. The wavelength and magnitude of this absorption varies depending on the earth's motion relative to the target. Stevenson (1994) emphasizes the insidiousness of the problem, especially because the water vapor lines are usually unresolved by typical instrumental resolution. Therefore extreme care should be exercised in applying correction techniques such as the commonly-used procedure of dividing the target by a reference star. Stevenson also shows that it is unclear that λ9532 should always be expected to be more strongly absorbed than λ9069, as is often assumed. Fortunately, our observations of λ9069 appear to be clear of the telluric absorption, but this issue is worth bearing in mind. As will be apparent below, the diagnostic line ratios involving [S III] do not show any evidence of errors resulting from telluric absorption.

3. SPATIAL COMPARISON TO MODELS

The spatially resolved, stationary slit observations permit a detailed comparison with photoionization models of H II regions. How well do these idealized models reproduce the spectra of real objects, and how accurate is the current generation of stellar atmosphere models for hot stars? We now compare various diagnostic line ratios predicted by the photoionization code MAPPINGS II (Sutherland & Dopita 1993) with the observed line ratios across the nebulae. For the O stars, our default stellar atmosphere models are the "CoStar" models of Schaerer & de Koter (1997). These represent the first models that combine stellar structure and evolution models with atmosphere models. The emergent energy distributions account for non-LTE radiation transfer, line blanketing, and wind blanketing. For the earliest spectral types, the CoStar models are somewhat harder than previous stellar atmosphere models, since all of the effects mentioned tend to obstruct radiative cooling. Schaerer & de Koter (1997) do not provide models at LMC metallicity, but the variation from Galactic to SMC abundances yields variations in the energy distribution of typically less than 0.1 dex, in the sense that the lower metallicity models are slightly hotter. We adopted the models for SMC metallicity, but note that the results are not sensitive to this variation in metallicity.

In Figure 5, we show the CoStar model atmospheres B2, C2, and E2, which correspond roughly to dwarf spectral types O8–O9, O6–O7, and O3–O4; or stellar effective temperature $T_\star$ of 36, 42, and 49 kK, respectively. The correspondence and accuracy of the spectral types and $T_\star$ is subject to uncertainties in the calibration of these parameters. For $T_\star$ the uncertainty is perhaps ±2 kK (e.g., Schaerer & de Koter 1997). DEM L199 is ionized by early Wolf-Rayet (WR) stars, so we also show model WR atmospheres from Schmutz et al. (1992) and Hamann & Koesterke (1998). These will be discussed in detail in § 3.3 below. The vertical, dotted lines indicate the ion-

[2]IRAF is distributed by NOAO, which is operated by AURA, Inc., under cooperative agreement with the National Science Foundation.

ization potentials (IP) required to produce the given ions; these nebular species are thus useful probes of the ionizing spectrum. The ionization edges of H^+ (13.60 eV) and He^{++} (54.42 eV) are clearly apparent.

3.1. *DEM L323: O3–4*

We first examine DEM L323 in detail, which we will take as a reference object on account of its simple morphology and high S/N observations obtained for it. This H II region has the most uniform, Strömgren sphere structure in the sample, and can be seen in Figure 1 to be emerging from a cocoon of presumably neutral material. The ratio of [S II]λ6716/λ6731 suggests electron densities n of a few 10's cm^{-3} in all apertures. The parent OB association is LH 117, whose members have been classified by Massey et al. (1989). We use their identifications for the three stars, #118, #140, and #214, that dominate the nebular ionization. These stars are all of spectral type O3–O4 (Table 1), and their positions are indicated in Figure 1. Two of the dominant stars are close to the center in projection, while star #214 is closer to the edge.

We have two stationary slit positions for DEM L323, both of which bisect the H II region, perpendicular to each other (Figure 1). Figure 6 shows a series of diagnostic line ratios from the apertures in these stationary observations, as a function of position in arcsec, across the nebula. The circular points show the data from position D323.C1, and the crosses are from position D323.C2. The y-axis error bars are the formal errors for the line ratio derived from the uncertainties listed in Table 2. The lighter, x-axis line segments for each point represent the spatial extent of each aperture; note that they do not indicate positional uncertainties. Since both slit positions pass through the center of the object, these plots should be representative cross-sections, projected through the line of sight.

The superimposed lines in Figure 6 show the MAPPINGS model predictions for different stellar atmospheres. The nebular models are divided into five radial zones, as seen in projection by the observer, so we are able to predict the observed cross-section of a spherically symmetric H II region. For most of our models, we take $n = 10\ \mathrm{cm}^{-3}$ as the default electron density, with a filling factor $f = 0.1$. The elemental abundances are weighted averages from the observations, as reported for this object in Paper II, namely, $\log X/\mathrm{H} = (-1.09, -5.15, -3.63, -4.52, -5.34, -5.93)$ for (He, N, O, Ne, S, and Ar). We adopt the values for log C/H and log Si/H of –4.1 and –5.3 from Garnett (1999), that were measured from H II regions in the LMC. For the refractory elements Mg and Fe, we adopted the solar values of Anders & Grevesse (1989), reduced by a factor of –1.6 dex to account for LMC metallicity and grain depletion. This yields log Mg/H and log Fe/H of –6.0 and –5.9, respectively. Since the dominant stars have essentially the same spectral type, we use a single atmosphere model, scaled to the ionizing luminosity $\log L_{\mathrm{Lyc}}/\ \mathrm{erg\ s}^{-1} = 38.7$, implied by the observed Hα luminosity reported by Oey & Kennicutt (1997). In that work, the nebular luminosity was found to be consistent with the expected stellar ionizing fluxes for this object. Figure 6 presents models generated with the CoStar atmospheres shown in Figure 5, and we also show one model with a WR atmosphere, using that of Schmutz et al. (1992). For the observed O3–4 spectral types present, we would therefore predict the model generated with CoStar atmosphere E2 to most closely reproduce the observed ionization structure. The Hα profiles suggest a central cavity of perhaps 40% the Strömgren radius, which we adopt in the models.

It is important to bear in mind that the photoionization models themselves are subject to uncertainty. We have compared the MAPPINGS results to the Lexington benchmarks (Ferland et al. 1995) and single-star photoionization models by Stasińska & Schaerer (1997). For the two blackbody models of the Lexington benchmarks, at solar metallicity ($Z_\odot$), we find excellent agreement. The Stasińska & Schaerer models use the CoStar atmospheres, and we find generally good agreement for both $Z_\odot$ and $0.25Z_\odot$ models, including element ionization fractions, electron temperatures, and line strengths. However, there are slight discrepancies in the sense that the MAPPINGS models produce somewhat lower optical line strengths in, e.g., [O III], [O II], [S III], and [S II]. For atmospheres used in this study, the differences in the models could cause up to ~ 0.2 dex variation in the line ratio predictions.

3.1.1. *U-sensitive diagnostics*

In general, the E2 model (solid line) does a great job of reproducing the observed diagnostics and their spatial dependence on position across the nebula. O and S are the principal elements with strong emission lines of more than one ion that are readily observable in this wavelength range. The ratios of [O III]λ5007/[O II]λ3727 and [S III]λ9532/[S II]λ6724 (Figure 6*a* and *b*) agree well with the E2 model and are within the intrinsic scatter of the different apertures. (The densities of our objects are sufficiently low that λ6717 is largely unaffected by collisional de-excitation; we therefore use the sum of the two red S lines, λ6716 + λ6732, designating this as λ6724, analogous to the unresolved components of λ3727.) These ratios are primarily indicators of the ionization parameter, which can be globally defined for an H II region as,

$$U = Q/(4\pi R_{\mathrm{S}}^2 nc) \propto (nf^2Q)^{1/3} \quad , \tag{2}$$

where Q is the ionizing photon emission rate, and R_{S} is the Strömgren radius. The concept of a local U is commonly described as the relative photon to gas density, but it is helpful to bear in mind that the global U increases with both these quantities, as is apparent from the right side of equation 2. The data show a large range in excitation across the nebula, corresponding to a large range in the local U, which is reproduced well by the models. The models are almost degenerate for the [S III] excitation; this results from the lower ionization potentials of the S ions, which are therefore less sensitive to high $T_\star$. For the hottest model, the WR atmosphere (dot-dashed line), there is actually a decrease in [S III]/[S II] since the ionization balance is redistributed to S^{+4} at IP = 47.30 eV.

We can see a distinct difference in the degree of intrinsic scatter for line ratios that include the lower ionization species, [O II] and [S II] as compared to higher ionization species. As contrasted between Figure 6$a-c,h$ and Figure 6d,i,j, the scatter in line intensities about the mean is about 0.3 dex for [O II] and [S II] and is $\lesssim 0.1$ dex for the higher ionization lines. This difference is apparent in the data for all our objects. The lower ionization species

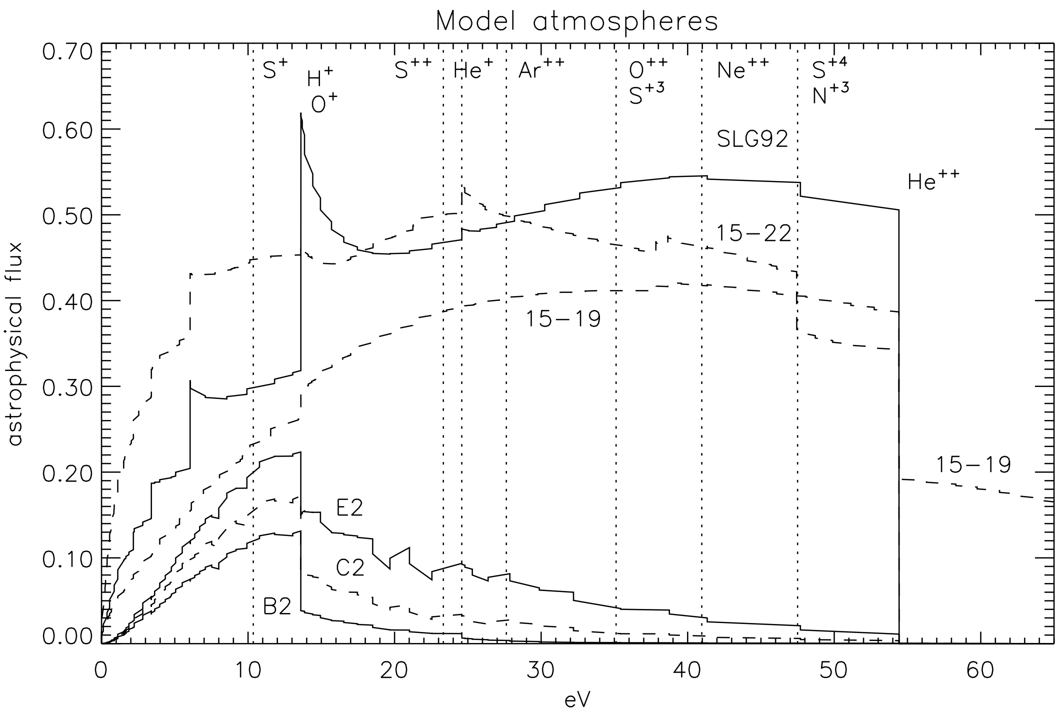

Fig. 5.— Examples of energy distributions from model stellar atmospheres in erg s^{-1} cm^{-2} Hz^{-1} (arbitrary scaling). The bottom three are CoStar models B2, C2, and E2 (Schaerer & de Koter 1997), corresponding to $T_\star \sim 36$, 42, and 49 kK; the top solid line shows a WR model for $\log T_\star/\mathrm{K} = 5.1$ by Schmutz et al. (1992); and the top two dashed lines show WR models for the same $T_\star$ by Hamann & Koesterke (1998), with model #15-19 producing He^{+}-ionizing emission, and #15-22 without. See §3.3.1 for discussion of the WR models. We also indicate the ionization potentials required to produce the named ions.

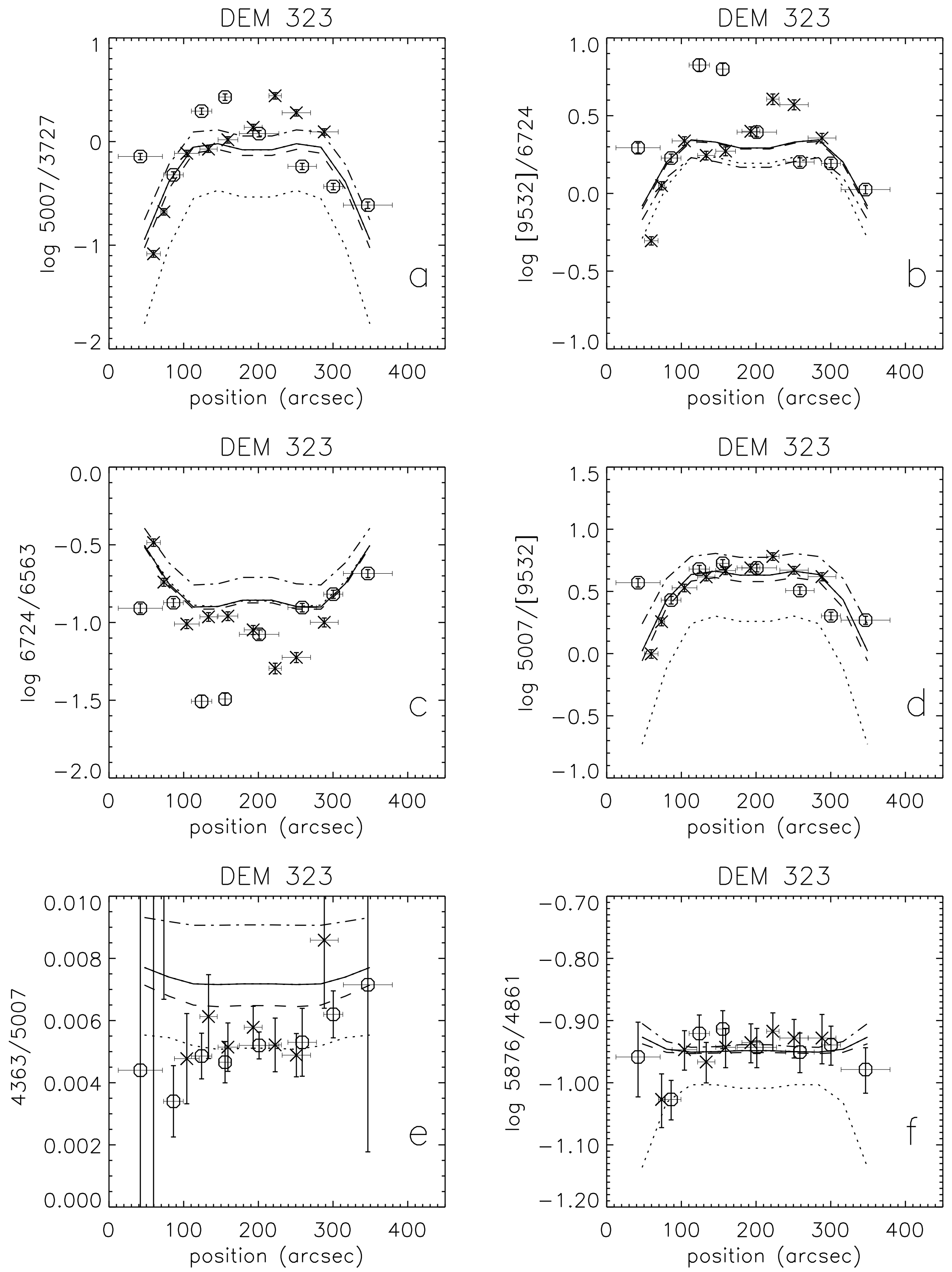

Fig. 6.— Projected spatial variation of diagnostic line ratios across DEM L323. The data points for position D323.C1 (circles) and D323.C2 (crosses) are superimposed, aligned at their intersection (Figure 1). The light, horizontal segments show the spatial extent of the aperture associated with each data point, while the vertical segments are error bars on the data. Dotted, dashed, and solid lines show photoionization models using CoStar atmospheres B2, C2, and E2, respectively; the dot-dashed model uses the WR atmosphere of SLG92. [S III]λ9532 is denoted in brackets to indicate that it is derived from the observed value of λ9069 (see text).

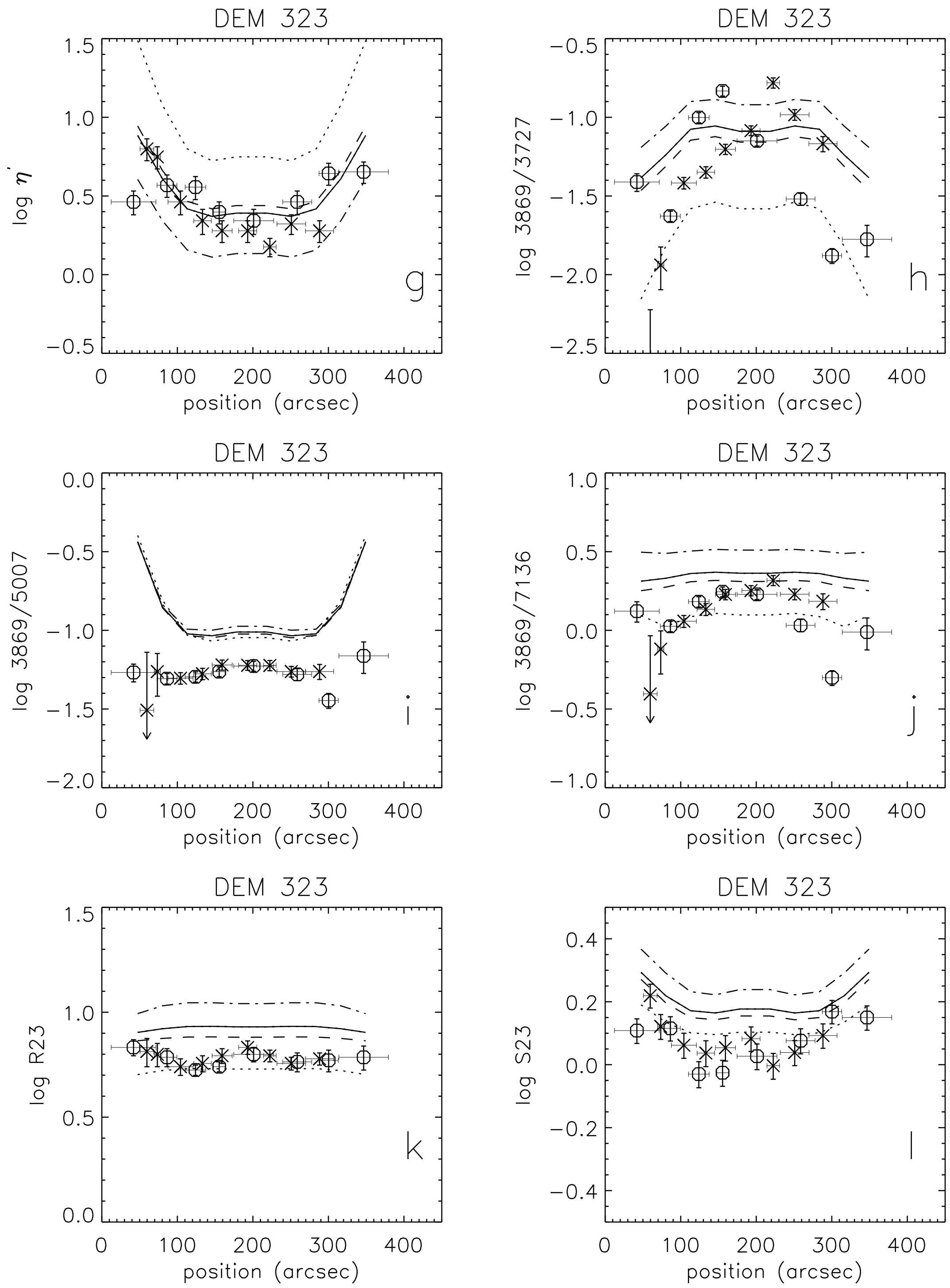

Fig. 6.— *continued*

dominate in the outer regions of the nebulae (e.g., Figure 1*c*), where perhaps there may be more structural and density variations, simply as a matter of greater surface area. The line intensities originating in this zone are sensitive to such variations, especially when compared in a single line of sight to emission from the inner, higher ionization zone. Our data show that individual, spatially resolved line ratios involving lower ionization species should be interpreted with great care, since the large-scale ionization structure has intrinsic order-of-magnitude variation and also a substantial scatter superimposed. This caveat would apply, for example, to the use of [Ne III]/[O II] as an indicator of the He ionization correction factor, as suggested by Ali et al. (1991).

Historically, predictions for the [S III]/[S II] ratio have sometimes been greater than observed values (e.g., Garnett 1989; Dinerstein & Shields 1986). Various causes have been suggested, such as problems with assumed photoionization cross sections and charge exchange reactions. The dielectronic recombination rates could be suspect (Ali et al. 1991). Figure 6*c* and *d* show our data for [S II]λ6724/Hα and [O III]λ5007/[S III]λ9532, which again show good agreement between observations and predictions for model E2. These results are reassuring, and imply that there is in fact no theoretical discrepancy. Furthermore, there is no suggestion of the [S III] intensities being attenuated by telluric absorption.

3.1.2. $T_\star$-*sensitive diagnostics*

We now examine some line ratios that are more sensitive to $T_\star$. The E2 and C2 atmospheres yield almost identical models and resulting diagnostic line ratios, which results from the fact that their energy distributions are quite similar (Figure 5). The implication is that it will be difficult to distinguish spectral types hotter than about 40 kK. One of our objectives is to identify diagnostics that can discern between different stellar temperatures in this regime. Figure 6*f* shows the recombination line ratio He I λ5876/Hβ. The models are degenerate for the hottest atmospheres since the He I Strömgren sphere is fully ionized, but this is not the case for the coolest model, B2. As we shall see below in Figure 12*f*, λ5876/Hβ also decreases when He is ionized to He^{++}.

In Figure 6*e* we show the [O III] ratio λ4363/λ5007, which is the well-known indicator of electron temperature T_e. Atmosphere E2 results in a model that overpredicts this line ratio and produces a model nebula that is about 850 K hotter than indicated by the data. The variation between actual $T_e(\mathrm{O}^{++})$ and T_e([[O III]]) is negligible, $\ll 1\%$. A similar discrepancy in T_e is seen in most of our objects. We confirmed that this result is not peculiar to MAPPINGS by running a similar model using the CLOUDY code (e.g., Ferland et al. 1998), yielding a similarly high T_e. Since the other line intensities and abundances (Paper II) are generally in good agreement with the models, the discrepancy in T_e is puzzling. Restoring the abundances of refractory elements to undepleted values does not resolve the problem. We also note that this discrepancy is in the *opposite* sense of that expected from the well-known effect of spatial temperature fluctuations (Peimbert 1967). In the presence of fluctuations, the characteristic measured T_e should be higher than predictions, since the line emissivity favors the hotter regions. However, in our case the observed T_e is lower than the prediction. We will discuss the nebular temperature structure in more detail in Paper II.

A quantity that is widely used as an observable diagnostic of $T_\star$ is the "radiation softness parameter" (Vílchez & Pagel 1988),

$$\eta' \equiv \frac{[\mathrm{O\,II}]\lambda3727/[\mathrm{O\,III}]\lambda\lambda4959,5007}{[\mathrm{S\,II}]\lambda6724/[\mathrm{S\,III}]\lambda\lambda9069,9532} \quad . \tag{3}$$

Given the excellent agreement between model E2 and the observations in Figure 6$a-d$, it is no surprise that Figure 6*g* also shows a beautiful concurrence. It is disappointing, however, that the models for E2 and C2 are virtually indistinguishable so that η' can no longer discriminate between O7 and O3 stars. As we show below, this was not the case for earlier generations of model atmospheres. Another potential problem with η' is that it is fairly sensitive to U, as is apparent in the variation by about 0.6 dex across the H II region. Thus, extreme care should be used in estimating $T_\star$ from η' for spatially resolved objects.

The line [Ne III]λ3869 is of particular interest because it requires the highest IP (40.96 eV) below that of He II, while producing readily observable optical emission. It is thus an important probe for hot stellar atmospheres. Historically, photoionization models have tended to underpredict [Ne III] emission (e.g., Mathis 1985; Simpson et al. 1986; Garnett et al. 1997), and it was unclear whether this "[Ne III] problem" was caused by shortcomings in the stellar atmosphere models, incorrect Ne abundances resulting from incorrect ionization correction factors, or inaccuracies in the atomic data for Ne. The stellar atmospheres have been considered to be the most likely problem, and Sellmaier et al. (1996) have recently shown convincing evidence that this is the case. Their model atmospheres that include NLTE effects and explicit, comprehensive line-blocking and wind effects produce harder energy distributions that are able to reproduce the observed [Ne III] intensities.

The CoStar models do not include explicit treatment of millions of metal lines, although they do incorporate an approximation to account for line blanketing. Figure 6*h* and *i* show the nebular [Ne III]λ3869/[O II]λ3727 and [Ne III]λ3869/[O III]λ5007. Given the large intrinsic scatter in [Ne III]/[O II], model E2 yields excellent agreement with the observations. However, for [Ne III]/[O III], the models are actually *over*predicting the observations. There is only a short baseline (5.85 eV; Figure 5) in IP for the two ions, so the discrepancy probably corresponds to small-scale features in the stellar energy distribution, or the depth of the Ne^{++} edge. In Figure 6*j* we show [Ne III]λ3869/[Ar III]λ7136, which probes a baseline in the stellar spectrum intermediate to those of the O$^+$ and O^{++} ions. The [Ne III]/[Ar III] ratio also shows a slight overprediction for the E2 atmosphere. To be sure, it is possible to obtain better agreement with the models by adjusting the Ne abundance downward by 0.2 – 0.3 dex. Our adopted value of log Ne/H $= -4.52$ was derived from the standard assumption that Ne^{++}/O^{++} is constant (e.g., Peimbert & Costero 1969; see Paper II), and Simpson et al. (1995) have shown that this assumption appears robust for Galactic objects observed in the mid-IR transitions of Ne$^+$ and Ne^{++}. It would therefore appear that the overestimate of [Ne III] intensities is still most likely caused by the stellar atmosphere models. We also note that reducing the Ne abundance has a negligible effect in resolving the overestimated T_e in the models.

Another widely-used parameter is (Pagel et al. 1979),

$$R23 \equiv \frac{[\mathrm{O\,II}]\lambda3727 + [\mathrm{O\,III}]\lambda\lambda4959,5007}{\mathrm{H}\beta} \quad . \qquad (4)$$

This line ratio is normally used as an indicator of O abundance, but it also varies with $T_\star$. It is therefore important to examine its behavior with $T_\star$ to constrain abundances, and this has been discussed in the literature by many authors (e.g., McGaugh 1991; McCall et al. 1985; Oey & Kennicutt 1993). Figure 6*k* shows $R23$ across the nebula, along with the models for different $T_\star$. We indeed see a strong differentiation between the different atmospheres, and the data are in reasonable agreement with model E2, to within ~ 0.1 dex.

A similar parameter has recently been introduced for S (Christensen et al. 1997; Díaz & Pérez-Montero 1999):

$$S23 \equiv \frac{[\mathrm{S\,II}]\lambda6724 + [\mathrm{S\,III}]\lambda\lambda9069,9532}{\mathrm{H}\beta} \quad . \qquad (5)$$

Figure 6*l* shows the behavior of $S23$ across the nebula. We again see reasonable agreement between the data and model E2, noting that there is spatial variation in this parameter. This is related to a non-negligible ionization fraction of S^{+3}, whereas O^{+3} will not be present in our objects, as evidenced by the lack of He II $\lambda4686$. The models for $S23$ also show a somewhat smaller range of mean values, perhaps ~ 0.15 dex, in contrast to the range in mean $R23$ of ~ 0.4 dex, for the stellar atmospheres used. For high $T_\star$, $S23$ will therefore be less sensitive to the stellar population. A more complete discussion of the abundance applications of these parameters will be given in Paper II.

3.1.3. *Comparison to Hummer & Mihalas atmospheres*

Overall, the diagnostic line ratios presented in Figure 6 show good agreement between the data for DEM L323 and the model predictions for the CoStar atmosphere E2, which corresponds most closely to the observed dominant spectral type O3 – O4. The variation between the observations and predictions is typically $\lesssim 0.1$ dex. Figure 7 demonstrates the degree of improvement shown by the CoStar models over the Hummer & Mihalas (1970; hereafter HM70) LTE atmospheres. The variation between the CoStar and Kurucz (1991) LTE atmospheres is discussed by Stasińska & Schaerer (1997), and should be similar to a comparison with the HM70 atmospheres (Evans 1991). Figure 7 plots some of the same line ratios as before, showing models using CoStar atmospheres E2 and C2 in solid lines, and Hummer & Mihalas atmospheres for 49 kK and 42 kK in dashed lines. The two sets of atmospheres should therefore correspond to the same stellar $T_\star$. The ratios of [Ne III]/[O III] and [Ne III]/[Ar III] (Figure 7*a* and *b*) dramatically demonstrate that the [Ne III] problem was indeed caused by stellar energy distributions that were not hard enough in earlier generation atmospheres. The [Ne III] line ratios for the HM70 atmosphere at 42 kK are reduced by about an order of magnitude in comparison to the CoStar C2 model, because the HM70 energy distribution is not hard enough to produce significant Ne^{++}. The "[Ne III] problem" was identified in the Orion Nebula and regions ionized by $T_\star \lesssim 40$ kK, so the earlier atmospheres at those $T_\star$ would indeed cause that underprediction of [Ne III]. It is also reassuring that the CoStar models compare favorably to the more detailed models of, e.g., Sellmaier et al. (1997) in reproducing the nebular ionization properties, and yield a good approximation to the stellar energy distributions.

Figure 7*c* shows the predictions for the radiation softness parameter η', using the CoStar and HM70 atmospheres. Here we see a strong differentiation between the HM70 42 and 49 kK models, but almost none for the CoStar models. Thus, although previously η' had been predicted to be a good diagnostic of $T_\star$ (e.g., Skillman 1989), unfortunately the new atmospheres now suggest that it cannot effectively discriminate $T_\star$ for stars hotter than about 40 kK. The data are clearly in better agreement with the CoStar models.

We also show in Figure 7*d* the model predictions for the T_e diagnostic, [O III]$\lambda4363/\lambda5007$. The discrepancy with observed temperatures is not resolved by using HM70 atmospheres. We note that Baldwin et al. (1991), in their study of the Orion Nebula, did match 4363/5007, but allowed $T_\star$ to be a free parameter. They arrived at $T_\star = 39.6$ kK for the O6–7 V star θ^1 Ori C, a temperature about 2 kK cooler than the current calibration of that spectral type for the CoStar models. Their work was based on Kurucz (1991) LTE atmospheres, which are also systematically softer than the CoStar atmospheres.

3.2. *DEM L243: O7*

For DEM L243, the dominant ionizing sources are stars #2 and #5 from Oey (1996a), having spectral types O7 V and O7 I, respectively (Table 1). Their positions are identified in Figure 2. The H II region has a fairly uniform morphology with a couple higher density knots (Figure 2*a*). DEM L243 is of special interest because of the prominent SNR on the eastern side; this is almost circular and is outlined in black in Figure 2. We defer a discussion of the SNR to § 3.2.2 below, and first consider only the photoionized region of the nebula.

3.2.1. *Photoionization models*

For our photoionization models, we follow a similar prescription to that for DEM L323. The Hα profile does not show clear evidence of a central cavity, so for DEM L243 we set the inner nebular radius to be 10% of the Strömgren radius. The observed Hα emission (Oey & Kennicutt 1997) implies an ionizing luminosity $\log L_{\rm Lyc}/\,\mathrm{erg\ s^{-1}} = 38.0$, and we scale the input O7 stellar atmosphere accordingly. For DEM L243, we show the effect of varying U, by changing the gas density between $n = 1$ and $100\ \mathrm{cm^{-3}}$ (equation 2). Given the existence of actual fluctuations in gas density and filling factor, local variations in U in this range would be unsurprising. We again adopt abundances that were measured for this object in Paper II, $\log X/\mathrm{H} = (-1.18, -5.18, -3.85, -4.77, -5.51, -6.19)$ for (He, N, O, Ne, S, and Ar), with refractory elements as before. There are three stationary slit positions for DEM L243: one centered on each of the dominant stars, and one passing through the knot associated with the SNR (Figure 2).

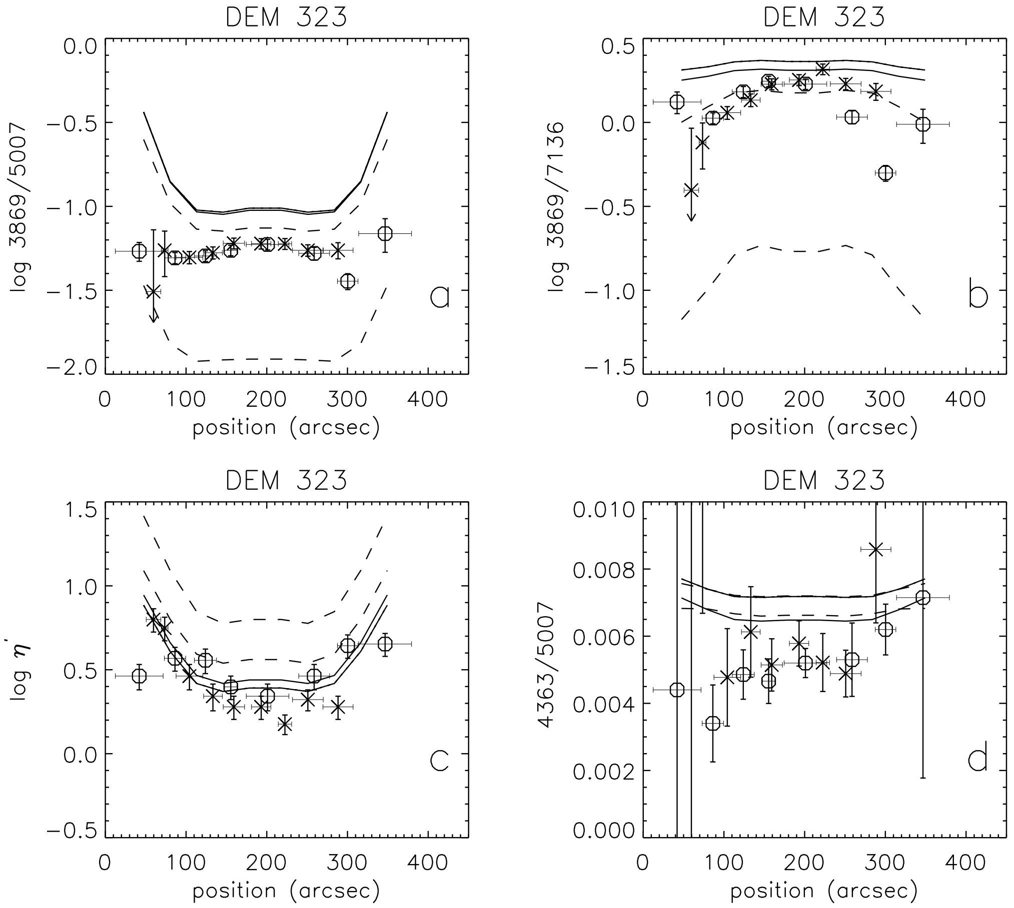

Fig. 7.— Same conventions as Figure 6, but now comparing models using CoStar atmospheres E2 and C2 (solid lines) with those using the corresponding Hummer & Mihalas (1970) atmospheres for 49 and 42 kK (dashed lines).

Since these slit positions do not share a common center, the direct superposition of the data as a function of slit position will not yield a strictly radial cross-section of the nebula, as we had in the case of DEM L323. However, the H II region does not have the simple, spherical morphology of DEM L323, and the two dominant stars are not located close to each other within the nebula. Therefore, we feel that a simple superposition of the slit data still provides an adequate spatial representation of the nebular structure. It is important to bear in mind that the nebular geometry now differs from the spherical symmetry assumed in the models, and spatial discrepancies in Figure 8 should not necessarily be considered significant. As an additional caveat, there is no information on the stellar population north of the prominent dust lane, so it is possible that a star in that northern extension is also an important ionizing source.

Figure 8 presents diagnostic line ratios for DEM L243, using the same conventions as before. The triangles, squares, and crosses show apertures from slit positions D243.2S, D243.5S, and D243.30S, respectively. The solid lines show the MAPPINGS models for CoStar atmosphere E2, at $n = 1$ and 100 cm^{-3}. The dashed and dotted lines show the corresponding models for atmospheres C2 and B2, respectively. For each $T_\star$, the lower-density model corresponds to lower ionization parameter (equation 2), so with the exception of Figure 8*e*, the $n = 1$ models have lower values on the ordinate. For the observed dominant spectral type O7, we now predict atmosphere C2 (dashed line) to most closely reproduce the nebular observations. An overall comparison of the models in Figure 8 with those in Figure 6 for DEM L323 also demonstrates how the range in the given line ratios can change depending on morphology, i.e., size of the central cavity.

Figure 8*a* and *b* show the U diagnostics for DEM L243. We again see the strong degeneracy of the E2 and C2 models, and excellent agreement with the data for [O III]/[O II]. For [S III]/[S II], the models appear to overpredict the data by about 0.2 dex. This appears to result in part from a slight underprediction in [S II]λ6724, as is apparent from Figure 8*c*. The offset between models and data is in the reverse sense from that seen for DEM L323.

The observations of He I/Hβ are interesting (Figure 8*d*). There is a large scatter in comparison to the models, and some values are significantly below the predictions. This scatter is not seen in our other objects (Figures 6*f*, and 12*f*). It would therefore appear that He is not uniformly fully ionized in DEM L243, in contrast to the other objects in this sample. This suggests that the CoStar atmospheres may be slightly too hard around this temperature of $T_\star = 42$ kK. The slight overprediction of S ionization described above is also consistent with an overly hard stellar atmosphere model, although there is some uncertainty in the spectral type $-$ $T_\star$ conversion. It is worth noting that the transition from full to partial He ionization apparently occurs around this O7 spectral type or slightly earlier.

The radiation softness parameter is plotted in Figure 8*e*. Its behavior is similar to that found for DEM L323, and the data are again in good agreement with the model prediction for atmosphere C2. Figure 8*f* and *g* show [Ne III]/[O II] and [Ne III]/[Ar III]. In contrast to DEM L323 (Figure 6*h*), [Ne III]/[O II] is overpredicted in the models by about 0.3 dex. [Ne III]/[Ar III] shows about the same ~ 0.2 dex overprediction for atmosphere C2 as seen for E2 in DEM L323.

The abundance parameter $R23$ is shown in Figure 8*h*. The data are in good agreement with the C2 atmosphere, about 0.1 dex below the prediction.

3.2.2. *The SNR*

The SNR in DEM L243 (N63 A in the Henize 1956 catalog) has been the subject of previous detailed studies (e.g., Shull 1983; Dickel et al. 1993; Levenson et al. 1995). As noted by several authors, the bright optical remnant is offset to the west side of the circular region of X-ray and radio emission, which is delineated by the black circle in Figure 2. Part of the SNR boundary is also visible in the [O III]/Hα ratio map in Figure 2*b*. This shows the area ionized by weak photoionization from the shock precursor. Such precursors are known to generate large [O III]/Hβ ratios (Dopita & Sutherland 1995, 1996), and so this region can be seen in the [O III]/Hα ratio map. The three-lobed structure seen in published images of the optical remnant (e.g., Mathewson et al. 1983; Shull 1983) is barely resolved in our images, and corresponds to the bright knot traversed by slit position D243.30S. Four associated bright knots of shocked gas are clearly apparent in the [S II]/Hα ratio map (Figure 2*c*), and indicate the locus of the blast wave.

In Figure 9, we show some diagnostics for observations affected by the SNR. The diamond corresponds to aperture D243.2S-12, and squares show values for slit position D243.30S. As before, the horizontal lines denote the spatial extent of the aperture, while the error bars are indicated vertically. A photoionization model for CoStar atmosphere C2 with $n = 10$ cm^{-3} is shown with the 'P' symbol. Since these apertures are all localized in one area of the nebula, their relative positions are not significant, so the models are not shown spatially resolved as before. Instead, the vertical dashed line shows the range of values for projected distances up to 0.8 R_{S}, with the 'P' symbol at the locus of the central zone.

We also generated models of plane-parallel shock emission with MAPPINGS v1.1.2, also for $n = 10$ cm^{-3}, and magnetic field strength $B = 10$ μG, thereby corresponding to magnetic parameter $B/n^{0.5} = 3.16\,\mu\mathrm{G\,cm}^{3/2}$, which corresponds to equipartition between the magnetic and gas thermal pressures in the ionized pre-shock plasma. We take an input ionization balance with H 99% ionized, and include contributions to the emission from both shock and precursor. The 'S' track in Figure 9 shows the range of values for shock velocities between 100 and 200 $\mathrm{km\ s}^{-1}$, with the 'S' symbol denoting the locus of the 200 $\mathrm{km\ s}^{-1}$ end. Estimates for the expansion velocity of the optical remnant range from 110 $\mathrm{km\ s}^{-1}$ (Dopita 1979) to 350 $\mathrm{km\ s}^{-1}$ (Shull 1983); additional estimates have been obtained and compiled by Chu & Kennicutt (1988). The presence of at least some radiative shocks with velocities above 200 $\mathrm{km\ s}^{-1}$ is indicated by the presence of the photoionized precursor mentioned above, and seen in Figure 2*b*. Dopita & Sutherland (1995) showed that, for radiative shocks, the velocity of the ionization front produced by the EUV photons from the shock only becomes greater than the shock

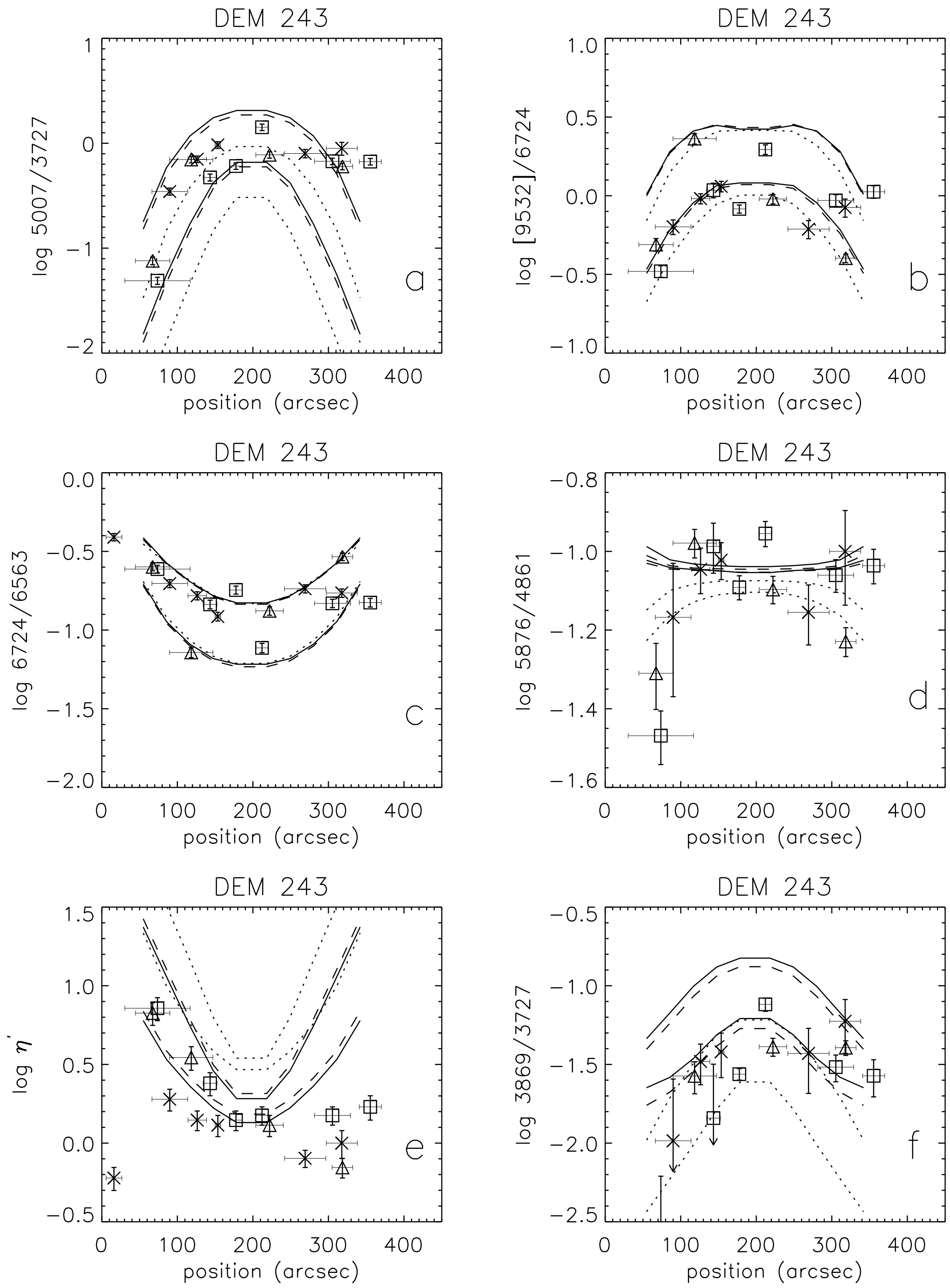

Fig. 8.— Projected spatial variation of diagnostic line ratios across DEM L243. The data points for all slit positions are superimposed. Triangles, squares, and crosses show positions D243.2S, D243.5S, and D243.30S, respectively (Figure 2). Dotted, dashed, and solid lines show photoionization models using CoStar atmospheres B2, C2, and E2, respectively, for densities of $n = 1$ and $n = 100$ cm^{-3} (see text).

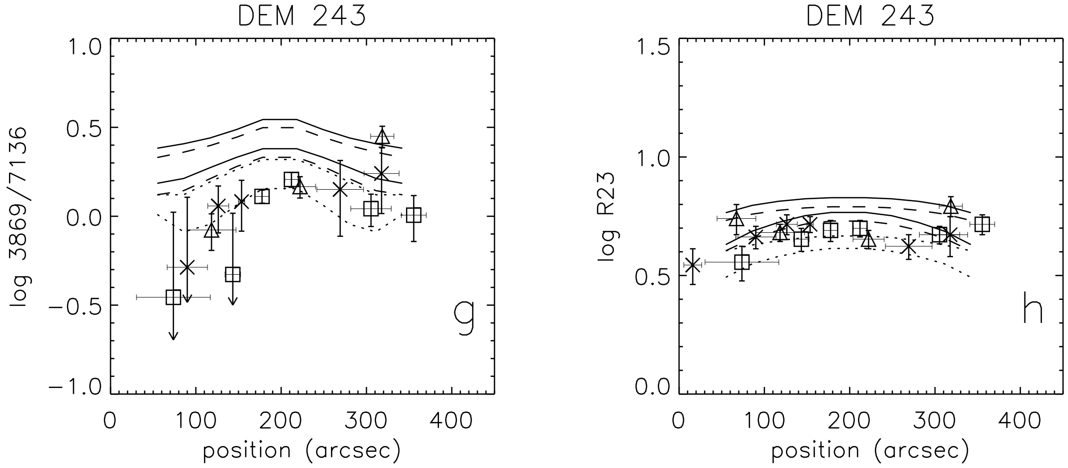

Fig. 8.— *continued*

velocity for velocities $\gtrsim$ 175 km s^{-1}. While we did not detect He II λ4686, Levenson et al. (1995) report two detections of this line, with intensities of 0.044 and 0.024 with respect to Hβ. This is roughly consistent with the prediction of 0.046 for a 200 km s^{-1} shock, undiluted by a stellar photoionized contribution. We combined each of our shock models with the zone of the photoionization model at $0.4 - 0.6\ R_S$. The cross in Figure 9 shows line ratios for the composite with the 200 km s^{-1} model, and the dotted line extends to the sum with the 100 km s^{-1} model.

While the equal weighting, with respect to Hβ emission, in the sum is arbitrary, it is apparent that a composite spectrum is in much better agreement with the observations than either the 'P' or 'S' models alone. Figure 9 also demonstrates that it is the higher velocity shock that more closely resembles many 'P' line ratios, owing to the higher ionization and emission in species like [O III]. However, this enhanced emission does affect both the η' and $R23$ parameters (Figure 9*e* and *f*). Thus, while it may be difficult to diagnose the presence of a 200 km s^{-1} shock, it can cause misleading values in the diagnostic parameters.

This object has historically been identified as an SNR within an H II region, especially since the presence of the OB association LH 83 increases the probability of Type II SN events in the region. However, it might be surprising to find the conventional optical signatures of elevated [S II] and [O I] in an ionized environment where the dominant species of S and O are S^{++} and O^{++}. We suggest that the origin of the blastwave may be located behind the nebula, and is impacting gas behind or near the edge of the H II region. This is also supported by the presence of only blueshifted velocity structure in the optical remnant (Shull 1983). It has been noted by previous authors (e.g., Shull 1983) that the western lobe of the bright optical SNR knot appears to be only photoionized, as opposed to the adjacent lobes, which show the strong shock signatures. This is also consistent with the blastwave impacting the region from behind, or with the SNR being a background object altogether. We note that our superimposed shock photoionized spectra are consistent with the nebular emission, without incorporating combined radiative transfer of these processes. When examining Figure 9, it should be kept in mind that apertures D243.30S-13 and D243.30S-16 cross the photoionized lobe.

3.3. *DEM L199: Early WR*

DEM L199 is a large and luminous nebular complex that poses a greater challenge for the idealized geometry of the photoionization models. As such, it may be more representative of H II regions observed in more distant galaxies. The dominant stars are early-type WR binaries, Br 32, Br 33, and Br 34, having spectral types WC4 + O6 V–III, WN3 + OB, and WN3: + B3 I (see Table 1). The WR atmospheres are much more difficult to model than the main sequence spectral types, and the nebular results are likewise more uncertain. There is also an O3–4 V star present, but it contributes only 10 – 20% of the observed Hα luminosity. In addition, DEM L199 has the most complicated morphology of any object in our sample. The Hα image suggests a range of densities in different regions (Figure 3*a*), although density estimates from the ratio [S II]λ6716/λ6731 are again in the low-density limit, suggesting $n \lesssim$ a few 10's cm^{-3}. There is also a prominent network of shells and filamentary material. The WR stars are located on the interior of the overall shell structure.

3.3.1. *WR model atmospheres*

Comparing the nebular emission-line spectrum with models based on synthetic atmospheres is a particularly important test for WR stars. Crowther (1999) emphasizes the importance of using nebular analyses to test the model atmospheres. The emergent spectra result from complicated radiation transfer in NLTE, supersonic expanding atmospheres having density and opacity stratification and inhomogeneities. A widely-used set of basic models for WR atmospheres is the grid of Schmutz et al. (1992; hereafter SLG92), which consists of pure He atmospheres incorporating NLTE radiation transfer and a power-law wind density law. More recently, Hamann and colleagues have computed new grids that include the principal metals and electron scattering in lines (Hamann & Koesterke 1998; Gräfener et al. 1998). We will exam-

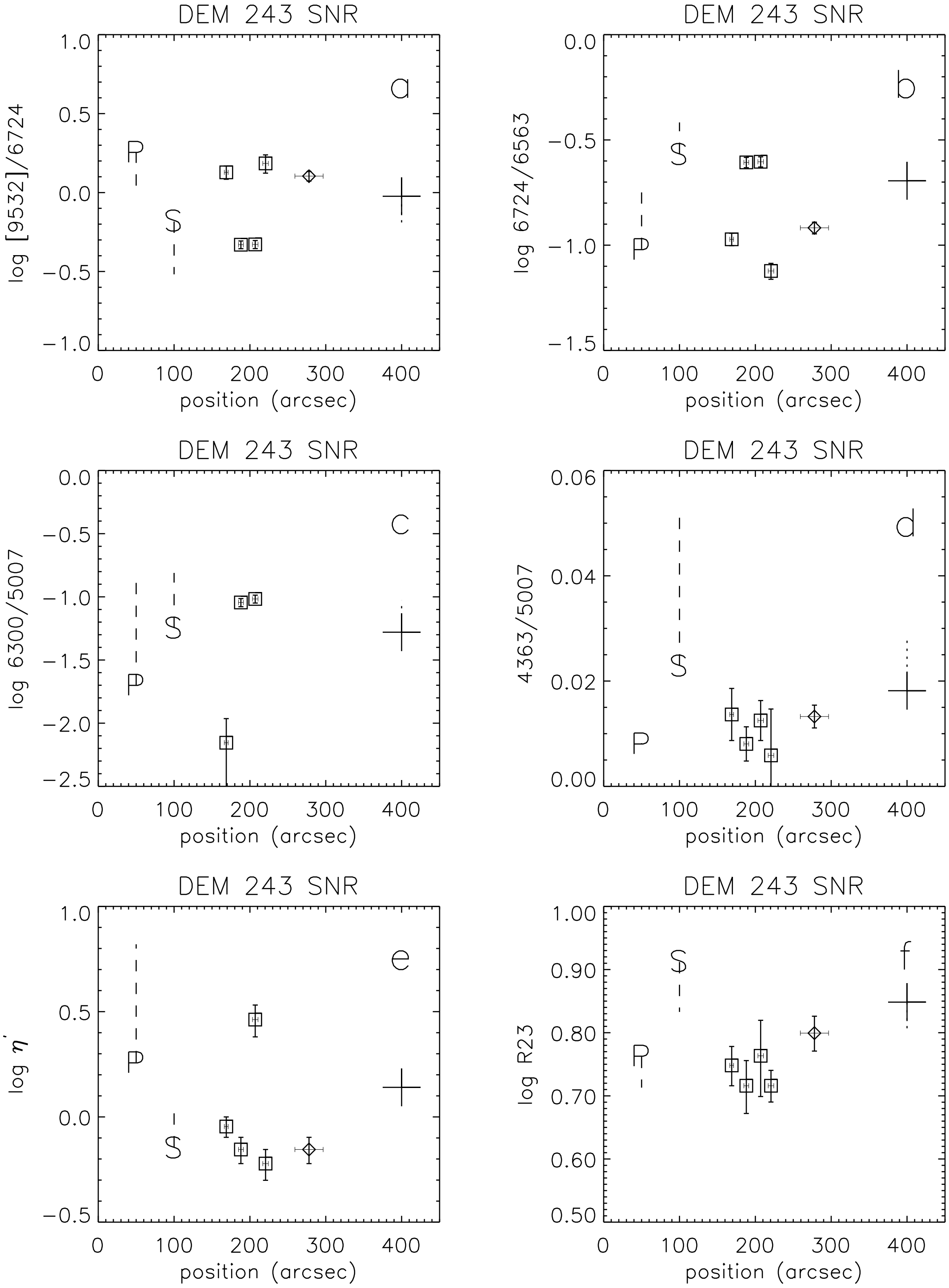

Fig. 9.— Diagnostics for apertures affected by the SNR shock. The diamond and squares correspond to slit positions D243.2S and D243.30S, respectively. The 'P' symbol represents a model photoionized by CoStar atmosphere C2, with the dashed line indicating the range of values for distances up to $0.8R_\mathrm{S}$. The 'S' symbol represents a shock model with $B/n^{0.5} = 3.16\ \mu\mathrm{G\ cm}^{3/2}$ and shock velocity 200 km s^{-1}, with the dashed line extending to a model at 100 km s^{-1}. The cross shows the sum of the photoionized and 200 km s^{-1} shock model, with the dotted line extending to a composite with the 100 km s^{-1} model. The spatial positions for the models are arbitrary.

ine photoionization models using atmospheres from this group, and also SLG92. Crowther (1999) and Schmutz & de Marco (1999) review the various WR models produced by different groups.

Only a few H II regions containing WR stars have been examined in conjunction with the model atmospheres (Crowther et al. 2000; Esteban et al. 1993; Kingburgh & Barlow 1995), and most of these are WR ejecta nebulae. DEM L199 is an interesting case for testing WR atmospheres since it is not an ejecta nebula, but is a large H II region whose principal ionizing sources are WR stars. It should therefore be more analogous, and directly comparable, to classical H II regions than a strongly density-bounded ejecta shell with abundance anomalies.

Slit position D199.205 includes both Br 32 and Br 33, and our scanned position D199.496W87 includes a transient exposure of Br 34 (Figure 3*a*). Our extracted spectra of these stars are shown in Figure 10. The WR models are computed for a grid of R_t and $T_\star$, where R_t is the reference "transformed" stellar radius, and $T_\star$ is now the core effective temperature. We use the spectral diagnostics of Br 33 to estimate its R_t and $T_\star$ from the contours of these parameters on the R_t–$T_\star$ grid of Hamann & Koesterke (1998, their Figures 1 – 3; hereafter HK98) for WN stars. We measure equivalent widths of He II $\lambda5412 \sim 12$ Å, N IV $\lambda4058 \sim 3.5$ Å, and N V $\lambda4933$–$44 \sim 2.7$ Å. There is no detectable He I or N III $\lambda4640$. This is a weak-lined WNE type, according to the the equivalent width of He II $\lambda5412$. The line strengths suggest that the HK98 WN models for $\log R_t/R_\odot = 0.1$ and 0.2, at $\log T_\star/\mathrm{K} = 5.1$ should correspond to the observed WN3-w spectrum. We caution that if the system is indeed a binary as originally suggested by Breysacher (1981), then the equivalent widths may be underestimated; however, we see no evidence of a companion in Figure 10.

There is also a simple and powerful constraint on the atmospheres from the nebular data: we find no detection of nebular He II $\lambda4686$ to $< 1\%$ of the Hβ intensity. Figure 11 shows apertures D199.205-17 and D199.496W87-21 in the vicinity of this line. D199.205-17 is adjacent to Br 33, and D199.496W87-21 scans the region between both of the WN3 stars, Br 33 and Br 34 (Figure 3*a*). This clearly constrains the models to those that produce no He$^+$-ionizing emission. However, it is also interesting that neither Br 33 nor Br 34 show detection of He I $\lambda5876$ (Figure 10*b*). There is a telluric absorption feature close to this position, but it is clear that any emission in He I must be minimal. This lack of stellar He I suggests that the stars are hot enough to fully ionize He^0 to He$^+$. We would therefore expect the production of He$^+$-ionizing photons, yet this is apparently not the case. *Both* of these stars appear to be hot enough to fully ionize He^0 in their atmospheres, yet not hot enough to produce He+-ionizing emission. The applicable stellar model should be one that is essentially on the boundary between these two conditions, and therefore corresponds to a very narrow range of stellar parameters. The boundary contour can be determined on the $R_t - T_\star$ plane, as for example, in Figure 1 of SLG92 and Figure 3 of HK98.

Thus the HK98 models that we selected are adjacent to this boundary, with $T_\star$ determined by the observed stellar N IV, N V, and He II lines. HK98 model #15-22 has $T_\star$ = 125.9 kK and R_t = 0.794 R$_\odot$; model #15-19 has $T_\star$ = 125.9 kK, R_t = 1.58 R$_\odot$. The corresponding model on the SLG92 grid has $T_\star$ = 127.4 kK and R_t = 1.05 R$_\odot$. Note that the atmospheres of the different groups are not strictly analogous since they assume different input physics; the difference in the resulting emergent fluxes is apparent in Figure 5. The SLG92 model has a pure He composition, whereas the HK98 model includes N. More importantly, the SLG92 model assumes a much steeper wind velocity law of $\beta = 2$, where β is the power-law index of the wind velocity gradient. In contrast, the HK98 models assume $\beta = 1$. A hydrodynamically calculated wind velocity law for the WN5 star HD 50896 by Schmutz (1997) suggests that the standard assumption of $\beta = 1$ may be a substantial underestimate in these cases. Also, the HK98 model #15-19 produces He$^+$-ionizing emission, while #15-22 does not.

In comparing with the stellar spectra, model #15-19 predicts no He I $\lambda5876$ in the stellar spectrum, and matches the optical spectrum of Br 33 well (W-R. Hamann, private communication). It is a much better spectral fit than model #15-22, which predicts a $\lambda5876$ equivalent width $\gtrsim 10$ Å, that is not seen in the stellar spectrum (Figure 10*b*). However, #15-19 produces substantial He$^+$-ionizing emission: the nebular models predict He II $\lambda4686$ in the range $0.2 - 0.3$ Hβ, but this is clearly not seen in Figure 11.

Br 34 has a similar spectral type to Br 33 (Table 1), so we presume that it is described by the same model. However, it would be desireable to obtain a better spectrum of Br 34. Br 32 has spectral type WC4, and several stars of this type have been modeled by the same group (Gräfener et al. 1998). Among these models, the WNE atmosphere identified above for Br 33 dominates the emission, so we do not consider the effect of the WC4 star in the energy distribution. Likewise, star #496 (Garmany et al. 1994) is an O3–4 V star, and we noted above that its ionizing luminosity will also be strongly dominated by the WR stars. It is interesting to note that in the [S II]/Hα ratio map of DEM L199, there is a zone of low [S II]/Hα around each of the WR stars (Figure 3*c*). Two apertures, D199.205-14 and D199.205N120-17, that traverse this zone for Br 32 show the highest excitations in the sample for [O III]/Hβ, and among the lowest for [N II]/Hβ and [S II]/Hβ (Table 2). This suggests high ionization states for N and S, perhaps with non-negligible fractions of N^{+3} and S^{+4} in this region, and in fact, the relevant IP's are virtually the same at 47.61 and 47.30, respectively. It may be that the ionization is enhanced by stellar wind shocks, suppressing recombination. The strong [O III]/Hα seen in Figure 3*b* in the zone for Br 34, and measured for the zones around Br 33 and Br 32 are again consistent with these stars being too cool to doubly ionize He.

3.3.2. *Photoionization models*

For the photoionization models, we take $L_{\rm Lyc}/\,\mathrm{erg\ s^{-1}} = 38.9$, obtained as usual from the observed Hα luminosity (Oey & Kennicutt 1997). Based on measurements from Paper II, we adopt abundances: $\log X/\mathrm{H} = (-1.05, -4.1, -4.93, -3.64, -4.40, -6.0, -5.3, -5.30, -5.90, -6.2)$ for (He, C, N, O, Ne, Mg, Si, S, Ar, and Fe). Based on the relative positions of the stars with respect to the gas in this complex, we run MAP-

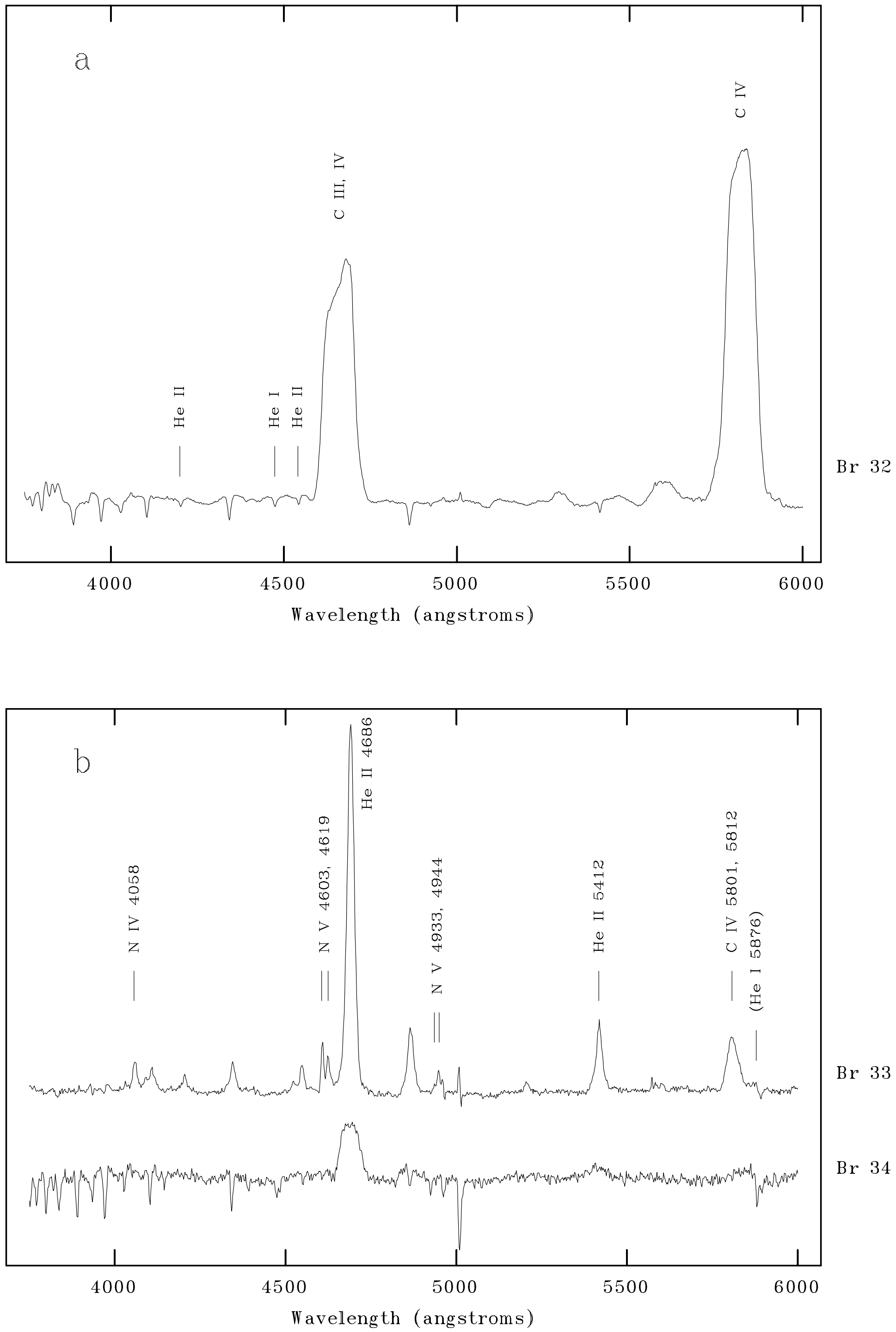

Fig. 10.— Rectified blue spectra of the WR stars in DEM L199. Figure 10*a* shows the WC4 + O6 V-III star, Br 32; Figure 10*b* shows Br 33, a WN3 star with possible OB companion, and Br 34 (WN3: + B3 I). The position of He I λ5876 is indicated; the absorption feature is telluric water vapor. Spectral types are as taken in Table 1.

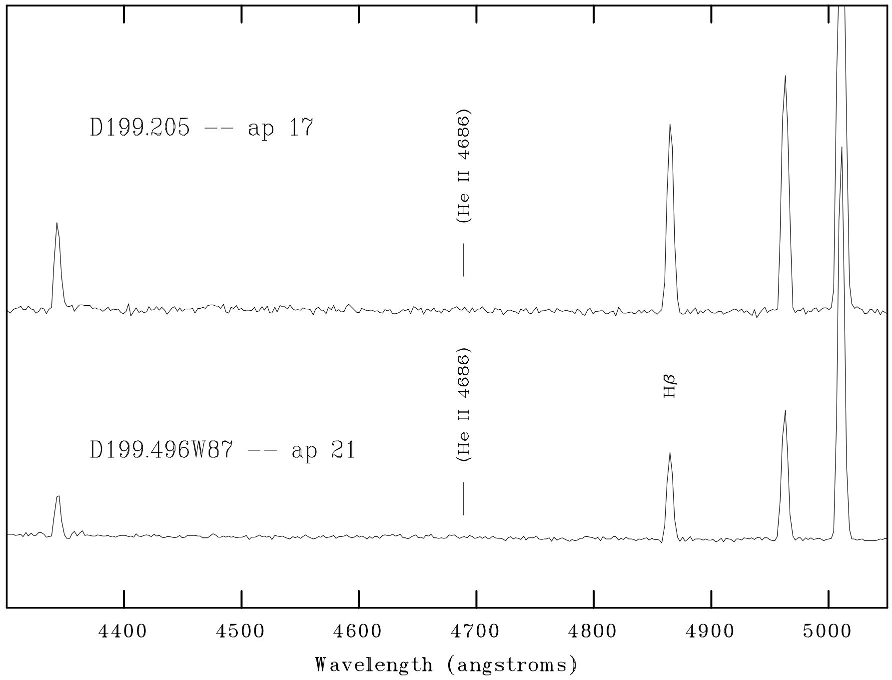

Fig. 11.— Subsections of representative nebular spectra of DEM L199 in two apertures near the WR stars. There is no detection of He II λ4686 to $< 1\%$ of Hβ.

pings with a central cavity of $0.5R_S$. However, clearly the model geometry will be a coarser approximation to reality than for the other objects in the sample. There are two stationary slit observations, and both of these cut across both high and low-density regions, sampling areas both interior and exterior to the shell. We present these data in the same manner as before, by superposing the slit observations; we caution that these will not be expected to closely follow the geometry of the models. Instead, it may be more useful to compare the data with the range in the predicted quantities.

Figure 12 shows the same diagnostic parameters as Figure 6. The squares show data from the stationary position D199.205 and the crosses show D199.205N120 (Figure 3*a*). The solid, dashed, and dotted lines show models for $n = 100$ cm^{-3} using the WR atmospheres of SLG92, HK98 #15-22, and HK98 #15-19. The dot-dashed line shows the results for CoStar model E2 for a hot O star, thus it should not be expected to yield diagnostics consistent with the data. As mentioned above, HK98 #15-19 has the best fit to the stellar spectrum of Br 33, but is predicted to produce nebular He II λ4686. The discrepancy is also apparent in Figure 12*f*, where the population of He^{++} diminishes the intensity of He I λ5876 for the model using atmosphere #15-19. The data are clearly consistent with no He^{++} population.

The atmospheres of SLG92 and HK98 #15-22 (solid and dashed lines) generally show excellent agreement with the data, and produce virtually indistinguishable nebular diagnostics in spite of the noticeable differences in Figure 5. Indeed, these line ratios are extremely robust to the WR atmospheres, except for the distinction between cases that do and do not produce He$^+$-ionizing emission. For example, the HK98 atmosphere for $T_\star = 89.1$ kK, $R_t = 3.98$ R$_\odot$ also produces diagnostics virtually identical to HK98 #15-22.

The U-tracer [O III]/[O II] (Figure 12*a*) shows as good an agreement with the data as was found for the O3-4 stars in DEM L323 and DEM L243 (Figures 6*a* and 8*a*). The data for [S III]/[S II] appear to be about 0.2 dex below the models, however (Figure 12*b*). This may be caused by the fact that the dominant [S II]-emitting zone corresponds to the lower-density, filamentary material on the outer edges of the region. This zone is particularly extensive in this object, and would have a lower U than assumed in these models. As in the previous objects, the predicted [O III] electron temperature for the models is hotter than indicated by the observations (Figure 12*e*), this time by ~ 1500 K.

The η' parameter again matches the WR models beautifully, as found for the O star nebulae. (Figure 12*g*). The other $T_\star$ diagnostics, [Ne III]/[O II], [Ne III]/[O III], [Ne III]/[Ar III], and $R23$ are all still slightly overpredicted as before (Figure $12h - k$). This suggests that the energy distributions of the model WR atmospheres are slightly too hard. [Ne III]/[O III] exhibits the same overprediction problem seen for all the objects. $S23$ is in good agreement (Figure 12*l*), although the two apertures sampling the high-ionization zone around Br 32, mentioned above, show anomalously low values. From the discussion of these apertures above, this demonstrates that $S23$ does not adequately trace all ions of S in high-ionization regions, which are especially relevant to spatially resolved observations or regions dominated by extremely hot stars.

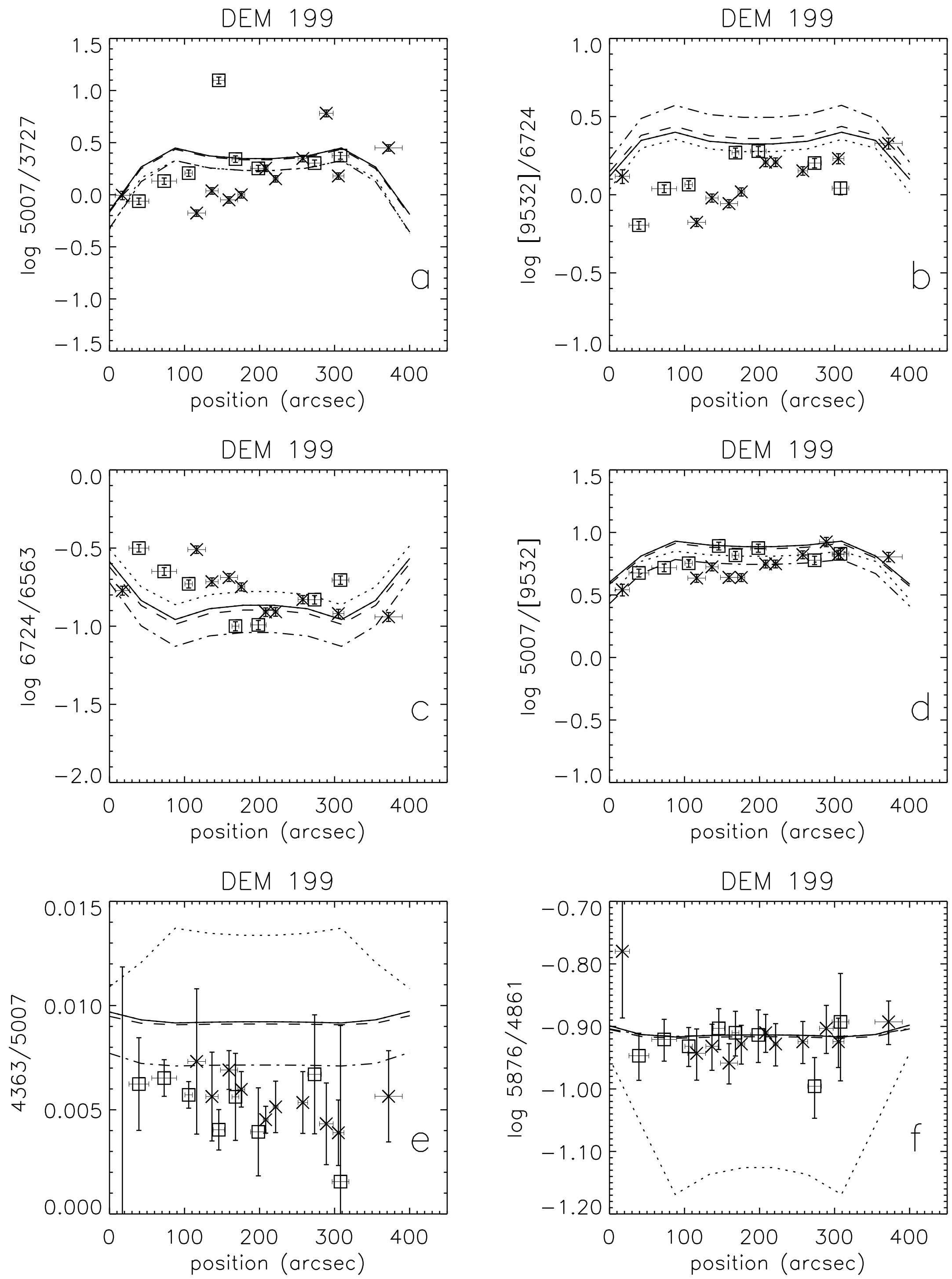

Fig. 12.— Diagnostic parameters as a function of position across the nebula for DEM L199, following the same format as Figure 6. Solid, dashed, and dotted lines indicate results using WR atmospheres from SLG92, HK98 #15-22, and HK98 #15-19, respectively. The dot-dashed line shows results using CoStar atmosphere E2, for an O3 – O4 star.

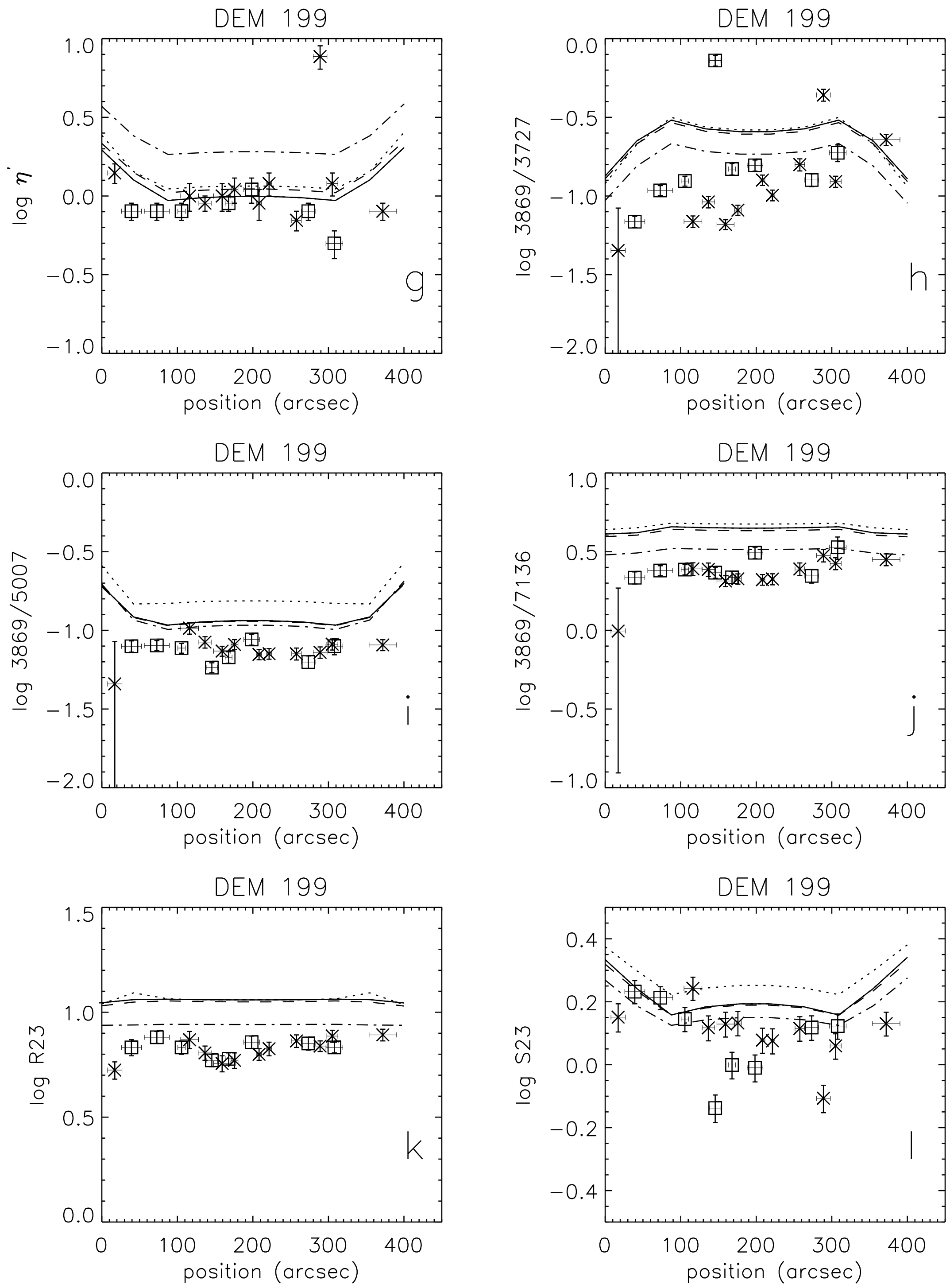

Fig. 12.— *continued*

It would appear to be a strange coincidence that *both* Br 33 and Br 34, and perhaps even Br 32, exhibit the narrow condition of being hot enough to fully ionize He^0, but not hot enough to produce any He^{++}. The He I $\lambda5876$ emission in modeled stellar spectra is sensitive to even small amounts of neutral He in the atmospheres (W-R. Hamann and W. Schmutz, private communications). One possible factor that may alleviate this situation is that all of these stars are binaries. Br 33 was suggested to be a binary by Breysacher (1981), although there is currently no evidence of a companion in Figure 10*b*. Absorption of He I $\lambda5876$ in the companion could mask emission in the WR star, but for Br 33, at least, the effect must be small in view of the lack of any other evidence of a companion. The fact that at least two of the stars in DEM L199 seem to meet this very specific condition hints that we are not seeing the full picture.

3.4. *DEM L301: O3 Shell*

DEM L301 (N70) is a well-known object with a remarkable, filamentary shell structure (Figure 4). The dominant ionizing stars are SW3 and NW4, with spectral types O3 I and O5 III, respectively (Oey 1996a; Table 1). Thus, the nebular emission-line properties might be comparable to DEM L323, except now varying the parameter of morphology. Dopita et al. (1981) found that the nebular emission is largely consistent with photoionization as the dominant excitation mechanism, rather than shocks. However, Lasker (1977) and Skelton et al. (1999) suggest a limited contribution by shock heating to resolve discrepancies that are apparent in the lower-ionization species. This is further supported by the existence of X-ray and kinematic evidence of a recent SNR impact (Chu & Mac Low 1990; Oey 1996b). Thus, the emission properties of this object may be more complex than simple photoionization.

Furthermore, Oey & Kennicutt (1997) and Skelton et al. (1999) found that the observed Hα luminosity of the H II region was much less than expected, based on the stellar census present. We therefore use the stellar parameters instead of the Hα luminosity to constrain the total ionizing flux. From the bolometric magnitudes reported by Oey (1996a), we obtain bolometric luminosities for SW3 and NW4 of $\log L_\star/\,\mathrm{erg\ s^{-1}} = 39.07$ and 39.15, respectively. Our photoionization models therefore assume a total stellar bolometric luminosity of $\log L_\star/\,\mathrm{erg\ s^{-1}} = 39.4$. We also compute shock models for this object, again including contributions to the emission from both shock and precursor. For DEM L301, we take an initial ionization balance with H 20% neutral, since this object has a low ionization parameter. The results are insensitive to details of the initial ionization balance, however. Based on results in Paper II, the adopted abundances are: $\log X/\mathrm{H} = (-1.05, -4.1, -5.14, -3.90, -4.64, -6.0, -5.3, -5.45, -6.23, -6.2)$ for (He, C, N, O, Ne, Mg, Si, S, Ar, and Fe).

We have only stationary slit observations for this H II region: one position along the west edge, and one across a central region (Figure 4*a*). As is apparent in Figure 13, the apertures for both slit positions yield similar spectra, suggesting that the central position, D301.SW1 (triangles), is sampling emission from essentially the same radial zone as the edge position, D301.SW6 (diamonds). This suggests that the shell is indeed hollow and has very little emitting gas in interior regions. Figure 13 also shows the diagnostic ratios predicted from four models. The 'P' symbol shows predictions for a photoionized, radiation-bounded model with inner and outer radii of 50 and 53 pc; these geometric boundaries require a density $n = 35\ \mathrm{cm^{-3}}$. The 'D' symbol shows a density-bounded model with the same inner radius of 50 pc, but density $n = 10\ \mathrm{cm^{-3}}$, and an outer radius truncating the nebula at a radius of 53 pc. This model includes roughly some 60% of the total volume of a radiation-bounded nebula at this gas density. For the 'P' and 'D' models, the diagnostic ratios show little variation between central and edge lines of sight. We also computed shock models for $n = 10\ \mathrm{cm^{-3}}$ and magnetic parameter $B/n^{0.5} = 3.16\ \mu\mathrm{G\ cm^{3/2}}$. These models are shown with the dashed line, with the letter 'S' indicating the locus of a $70\ \mathrm{km\ s^{-1}}$ shock, and the opposite end of the line corresponding to a $100\ \mathrm{km\ s^{-1}}$ shock. The choice of these velocities is motivated by Fabry-Perot observations of Rosado et al. (1981), whose data for over 1000 positions across the nebula were most consistent with an expansion velocity of $70\ \mathrm{km\ s^{-1}}$. Finally, the cross symbol shows a model that combines the density-bounded model and the $70\ \mathrm{km\ s^{-1}}$ shock model.

The diagnostics presented in Figure 13 permit a detailed evaluation of the candidate excitation processes. Examination of the ratios [S III]$\lambda9532$/[S II]$\lambda6724$ (Figure 13*b*) and [O III]$\lambda4363/\lambda5007$ (Figure 13*f*) indeed shows the photoionization models in much better agreement with the observations than the shock models. The predicted stellar ionizing luminosity is a factor of ~ 5 greater than implied by the observed Hα luminosity (Oey & Kennicutt 1997), suggesting that a photoionized model of the nebula should be density-bounded. However, where the radiation-bounded ('P') and density-bounded ('D') models differ, we see that neither can satisfactorily account for all the diagnostics shown. While the 'P' model is consistent with [S II]$\lambda6724$/Hα (Figure 13*c*), line ratios such as [O I]$\lambda6300$/[O III]$\lambda5007$ and [O III]$\lambda5007$/[S III]$\lambda9532$ (panels *d* and *e*) are in better agreement with the 'D' model.

We do find a satisfactory resolution to the puzzle by adding the density-bounded, photoionized model with the shock model. By simply summing the 'D' model with the $70\ \mathrm{km\ s^{-1}}$ 'S' model, using equal weighting in Hβ line flux, we find remarkable agreement in all the diagnostics shown in Figure 13 (crosses). As in the case for DEM L243, the composite model implies distinct, shock-dominated and photoionized components superposed. Hβ flux for the 70 $\mathrm{km\ s^{-1}}$ shock model is $5 \times 10^{-5}\ \mathrm{erg\ s^{-1}\ cm^{-2}}$. For the observed shell radius of 53 pc, this would yield a total Hβ emission of $1.7 \times 10^{37}\ \mathrm{erg\ s^{-1}}$ if the entire nebula were shock-excited. This is exactly the same as the observed value (Oey & Kennicutt 1997), thereby demonstrating that the shock model is easily capable of significantly contributing to the emission as suggested by the composite model. Our preferred model for DEM L301 is a composite structure in which radiative shocks are propagating outward, forming a system of dense filaments, while the cool, post-shock gas in these filaments is photoionized on the inner surface by radiation from the central stars.

The ambiguity of this emission-line spectrum emphasizes the necessity of a careful analysis in determining the

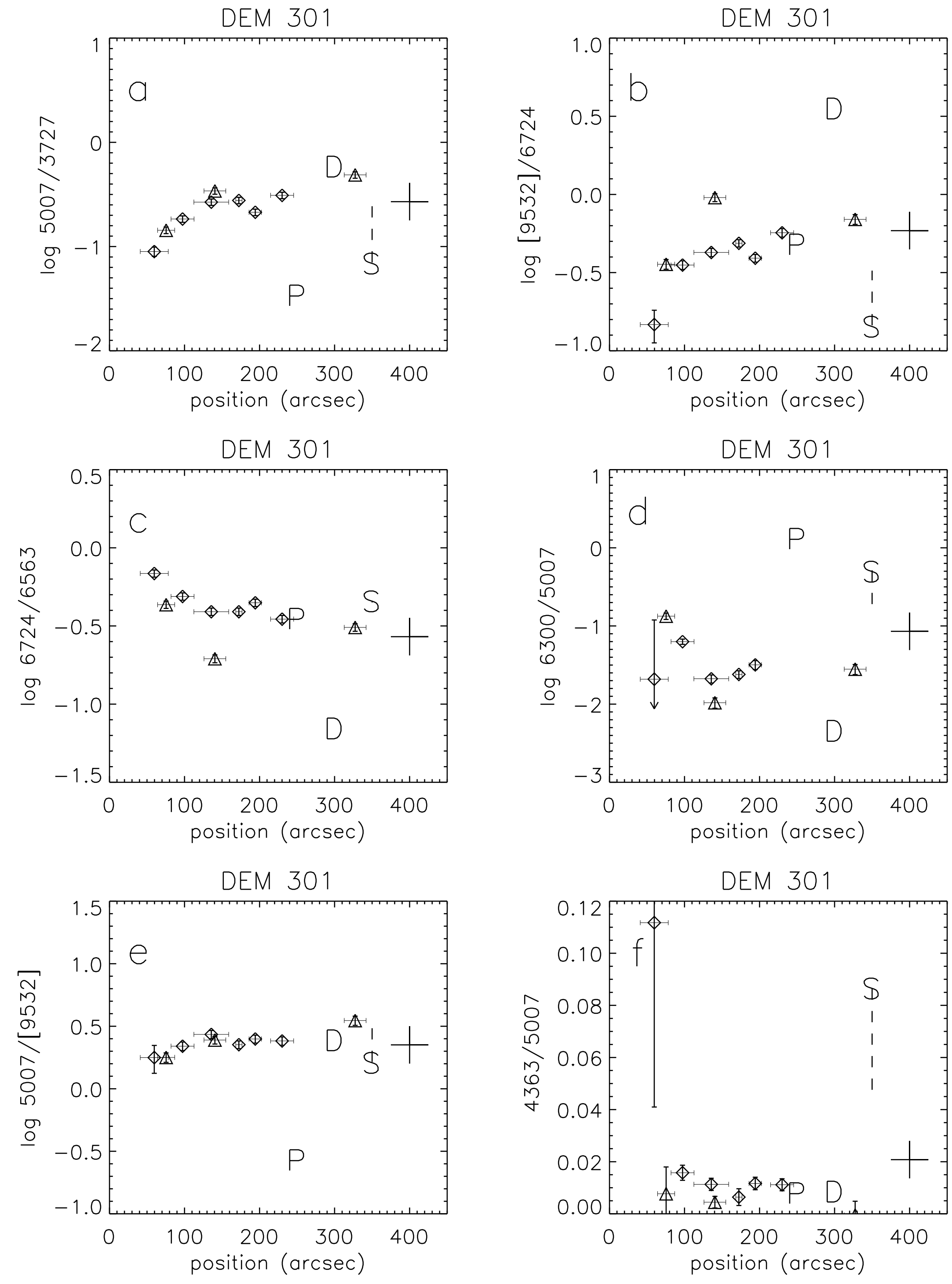

Fig. 13.— Diagnostics for DEM L301, with triangles from slit position D301.SW1 and diamonds from D301.SW6. The 'P' and 'D' symbols show the loci of the radiation- and density-bounded photoionized shell models; the 'S' symbol represents a 70 km s^{-1} shock model, with the dashed line extending to a 100 km s^{-1} model. The cross shows a composite of the 'D' and 'S' models (see text for details on all the models). The spatial positions of the models are arbitrary.

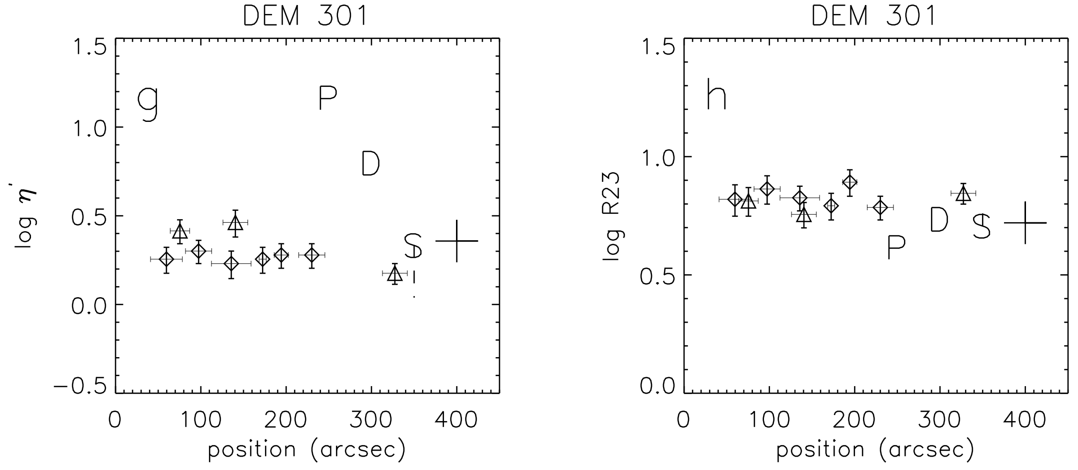

Fig. 13.— *continued*

excitation mechanisms. It is apparent that the H II region is not strongly density-bounded, as evidenced by the ratios of [O III]/[O II] and [S III]/[S II] (Figure 13*a* and *b*), and by the [S II]/Hα ratio map (Figure 4*c*). The contribution of shock heating to the lower-ionization species also partly counteracts the loss of low-ionization emission in a photoionized, density-bounded nebula, for example, in the ratios [S II]/Hα and [O I]/[O III] (Figure 13*c* and *d*). These characteristics may lead to an initial diagnosis suggesting predominantly radiation-bounded photoionization. Furthermore, it is apparent that conventional shock indicators such as [O I]/[O III] and $\lambda\lambda$4363/5007 (panels *d* and *f*), for low-velocity shocks, are easily diluted in the presence of photoionized gas, owing to low shock excitation in higher-ionization species like [O III].

It is apparent that the ambiguous line ratios do not clearly delineate DEM L301 as a density-bounded object. As just described, the H II region is not strongly density-bounded, despite the fact that only about 20% of the emitted stellar ionizing radiation is absorbed by the nebula (Oey & Kennicutt 1997). However, the highly filamentary morphology apparent in Figure 4 suggests that the majority of this ionizing radiation is escaping through "windows" between the filaments. Thus apparently, where absorbing material exists, it is thick enough to present some diagnostics resembling radiation bounding, whereas most of the ionizing photons are in fact easily escaping. This object therefore demonstrates that strong spectral signatures of density bounding are not required evidence for enormous photon leakage from H II regions.

It is also worth noting the behavior of the parameters η' and $R23$ (Figure 13$g - h$). If the composite model is correct, adding the density-bounded photoionization and shocks, we see that η' is significantly underestimated, compared to a standard, radiation-bounded situation. A contribution by shocks will therefore lead to an overestimate in the inferred stellar $T_\star$. On the other hand, $R23$ is largely insensitive to *any* of the modeled conditions, and is a robust diagnostic in the presence of shocks with velocities $\lesssim 100$ km s^{-1}. $R23$ does become sensitive to higher shock velocities, however, as seen in Figure 9f.

4. SPATIALLY INTEGRATED SPECTRA: $T_\star$ SEQUENCE

Spectrophotometric observations of H II region complexes in distant galaxies inevitably result in the averaging of line ratios across an appreciable fraction, or entirety, of an object. Our spatially integrated observations that were obtained by scanning the slit across the H II regions (Table 3) should approximate those obtained by conventional $1 - 1.5''$ slit observations if the LMC were at a distance of roughly 15 Mpc. In Figures 1a – 3a, the two end positions of the scanned observations are shown in black. (As indicated in these figures, we also extracted smaller apertures from the scanned positions, but will not discuss these here.)

How well can we determine $T_\star$ from the diagnostic line ratios of the integrated spectra? Figure 14 shows η' and [Ne III]/Hβ from the integrated spectra for our objects. For DEM L243, we show values derived from the spectrum with the SNR-contaminated region subtracted (solid diamond); and we also show the total integrated region, including the SNR (open diamond). DEM L323 has three scanned observations (triangles): one across the northern half of the object, one across the southern half, and one across the entire nebula (see Figure 1a). Diagnostics from the total integrated spectrum across the entire nebula are indicated with the solid triangle. For spherical symmetry, these should all produce similar results, so the variation between these gives an indication of the how well subsampling is representative of the total spectrum. The square and cross show DEM L199 and DEM L301, respectively. DEM L199 has a larger angular size, and our scanned position did not traverse the entire nebula (Figure 3a). However, we included both low and high-surface brightness regions in proportions that we hope are representative of the entire nebula. Likewise, the scanned region includes areas both near and far from the ionizing stars. Again, the variation in the three observations of DEM L323 suggests the degree to which the single scan of DEM L199 might be representative. In lieu of a scanned observation of DEM L301, we use the spatially integrated data from aperture D301.SW6. Since the shell morphology of this H II region is so thin, the stationary observations are reasonably representative of the integrated spectra, as indicated by the smaller range in values for the diagnostic parameters (Figure 13).

Each line in Figure 14 represents a track of photoionization models that varies $T_\star$, using the same stellar atmosphere models as before: O8–9 (B2), O6–O7 (C2), and O3–O4 (E2) CoStar models, and the WR atmosphere of SLG92, with $T_\star = 127.4$ kK and $R_t = 1.05$ $R_\odot$. We take $\log L_{\rm LyC}/\,{\rm erg\ s^{-1}} = 38.7$, which is the value for DEM L323, and a default central cavity of $0.1R_{\rm S}$. As before, the filling factor is 0.1, and the default LMC metallicity is that for DEM L323 (§3.1). Tracks with the same line type vary U by changing the density over $n = 1, 10$, and 100 cm^{-3}. The dotted lines show shell models with a central cavity of $0.9R_{\rm S}$; and the dashed lines show models with the default inner radius, at SMC metallicity. For the SMC abundances, we take He from Russell & Dopita (1992), Mg and Fe depleted by −2.0 dex from the solar values of Anders & Grevesse (1989), and the remaining elements as reported by Garnett (1999) from H II region measurements, hence: $\log X/{\rm H} = (-1.09, -4.6, -5.5, -4.0, -4.8, -6.4, -5.7, -5.7, -6.1$, and $-6.3)$ for (He, C, N, O, Ne, Mg, Si, S, Ar, and Fe).

At the time of this writing, Kennicutt et al. (ApJ, in preparation; hereafter KBFM) are also completing a study that investigates the behavior of $T_\star$ with nebular diagnostics. They have kindly made available their data to us, and we overplot a subset of their nebular line ratios in Figure 14 with numerical symbols. Their data represent stationary slit positions on Galactic (small symbols) and LMC (large symbols) H II regions. For their LMC observations, measurements for λ5007 and blueward were obtained with the CTIO 2D-Frutti image tube, and the rest of their data were obtained with CCD detectors. Their line ratios appear to show an offset from ours in Figure 14, and this is probably caused primarily by their selection of the brighter, central areas of the H II regions, which have higher local ionization parameters, as shown in their work and §3 above. Most of the well-known Galactic H II regions subtend many 10's of arcminutes or even degrees, and it is therefore more difficult for a single slit position to characterize the emission-line properties. These objects also present a greater challenge in cleanly identifying the ionizing stellar population, owing to patchy extinction and distance uncertainties. To make the best comparison to our data, we therefore take from their Galactic sample only those objects studied by Hunter & Massey (1990) and Esteban et al. (1993), plus the Orion nebula (M42). Hunter & Massey (1990) specifically examined a sample of small Galactic H II regions with the goal of spectroscopically classifying the ionizing stars. Any objects in the Hunter & Massey sample for which the dominant star was not spectroscopically identified was also omitted. The work by Esteban et al. (1993) was a similar study, for WR nebulae. We do include all of the KBFM LMC objects that were not part of our study. Table 4 lists the objects we include from their sample, along with the spectral types of the ionizing stars and references. In Figure 14, we show their objects ionized by (WR, O3–O4, O5–O8, and O9 – B0) with the symbols (1, 2, 3, and 4), respectively. The 30 Dor giant H II region is indicated with a tick mark.

Figure 14*a* shows the conventional measures of the radiation softness parameter η vs. the ionization parameter U, displaying the observables η' vs. [O III]/[O II]. We can see from the models that η' is insensitive to metallicity, since the numerator and denominator of equation 3 correspond to the ionization of single elements. However, it is apparent that η' is signficantly affected by nebular morphology. Stasińska (1999) and Garnett & Kennicutt (1994) demonstrated that changing the geometry between a filled and hollow sphere produces different ionization properties than merely changing the mean ionization parameter, although the local change in U is the dominant effect. The variation in η' over the parameter space for our models shows offsets by 0.3 − 0.5 dex, which is the same range in η' displayed by the data itself.

Empirically, however, Figure 14*a* shows that the data for DEM L323 and DEM L301 do *not* exhibit the offset predicted in the models. These are the objects with similar O3 − O4 ionizing stars, but with Strömgren sphere vs. shell morphology. DEM L323 (triangles) shows values of η' in the predicted range, and DEM L301 (cross) shows a similar value, rather than a higher one, as predicted for its shell morphology. As seen in Figure 13*g*, density-bounding and shock excitation can explain this behavior. On the other hand, DEM L301 does exhibit the predicted strong decrease in [O III]/[O II].

As found in §3 from the spatially resolved analysis, η' is not predicted to be sensitive to $T_\star \gtrsim 40$ kK for H-burning stars, using the CoStar atmospheres. Our spatially integrated data also support this, since it is apparent that the data for DEM L323 (triangles) and DEM L243 (solid diamond) show values that are difficult to distinguish. Combined with the KBFM data (2's and 3's), we do see a tendency for the later types to fall to higher η', but it is impossible to empirically differentiate the early and late types around $\eta' \sim 0.5$. The WR objects, however, do show significant differentiation from the others. DEM L199 shows a typical observed value of $\log\eta' = -0.15$. Although this H II region includes substantial shell structure (Figure 3), the integrated ionization parameter as indicated by [O III]/[O II] is still the highest of any of our objects. This is also true in spite of the fact that the WR stars are located at some distance from the high-surface brightness areas. The KBFM data for 30 Dor do show a value closer to those of early O star nebulae. Massey & Hunter (1998) suggest that most of the WN stars in this object are actually core H-burning stars that are so hot that they exhibit WR features. The locus of the KBFM nebular observations of 30 Dor are consistent with this interpretation, although we again caution that they are taken from a single slit position. Turning to the KBFM objects dominated by O9 − B0 stars (4's in Figure 14*a*), we see that η' indeed recovers its sensitivity, and can reliably identify this stellar population for $\eta' \gtrsim 1$.

As expected, the integrated spectrum for DEM L243 including the SNR shows a hotter value of η' than implied by the photoionized region only. The same appears to be be true for DEM L301. It is therefore important to test for the presence of superimposed SNRs or shocks by some independent measure, such as the [O I] line strengths. Another strong discriminant would be the presence of [Fe II] and Ca II lines in the visible or near IR. However, as we saw in the case of DEM L301, the presence of shocks may

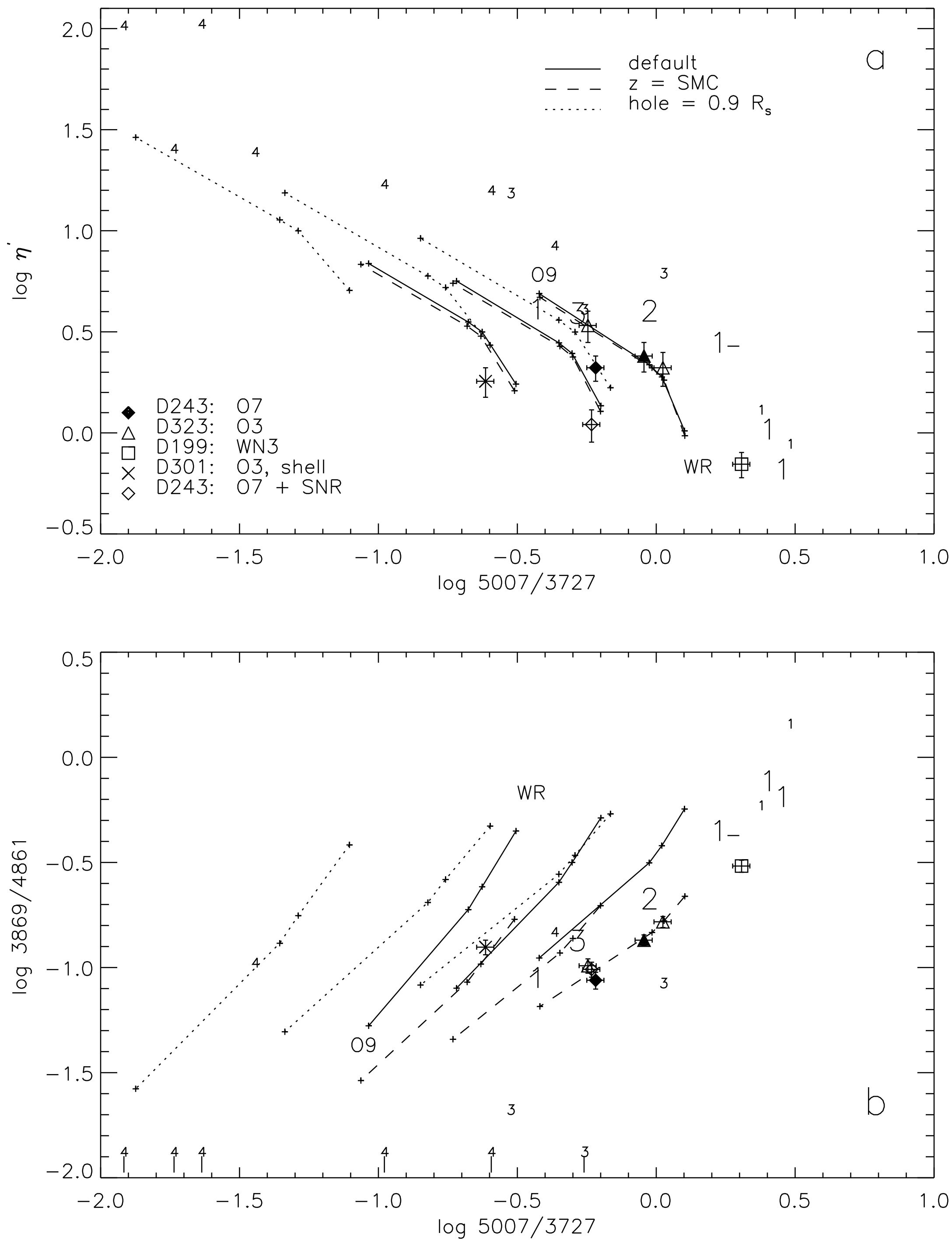

Fig. 14.— Diagnostic parameters η' and [Ne III]λ3869/Hβ vs. [O III]λ5007/[O II]λ3727. Each track of spatially integrated models shows a range of $T_\star$, with the high and low extremes indicated. Default model parameters are LMC metallicity measured from DEM L323 and central hole size of 0.1 R_S. Different line types indicate variations from default, as given by the key in Figure 14*a*. The three tracks for each line type correspond to $n = 1,\ 10$, and 100 cm^{-3}, with the the last having the highest values in [O III]/[O II]. Spatially integrated spectra for our objects are shown with the symbols indicated by the key in Figure 14*a*. The solid triangle corresponds to the scan over the entire object for DEM L323. Numerical symbols show data from BK that are *not* spatially integrated, with LMC and Galactic objects shown with large and small font, respectively. The numbers (1, 2, 3, 4) correspond to types (WR, O3–O4, O5–O8, O9 –B0), respectively.

be difficult to ascertain. We also note that our nebular spectra presented here do not resolve any velocity structure revealing the shocks.

In Figure 14*b* we show a similar diagram, now examining whether [Ne III]/Hβ might be a useful indicator of $T_\star$. This diagnostic shows a larger range of values in differentiating $T_\star$. We initially investigated [Ne III]/[O III] and [Ne III]/[Ar III], but these line ratios did not improve the range of sensitivity as much as simply using [Ne III]/Hβ. In contrast to η', [Ne III]/Hβ is fairly insensitive to the nebular morphology; the variation with morphology follows the same track as that for ionization parameter. However, [Ne III]/Hβ should of course be completely sensitive to the metallicity, as can be seen from the effect of the 0.28 dex variation in Ne abundance between the adopted LMC and SMC metallicity in these models. It is also apparent that the data are not falling on the predicted locus of the models. This is unsurprising, since the [Ne III] intensity appears to be systematically somewhat overpredicted in the models shown in §3. Likewise, [O III]/[O II] is often slightly underpredicted by the models, resulting in the offset between the data and predictions in Figure 14*b*. We therefore recommend using an empirical calibration if these diagnostics are used to infer $T_\star$.

Nevertheless, the data form a fairly clean sequence in Figure 14*b*. KBFM measurements with no [Ne III] detection are shown along the bottom, at their measured [O III]/[O II] values. Surprisingly, the Galactic and LMC objects do not show the predicted dependence on abundance; additional data are necessary to understand the metallicity dependence. The scatter in the points for DEM L323 (triangles) and DEM L243 (diamonds) shows that it is still difficult to reliably distinguish the O7 and O3 stellar temperatures, although the degeneracy is less than for η'. Furthermore, it appears that this diagnostic is less sensitive to the presence of shock excitation, since the loci for DEM L243 with shock and DEM L301 do not show obviously anomalous positions. Presumably only faster shocks would be able to produce enough Ne^{++} to significantly affect the [Ne III]/Hβ ratio. We do see an anomalous locus for one WR object in the KBFM LMC sample, which corresponds to N51 D, a superbubble H II region. This object does not follow the predicted track for shell objects, nor that for WR-dominated objects. The discrepancy may again be related to the localized sampling of nebular conditions. There are also a couple of O9 – B0 objects showing apparently significant [Ne III]/Hβ fluxes; the one with higher [O III]/[O II] is S288, whose spectral type is not as well-determined (Table 4).

Based on Figure 14*b*, we tentatively suggest an empirical calibration for [Ne III]/Hβ and η', for LMC metallicity, given in Table 5. We do not assign $T_\star$ in Table 5, since the evidence discussed above suggests that the spectral type – $T_\star$ conversion used with the CoStar models gives $T_\star$ that are somewhat too hot.

We defer a full discussion of the abundance parameters, $R23$ and $S23$ to Paper II. However, it is worth emphasizing their $T_\star$-dependence here. As can be seen in Table 3, the observed values of $R23$ and $S23$ for the integrated spectra do follow a sequence such that lower values correspond to cooler $T_\star$. As seen in the spatially-resolved models of §3, the predicted values are in good agreement with the data, although tending to be slight overestimates.

5. CONCLUSION

We have obtained both spatially resolved and integrated observations of four H II regions, with ionizing stellar spectral types of O7, O3–4, and WN3, and morphologies ranging from Strömgren sphere to extreme shell. Two of the objects show evidence of shock excitation in addition to the dominant photoionization. Empirically, we find that lower-ionization species such as [S II] and [O II] show a large degree of intrinsic scatter, spatially. This is likely to be caused by conditions such as stronger density fluctuations in the outer regions where these species dominate. Any inferences extrapolated from spatially-resolved observations involving these species should therefore be interpreted with care. Likewise, our scanned observations of the almost-spherical object DEM L323, show that spatial subsampling of an H II region can show significant variation from the total integrated spectrum, even when the subsampled region includes all ionization zones.

Overall, the spatially-resolved, optical emission-line diagnostics are in good agreement with the current generation of hot star atmospheres for our objects. For O stars, we tested CoStar atmospheres of Schaerer & de Koter (1997), and for WNE stars, the models of Schmutz et al. (1992) and Hamann & Koesterke (1998). In general, the MAPPINGS photoionization models and the observations agree to within $\lesssim 0.2$ dex. The remaining discrepancies may be just as likely to be caused by inaccuracies in the photoionization code as in the stellar atmosphere models. There is also the likelihood that systematic effects in density and geometry, affecting the local ionization parameter, can systematically affect the observed diagnostics.

The primary trend of this remaining disagreement between observations and models is that the nebular models appear to be too hot. This discrepancy is in the opposite sense of that expected from T_e fluctuations (Peimbert 1967). In the two objects with high-quality measurements of [O III]λ4363/5007, the [O III] electron temperature appears to be systematically overpredicted: in DEM L323 by 850 K, and in DEM L199 by 1500 K. The results are also consistent with a similar discrepancy in DEM L243, but the standard deviation in derived T_e for this object is too high to constrain this. There is a similar problem with data quality for DEM L301, in addition to complications with geometry and excitation mechanism. The discrepancy is clear for DEM L323 and DEM L199, however, and may be related to the systematic slight overestimate in the high-ionization species [Ne III]. This problem is most pronounced in [Ne III]/[O III]. Because of the relatively small difference in IP of 5.85 eV required for these two species, the deviation may be due in part to small-scale features in the stellar energy distribution, or the depth of the Ne^{++} edge in the atmospheres. It is interesting that the more highly-resolved WNE energy distribution by Hamann & Koesterke (1998) yields an identical result for [Ne III]/[O III] as that of Schmutz et al. (1992) (Figure 12*i*; the lines cannot be distinguished). Furthermore, the models produced with the Hummer & Mihalas (1970) atmospheres exhibit the same problem. It is unclear whether the overestimated T_e are caused by the stellar atmosphere models or the photoionization codes. A test run with CLOUDY (e.g., Ferland 1998) confirms the result with that code.

As has been found by Sellmaier (1997) and Stasińska & Schaerer (1997), we confirm that the earlier problem in ionizing Ne to Ne^{++} has been resolved in the new generation O star models. Whereas with earlier generation atmospheres the [Ne III]/[O III] ratio was underestimated by ~ 0.6 dex, our models now show an overestimate of $\lesssim 0.2$ dex. As mentioned above, the source of the remaining discrepancy is unclear, and seems unlikely to be caused by an overestimate in the Ne abundance. There does seem to be a hint that the stellar atmospheres for the O7 stars in DEM L243, at least, are slightly too hard. It appears that He is not uniformly ionized to He^+, and S appears to be slightly over-ionized compared to the data, as seen in the ratios of [S III]/[S II] and [S II]/Hα.

We find no evidence of a problem with the ratio [S III]/[S II], as has occasionally been suggested in the past (e.g., Garnett 1989; Dinerstein & Shields 1986). While our models and observations are not always perfectly matched, the discrepancies are not large, and show both over- and underprediction by the models. Our data suggest significant fractions of S^{+3} and perhaps even S^{+4}, as seen in the regions closest to the WR stars in DEM L199 and in the spatial behavior of the $S23$ parameter. Thus for spatially-resolved nebular observations, the behavior of the S lines might be another potentially useful probe of $T_\star$.

DEM L199 is an important test of WNE-w model atmospheres. The dominant stars are Br 33 and Br 34, of spectral type WN3-w, with a possible significant contribution by Br 32 (WC4). The lack of He I $\lambda5876$ emission from either Br 33 or Br 34 suggests that they are hot enough to fully ionize He^0 in their atmospheres. However, peculiarly, there is no evidence of any He II $\lambda4686$ emission from the nebula. This corresponds to a very confined, boundary range of conditions in the stellar atmosphere models, and it is puzzling that both of these stars exhibit these properties. As mentioned above, both the pure He model atmosphere by Schmutz et al. (1992) and the latest generation models by Hamann & Koesterke (1998) yield photoionization models of the H II complex that are in excellent agreement with the observations, and show the same patterns with respect to the data as the CoStar atmospheres. For WR atmospheres that do not produce He^+-ionizing photons, the optical nebular diagnostics are actually quite insensitive to the energy distributions; models from the two different groups produce virtually identical results.

We find that DEM L301 shows excellent agreement with the composite spectrum of a density-bounded, shell H II region and a 70 km s^{-1} shock. The object is not strongly-density bounded, in spite of predictions that the Hα emission of the nebula accounts for only $\sim 20\%$ of the ionizing emission from the stars. The filamentary structure of this extreme shell object suggests that these shock-produced filaments trap the stellar ionizing radiation, producing spectral properties roughly resembling radiation-bounded photoionization. Nevertheless, the majority of ionizing photons are likely to be escaping through the holes between the filaments. This implies that enormous leakage of ionizing radiation can take place without producing signatures of strong density-bounding.

The two objects in our sample with evidence of shock excitation do indeed show spectral diagnostics that agree well with composite models including both photoionization and shock components. DEM L243 (N63 A) has an embedded or superimposed SNR, and its emission-line spectrum is consistent with a shock velocity of ~ 200 km s^{-1}. DEM L301 (N70) shows evidence of a recent SNR impact, and its spectrum is consistent with a lower shock velocity of ~ 70 km s^{-1}. For both objects, the shock velocities agree with kinematic observations. We note that the existence of the shocks in both objects is difficult to discern in the spatially integrated spectra. The higher-velocity shock in DEM L243 shows optical line ratios that are closer to those from photoionization by hot stars, and are therefore easily diluted. However, the lower-velocity shock in DEM L301 has such weak emission in [O III]$\lambda5007$ that line ratios such as $\lambda4363/\lambda5007$ are also extremely diluted in combination with photoionized emission. The historical confusion over the excitation mechanism in DEM L301 demonstrates the subtleties of these effects. Contamination by shock emission clearly decreases the observed value of η' in the spatially integrated spectra. This results in an inferred $T_\star$ that is spuriously high. Given the difficulty in diagnosing the presence of a contaminating shock, this would be an additional uncertainty in the application of η'. $R23$ can also be affected, especially by higher-velocity shocks.

Previous authors (e.g., Skillman 1989; Bresolin et al. 1999) have noted difficulties in using the η' parameter for estimating $T_\star$. In addition to its sensitivity to U, the value of η' also tends to saturate for O stars above a certain $T_\star$. Empirically, η' has a similar a value, around 2, for our O star H II regions, which have dominant stellar spectral types ranging from O3 to O7. While for earlier generations of stellar atmosphere models, the regime of sensitivity to $T_\star$ extended into O star spectral types, we show that for the CoStar atmospheres, η' is an ineffective discriminant for O star $T_\star \gtrsim 40$ kK. Objects dominated by WR stars, however, and O9 – B0 stars, are still clearly differentiated by η'. We also show that, in contrast to spatially resolved observations of, e.g., 30 Dor (Vílchez & Pagel 1988), there is often a strong spatial variation in η', for example in our data for DEM L323 and DEM L243. Finally, we demonstrate that η' is sensitive to nebular morphology, with shell structures having significantly higher values.

Given the limitations of η' as an indicator of $T_\star$, we suggest that examination of the simple line strength of [Ne III]$\lambda3869$ can be an additional useful constraint in estimating $T_\star$. While [Ne III]/Hβ is dependent on metallicity, it nevertheless offers some advantages over η'. In the first instance, it is more sensitive than η' in differentiating O star spectral types. For our photoionization models, [Ne III]/Hβ varies by about 0.75 dex between types O9 and O3, as opposed to 0.35 dex for η'. Unfortunately, the modeled difference between O3 and O7 spectral types is still $\lesssim 0.1$ dex. We note, however, that the spatially integrated data for our O3 nebula, DEM 323, and our O7 nebula, DEM 243, appear better differentiated in [Ne III]/Hβ than η'. This stronger differentiation is supported by data for additional objects from the forthcoming sample of Kennicutt et al. Another advantage of [Ne III]/Hβ is its lower sensitivity to the presence of contaminating shocks, owing to the high IP required for Ne^{++}. This is also demonstrated by our spatially integrated data. Finally, [Ne III]/Hβ is almost independent of nebular morphology, and somewhat less sensitive to U. The primary disadvantage, aside from presumable metallicity sensitivity, is that the modeled values are not in agreement with the data, and hence an empirical calibration is necessary. The observations presented here provide some initial data points for this purpose, suggesting a rough empirical calibration at LMC metallicity given by Table 5.

We have enjoyed discussions of this work with many people, including Paul Crowther, Evan Skillman, Wolf-Rainer Hamann, Henny Lamers, John Mathis, Werner Schmutz, and Bill Blair's SNR lunch group. We are especially grateful to Don Garnett for discussions and comments on the manuscript. Special thanks to Rob Kennicutt and Fabio Bresolin for providing their data in advance of publication, and also to Wolf-Rainer Hamann for providing model WR atmospheres from his group. We are grateful to Mark Allen, Daniel Schaerer, and Grazyna Stasińska for help in sorting out photoionization codes, and also thank Ken Freeman for assistance at the telescope. Finally, thanks to the referee, Jim Kingdon, for helpful comments. Some of this work was carried out by MSO while at the Institute of Astronomy, Cambridge.

Table 1

H II region sample and ionizing stars

DEM	Henize	LH	Star ID	Sp. Type	Reference
DEM L199	N144	LH 58	Br 32	WC4 + O6 V-III	Moffat et al. (1990)
			Br 33	WN3 + OB	Breysacher (1981)
			Br 34	WN3: + B3 I	Breysacher (1981)
			496	O3-4 V	Garmany et al. (1994)
DEM L243	N63 A	LH 83	2	O7 V((f))	Oey (1996a)
			5	O7 If	Oey (1996a)
DEM L301	N70	LH 114	SW3	O3 If*	Oey (1996a)
			NW4	O5: III:e	Oey (1996a)
DEM L323	N180 B	LH 117	LH 117–118	O4: III(f)	Massey et al. (1989)
			LH 117–140	O3-4 (f*)	Massey et al. (1989)
			LH 117–214	O3-4	Massey et al. (1989)

Table 2

Dereddened line intensities for stationary positions[a]

							D199.205							
line (Å)	ap10	err	ap11	err	ap13	err	ap14	err	ap15	err	ap16	err	ap17	err
3727	314.5	15.8	272.0	13.6	216.9	10.9	33.6	1.9	153.7	7.8	212.7	10.8	193.0	9.9
3869	21.6	1.4	29.5	1.6	27.0	1.4	24.4	1.3	22.8	1.5	33.3	2.1	24.4	1.9
4069	3.4	0.9	2.2	0.5	2.3	0.4	0.0	0.6	0.6	0.9	2.4	1.3	2.6	1.5
4076	0.5	0.9	0.9	0.5	0.5	0.4	0.1	0.6	0.0	0.9	0.5	1.3	0.5	1.5
4101	23.5	1.5	23.8	1.3	25.6	1.3	24.8	1.4	23.4	1.5	20.1	1.6	21.6	1.8
4340	45.4	2.3	45.4	2.3	46.1	2.3	46.1	2.3	44.5	2.3	43.5	2.3	42.1	2.4
4363	1.7	0.6	2.4	0.3	2.0	0.2	1.7	0.4	1.9	0.7	1.5	0.8	2.6	1.1
4471	3.6	0.6	3.5	0.5	4.0	0.5	3.8	0.6	2.7	0.5	2.4	0.7	2.9	0.8
4861	100.0	5.0	100.0	5.0	100.0	5.0	100.0	5.0	100.0	5.0	100.0	5.1	100.0	5.1
4959	91.4	4.6	122.9	6.2	117.8	5.9	140.1	7.0	111.8	5.6	128.0	6.4	129.4	6.5
5007	272.7	13.6	367.9	18.4	350.0	17.5	420.8	21.0	338.1	16.9	380.5	19.0	388.0	19.4
5200	1.2	0.6	0.7	0.5	0.2	0.4	0.0	0.6	0.0	0.5	0.0	0.7	0.0	0.8
5755	0.6	0.6	0.6	0.4	0.5	0.2	0.4	0.3	0.7	0.5	1.1	0.8	0.0	0.9
5876	11.3	0.8	12.0	0.7	11.7	0.6	12.5	0.7	12.3	0.8	12.2	1.0	10.1	1.0
6300	5.2	0.6	4.6	0.4	2.6	0.2	0.0	0.4	0.0	0.5	0.0	0.8	0.0	0.9
6312	1.6	0.6	1.5	0.4	1.3	0.2	1.5	0.3	1.2	0.5	2.6	0.8	1.2	0.9
6548	11.6	0.7	9.5	0.5	8.1	0.4	1.4	0.2	5.7	0.4	5.1	0.4	6.9	0.6
6563	285.3	14.3	287.7	14.4	285.2	14.3	286.1	14.3	276.7	13.8	261.9	13.1	274.7	13.7
6584	36.4	1.9	29.2	1.5	24.4	1.2	3.0	0.2	18.6	1.0	16.3	0.9	20.3	1.1
6678	3.7	0.4	3.5	0.3	3.5	0.2	3.9	0.3	3.9	0.4	3.8	0.3	3.6	0.5
6716	52.7	2.7	37.8	1.9	31.2	1.6	0.0	0.2	16.5	0.9	15.6	0.8	24.0	1.3
6731	37.4	1.9	26.7	1.4	22.0	1.1	0.0	0.2	11.2	0.6	11.1	0.6	16.6	1.0
7065	1.9	0.4	2.1	0.2	2.1	0.2	2.1	0.2	2.1	0.3	2.2	0.3	2.1	0.5
7136	10.0	0.6	12.3	0.6	11.1	0.6	10.5	0.6	10.5	0.6	10.7	0.6	11.0	0.7
9069	23.0	1.2	28.2	1.4	24.7	1.2	21.6	1.1	20.6	1.1	20.3	1.1	25.9	1.5
η'	0.8	0.1	0.8	0.1	0.8	0.1	0.0	-0.3	0.9	0.1	1.1	0.2	0.8	0.1
$R23$	6.8	0.6	7.6	0.5	6.8	0.5	5.9	0.4	6.0	0.4	7.2	0.5	7.1	0.5
$S23$	1.71	0.11	1.63	0.11	1.40	0.09	0.73	0.06	1.00	0.07	0.98	0.07	1.31	0.09
c[b]	0.00	0.05	0.00	0.05	0.00	0.05	0.00	0.05	0.11	0.05	0.11	0.05	0.11	0.05

[a]Relative to Hβ.

[b]Adopted reddening correction.

[c]Affected by SNR.

TABLE 2—*continued*

	D199.205		D199.205N120											
line (Å)	ap18	err	ap 9	err	ap10	err	ap11	err	ap12	err	ap13	err	ap14	err
3727	163.1	9.2	230.8	17.1	389.0	19.5	260.6	13.1	259.4	13.0	250.8	12.6	184.6	9.3
3869	30.7	3.3	10.4	8.9	26.8	1.8	23.9	1.6	17.1	0.9	20.4	1.1	23.3	1.3
4069	0.0	3.0	0.0	8.9	2.9	1.2	1.6	1.1	2.3	0.4	1.9	0.5	1.5	0.5
4076	0.6	3.0	2.7	8.9	0.0	1.2	0.0	1.1	0.0	0.4	0.5	0.5	0.4	0.5
4101	17.6	3.1	17.8	9.0	26.2	1.7	23.5	1.6	26.0	1.4	26.0	1.4	25.1	1.3
4340	38.2	3.5	49.6	4.1	47.5	2.5	47.0	2.4	47.9	2.4	48.4	2.4	46.6	2.3
4363	0.6	2.9	0.0	3.3	1.9	0.9	1.6	0.6	1.6	0.2	1.5	0.2	1.5	0.2
4471	2.8	2.0	7.1	5.5	5.1	1.2	4.0	0.7	3.6	0.3	3.9	0.4	4.3	0.4
4861	100.0	5.4	100.0	7.4	100.0	5.1	100.0	5.0	100.0	5.0	100.0	5.0	100.0	5.0
4959	131.0	6.8	74.9	6.6	89.2	4.6	96.4	4.9	77.6	3.9	84.4	4.2	110.3	5.5
5007	387.1	19.5	227.8	12.6	259.6	13.0	284.0	14.2	231.6	11.6	250.8	12.5	331.7	16.6
5200	0.0	2.0	1.5	5.5	1.3	1.1	1.1	0.6	0.9	0.3	0.7	0.3	0.6	0.3
5755	2.5	2.4	0.0	3.3	0.8	0.7	1.0	0.6	0.4	0.2	0.4	0.2	0.1	0.2
5876	12.8	2.4	16.6	3.4	11.4	0.9	11.7	0.8	11.0	0.6	11.8	0.6	12.3	0.6
6300	3.7	2.4	13.5	3.3	5.6	0.8	2.0	0.6	2.8	0.2	2.4	0.3	1.7	0.2
6312	0.0	2.4	1.7	3.3	2.0	0.7	1.1	0.6	1.0	0.2	1.1	0.3	1.1	0.2
6548	5.2	1.1	8.8	1.9	13.0	0.8	9.2	0.6	9.8	0.5	9.5	0.5	6.5	0.4
6563	264.5	13.3	295.1	14.9	292.7	14.6	291.4	14.6	294.4	14.7	308.3	15.4	298.0	14.9
6584	19.6	1.4	23.0	2.2	40.6	2.1	26.7	1.4	29.3	1.5	28.2	1.4	19.3	1.0
6678	4.2	1.1	3.4	1.9	3.0	0.4	3.0	0.5	3.2	0.2	3.5	0.3	3.8	0.2
6716	30.9	1.9	29.8	2.4	53.6	2.7	33.0	1.7	35.5	1.8	32.4	1.6	21.6	1.1
6731	21.3	1.5	20.1	2.1	36.9	1.9	23.1	1.2	24.9	1.3	22.7	1.2	15.1	0.8
7065	2.7	1.0	1.5	1.8	1.8	0.4	2.0	0.5	1.8	0.2	2.0	0.2	2.3	0.2
7136	9.1	1.1	10.5	1.9	10.9	0.7	9.8	0.7	8.3	0.5	9.6	0.5	11.1	0.6
9069	23.0	2.0	26.2	2.4	24.1	1.3	21.4	1.1	21.2	1.1	23.0	1.2	23.7	1.2
η'	0.5	0.1	1.4	0.2	1.0	0.2	0.9	0.1	1.0	0.2	1.1	0.2	0.9	0.2
$R23$	6.8	0.4	5.3	0.5	7.4	0.7	6.4	0.5	5.7	0.5	5.9	0.5	6.3	0.4
$S23$	1.33	0.09	1.42	0.13	1.75	0.11	1.31	0.08	1.35	0.09	1.36	0.09	1.20	0.08
c	0.20	0.05	0.20	0.05	0.11	0.05	0.11	0.05	0.20	0.05	0.29	0.05	0.11	0.05

TABLE 2—*continued*

	D199.205N120										D243.2S			
line (Å)	ap15	err	ap16	err	ap17	err	ap18	err	ap19	err	ap 7	err	ap 6	err
3727	232.5	11.7	184.5	9.5	76.4	4.3	254.2	12.8	163.4	8.4	497.1	25.7	250.9	12.7
3869	23.5	1.4	29.2	2.1	33.5	2.2	31.4	2.0	37.2	2.3	0.0	4.5	6.7	1.5
4069	1.5	0.7	1.4	1.5	0.1	1.4	0.9	1.2	0.4	1.3	4.9	4.5	2.0	1.4
4076	0.0	0.7	0.0	1.5	0.0	1.4	0.0	1.2	0.3	1.3	0.0	4.5	0.0	1.4
4101	26.4	1.5	24.0	1.9	23.1	1.8	24.9	1.8	24.4	1.8	28.6	4.7	26.6	2.0
4340	47.0	2.4	47.0	2.4	48.5	2.6	47.8	2.5	46.5	2.5	53.8	3.2	49.7	2.6
4363	1.7	0.4	2.2	0.6	2.0	0.9	1.5	0.6	2.6	1.0	4.0	1.8	2.6	0.8
4471	4.3	0.5	4.8	0.5	5.0	0.8	4.0	0.6	5.2	0.6	0.0	1.6	3.7	0.6
4861	100.0	5.0	100.0	5.0	100.0	5.1	100.0	5.0	100.0	5.0	100.0	5.2	100.0	5.0
4959	110.1	5.5	138.2	6.9	155.0	7.8	129.1	6.5	154.3	7.7	13.2	1.7	58.1	3.0
5007	330.8	16.5	411.4	20.6	462.3	23.1	384.9	19.3	460.5	23.0	37.7	2.5	175.5	8.8
5200	0.5	0.4	0.0	0.5	0.0	0.7	0.0	0.5	0.0	0.6	0.6	1.6	0.0	0.6
5755	0.4	0.3	0.5	0.4	0.8	0.7	0.8	0.6	0.4	0.5	0.1	0.9	0.0	0.4
5876	11.8	0.7	11.9	0.7	12.5	0.9	11.9	0.9	12.8	0.8	4.9	0.9	10.5	0.7
6300	1.4	0.3	0.6	0.4	0.0	0.7	0.0	0.6	2.3	0.5	3.5	0.9	0.0	0.4
6312	1.2	0.3	1.6	0.4	1.8	0.7	1.5	0.6	1.9	0.5	0.0	0.9	0.5	0.4
6548	7.3	0.4	6.7	0.4	1.0	0.4	5.9	0.5	3.0	0.5	16.5	1.4	7.2	0.5
6563	295.3	14.8	294.1	14.7	286.2	14.3	281.4	14.1	295.4	14.8	320.4	16.1	299.8	15.0
6584	21.9	1.1	19.8	1.0	3.8	0.5	19.6	1.0	16.4	0.9	46.4	2.6	19.9	1.1
6678	3.7	0.3	3.6	0.3	3.1	0.4	3.6	0.4	3.1	0.5	1.9	1.1	3.6	0.4
6716	21.3	1.1	25.6	1.3	0.8	0.4	20.0	1.1	20.2	1.1	47.6	2.6	12.8	0.7
6731	15.2	0.8	18.0	0.9	0.4	0.4	13.9	0.8	13.7	0.8	33.2	2.0	8.8	0.6
7065	2.2	0.3	2.1	0.3	2.1	0.4	2.1	0.4	2.2	0.5	1.0	1.1	1.9	0.4
7136	11.1	0.6	11.9	0.7	11.2	0.7	11.8	0.7	13.2	0.8	2.5	1.1	8.0	0.5
9069	23.6	1.2	24.8	1.3	22.0	1.5	23.1	1.4	28.9	2.0	15.8	1.4	19.9	1.1
η'	1.2	0.2	0.7	0.1	7.7	1.3	1.2	0.2	0.8	0.1	6.7	1.1	3.5	0.6
$R23$	6.7	0.5	7.3	0.5	6.9	0.4	7.7	0.5	7.8	0.5	5.5	0.8	4.8	0.4
$S23$	1.19	0.08	1.30	0.09	0.78	0.07	1.15	0.08	1.35	0.10	1.36	0.09	0.91	0.06
c	0.11	0.05	0.11	0.05	0.00	0.05	0.11	0.05	0.11	0.05	0.08	0.05	0.08	0.05

TABLE 2—*continued*

	D243.2S										D243.5S			
line (Å)	ap 9	err	ap12[c]	err	ap13[c]	err	ap10[c]	err	ap14	err	ap 3	err	ap 4	err
3727	222.0	11.2	179.3	9.3	187.0	9.7	271.1	13.7	341.7	17.2	341.0	17.2	277.4	15.4
3869	9.1	1.1	22.2	2.0	20.2	2.2	17.3	1.4	13.8	1.3	0.7	1.4	4.0	4.8
4069	2.6	1.1	1.6	1.7	1.5	1.9	2.5	1.2	2.5	1.1	2.1	1.4	0.9	4.8
4076	0.7	1.0	0.2	1.7	1.0	1.9	0.1	1.2	0.6	1.1	0.7	1.4	0.2	4.8
4101	26.6	1.7	26.5	2.1	25.8	2.3	26.1	1.7	26.4	1.7	28.9	2.0	24.8	4.9
4340	49.4	2.5	50.3	2.6	48.9	2.6	49.4	2.5	48.9	2.6	50.1	2.6	50.9	2.9
4363	2.0	0.6	4.5	0.7	4.3	1.0	3.3	0.6	3.0	0.9	0.3	0.7	0.0	1.4
4471	2.4	0.4	2.6	0.6	2.3	0.9	2.2	0.4	1.6	0.5	1.5	0.5	3.4	1.3
4861	100.0	5.0	100.0	5.0	100.0	5.1	100.0	5.0	100.0	5.0	100.0	5.0	100.0	5.2
4959	57.2	2.9	113.1	5.7	108.1	5.5	87.1	4.4	69.1	3.5	5.4	0.5	42.2	2.5
5007	172.3	8.6	339.4	17.0	324.3	16.2	260.0	13.0	205.5	10.3	16.7	1.0	131.1	6.7
5200	0.3	0.4	0.0	0.5	0.0	0.8	0.3	0.4	0.6	0.5	0.0	0.5	0.0	1.3
5755	0.3	0.3	0.2	0.5	0.3	0.6	0.3	0.3	0.4	0.3	0.2	0.5	1.2	1.3
5876	8.0	0.5	8.7	0.6	8.5	0.7	6.5	0.4	5.9	0.4	3.4	0.5	10.3	1.4
6300	0.0	0.3	0.0	0.5	0.0	0.6	0.3	0.3	0.2	0.3	2.2	0.5	1.9	1.3
6312	0.4	0.3	0.6	0.5	1.2	0.6	0.3	0.3	0.0	0.3	0.0	0.5	0.0	1.3
6548	8.0	0.5	3.7	0.5	6.4	0.5	7.9	0.5	10.0	0.6	12.7	0.8	10.1	1.3
6563	299.0	15.0	292.8	14.6	303.7	15.2	293.9	14.7	291.9	14.6	309.6	15.5	332.4	16.7
6584	22.2	1.1	16.0	0.9	18.4	1.0	26.1	1.3	32.2	1.7	37.3	1.9	29.1	1.9
6678	3.0	0.3	3.0	0.4	2.8	0.5	2.4	0.3	2.5	0.4	1.0	0.4	3.8	1.2
6716	23.1	1.2	20.2	1.1	23.5	1.3	39.1	2.0	49.8	2.5	44.6	2.3	27.6	1.9
6731	16.5	0.9	15.2	0.9	17.8	1.0	28.2	1.4	35.6	1.8	31.0	1.6	20.8	1.6
7065	1.7	0.3	1.7	0.4	1.6	0.4	1.3	0.3	1.0	0.4	0.7	0.4	2.3	1.2
7136	6.2	0.4	7.4	0.6	7.7	0.6	5.5	0.4	4.9	0.5	2.0	0.4	8.5	1.3
9069	15.1	0.9	18.0	1.0	20.4	1.2	15.0	0.9	13.7	0.8	10.0	0.8	21.0	2.1
η'	1.3	0.2	0.7	0.1	0.7	0.1	0.6	0.1	0.7	0.1	7.2	1.2	2.4	0.4
$R23$	4.5	0.4	6.3	0.4	6.2	0.4	6.2	0.5	6.2	0.6	3.6	0.6	4.5	0.5
$S23$	0.92	0.06	0.98	0.07	1.13	0.08	1.20	0.07	1.33	0.08	1.11	0.07	1.22	0.09
c	0.08	0.05	0.08	0.05	0.00	0.05	0.08	0.05	0.08	0.05	0.16	0.05	0.33	0.05

TABLE 2—*continued*

	D243.5S								D243.30S					
line (Å)	ap 6	err	ap 5	err	ap 7	err	ap 8	err	ap 8	err	ap 9	err	ap10	err
3727	273.5	13.7	173.3	8.7	246.6	12.5	272.8	13.9	367.1	20.1	309.5	16.9	266.6	13.8
3869	7.5	0.5	13.2	1.1	7.5	1.4	7.3	1.9	0.0	5.8	3.2	4.7	8.8	2.5
4069	2.3	0.4	1.1	0.8	1.9	1.4	2.8	1.8	1.7	5.8	2.5	4.7	0.5	2.5
4076	0.3	0.4	1.3	0.8	1.6	1.4	3.1	1.8	0.0	5.8	0.0	4.7	0.0	2.5
4101	27.4	1.4	27.8	1.6	26.6	1.9	27.4	2.3	30.4	6.0	28.5	4.9	30.2	2.9
4340	48.5	2.5	48.4	2.4	47.8	2.5	48.7	2.6	45.5	3.2	49.9	4.1	49.4	2.6
4363	0.9	0.4	1.0	0.2	0.4	0.6	0.9	1.0	0.6	2.2	2.5	3.3	1.8	0.9
4471	2.8	0.3	3.9	0.4	4.1	0.7	3.6	1.0	1.0	2.8	2.7	2.4	4.8	1.0
4861	100.0	5.0	100.0	5.0	100.0	5.1	100.0	5.1	100.0	5.8	100.0	5.5	100.0	5.1
4959	55.0	2.8	81.1	4.1	55.6	2.9	61.8	3.2	0.0	2.9	38.1	3.1	62.7	3.3
5007	165.9	8.3	246.3	12.3	166.0	8.3	182.3	9.2	0.0	3.0	107.4	5.9	188.0	9.5
5200	0.4	0.3	0.1	0.4	0.0	0.7	0.0	0.9	7.8	2.9	3.7	2.4	1.4	1.0
5755	0.4	0.2	0.3	0.2	0.5	0.6	0.3	0.7	1.2	2.7	2.6	2.5	0.8	1.0
5876	8.1	0.4	11.1	0.6	8.7	0.7	9.2	0.8	0.0	2.7	6.8	2.5	9.0	1.1
6300	1.4	0.2	1.0	0.2	0.9	0.6	0.8	0.7	0.0	2.6	1.9	2.5	1.6	1.0
6312	0.5	0.2	0.4	0.2	0.0	0.6	0.0	0.7	0.0	2.7	1.5	2.5	0.8	1.0
6548	8.3	0.4	4.8	0.3	7.9	0.6	7.6	0.9	14.2	1.2	12.1	1.1	7.6	0.6
6563	297.0	14.8	310.2	15.5	297.0	14.9	285.5	14.3	307.5	15.4	313.2	15.7	307.9	15.4
6584	24.1	1.2	13.8	0.7	23.3	1.3	21.4	1.3	48.4	2.6	34.3	2.0	24.6	1.3
6678	2.3	0.2	3.7	0.3	3.3	0.5	3.0	0.8	0.0	1.0	0.7	0.9	1.8	0.4
6716	31.4	1.6	13.9	0.7	25.8	1.4	24.9	1.5	69.5	3.6	36.5	2.0	29.7	1.5
6731	22.0	1.1	10.0	0.5	18.1	1.0	17.8	1.2	50.3	2.7	25.4	1.6	21.2	1.1
7065	1.3	0.1	1.9	0.2	1.6	0.5	1.4	0.8	0.0	1.0	1.0	0.9	1.5	0.4
7136	5.8	0.3	8.2	0.4	6.8	0.6	7.2	0.9	0.8	1.0	6.2	1.0	7.7	0.6
9069	17.6	0.9	18.8	1.0	16.4	1.3	18.1	1.5	0.0	1.1	15.7	1.6	19.5	1.3
η'	1.4	0.2	1.5	0.2	1.5	0.2	1.7	0.3	0.6	0.1	1.9	0.3	1.4	0.2
$R23$	4.9	0.5	5.0	0.4	4.7	0.4	5.2	0.5	3.5	0.6	4.6	0.5	5.2	0.5
$S23$	1.15	0.07	0.90	0.06	1.01	0.07	1.06	0.07	1.16	0.08	1.17	0.08	1.19	0.08
c	0.16	0.05	0.16	0.05	0.08	0.05	0.08	0.05	0.16	0.05	0.08	0.05	0.08	0.05

Table 2—*continued*

	D243.30S													
line (Å)	ap11	err	ap12[c]	err	ap13[c]	err	ap16[c]	err	ap17[c]	err	ap14	err	ap15	err
3727	228.6	12.0	181.2	9.6	269.0	13.7	470.8	23.6	108.7	10.1	201.8	11.1	213.6	12.6
3869	8.7	2.7	17.0	2.5	9.8	1.8	3.9	0.7	13.1	6.1	7.5	3.3	12.7	4.7
4069	2.5	2.7	3.5	2.3	5.6	1.7	3.1	0.7	0.0	6.0	0.7	3.3	0.0	4.7
4076	0.4	2.7	0.0	2.3	0.3	1.7	1.7	0.6	1.2	6.0	1.1	3.3	4.3	4.7
4101	26.7	3.0	22.4	2.6	26.6	2.2	26.7	1.5	22.1	6.1	28.0	3.6	27.2	4.9
4340	49.6	2.9	48.7	2.8	47.9	2.5	49.4	2.5	46.5	3.6	48.4	3.1	50.5	3.4
4363	0.4	1.5	3.9	1.4	1.5	0.6	1.0	0.3	1.8	2.7	2.9	1.9	0.2	2.2
4471	3.5	1.0	3.2	1.5	3.8	0.5	1.8	0.4	2.8	2.2	2.6	8.6	5.6	22.5
4861	100.0	5.1	100.0	5.2	100.0	5.0	100.0	5.0	100.0	5.5	100.0	9.9	100.0	23.1
4959	73.9	3.8	94.5	4.9	62.1	3.1	26.5	1.4	104.5	5.7	55.0	9.0	63.4	22.7
5007	220.5	11.1	285.7	14.4	186.2	9.3	80.0	4.0	306.4	15.5	161.4	11.8	190.9	24.4
5200	1.6	0.9	0.0	1.5	1.5	0.5	1.4	0.4	1.8	2.2	0.5	8.6	0.0	22.5
5755	1.6	0.8	1.6	1.0	1.1	0.4	0.7	0.1	0.4	1.7	1.0	1.0	0.0	1.3
5876	9.5	0.9	8.9	1.1	10.3	0.6	6.8	0.4	11.2	1.8	7.0	1.0	10.0	1.4
6300	0.8	0.8	2.0	1.1	16.8	0.9	7.7	0.4	0.0	1.7	1.6	1.0	0.0	1.3
6312	0.0	0.8	0.9	1.0	1.1	0.4	0.9	0.1	0.0	1.7	0.7	1.0	0.0	1.3
6548	7.1	0.5	4.7	0.7	10.1	0.6	15.9	0.8	3.2	1.1	6.8	0.7	5.6	1.2
6563	295.2	14.8	289.7	14.5	302.8	15.1	320.8	16.0	290.4	14.6	296.0	14.8	300.6	15.1
6584	20.2	1.1	16.5	1.1	31.3	1.6	46.5	2.3	9.2	1.2	22.6	1.3	23.3	1.7
6678	2.6	0.4	2.3	0.7	2.9	0.3	2.3	0.2	3.3	1.1	2.1	0.6	4.2	1.2
6716	21.0	1.1	17.9	1.1	37.2	1.9	43.2	2.2	11.7	1.2	31.5	1.7	28.8	1.9
6731	15.0	0.8	13.0	0.9	37.7	1.9	36.7	1.8	10.2	1.2	22.7	1.3	22.9	1.6
7065	1.5	0.4	1.9	0.7	2.2	0.3	1.4	0.2	1.2	1.1	0.7	0.6	2.1	1.2
7136	7.2	0.5	8.0	0.8	7.1	0.4	5.2	0.3	9.5	1.2	5.3	0.6	7.3	1.2
9069	16.5	1.1	16.6	1.4	14.0	0.7	15.0	0.8	13.4	1.5	13.3	1.7	17.4	2.2
η'	1.3	0.2	0.9	0.1	0.7	0.1	2.9	0.5	0.6	0.1	0.8	0.1	1.0	0.2
$R23$	5.2	0.4	5.6	0.4	5.2	0.5	5.8	0.8	5.2	0.3	4.2	0.5	4.7	0.9
$S23$	0.94	0.06	0.89	0.06	1.24	0.07	1.32	0.08	0.69	0.05	1.01	0.11	1.13	0.27
c	0.16	0.05	0.08	0.05	0.33	0.05	0.16	0.05	0.16	0.05	0.08	0.05	0.08	0.05

Table 2—*continued*

	D301.SW1						D301.SW6							
line (Å)	ap 6	err	ap 5	err	ap 7	err	ap 6	err	ap 7	err	ap 8	err	ap 9	err
3727	543.2	27.3	393.0	19.7	425.1	21.5	589.1	31.3	587.1	29.4	496.6	24.8	451.1	22.6
3869	11.8	1.8	6.6	0.6	14.0	2.6	0.0	7.6	10.9	1.0	10.3	0.9	10.7	0.8
4069	6.2	1.7	2.7	0.6	4.9	2.5	0.9	7.6	6.0	0.9	4.5	0.7	4.0	0.6
4076	0.2	1.7	1.0	0.6	0.5	2.5	7.3	7.6	1.8	0.8	2.1	0.7	1.5	0.5
4101	27.5	2.2	25.6	1.4	25.8	2.8	30.4	7.7	26.5	1.6	26.3	1.5	24.4	1.3
4340	45.8	2.4	46.1	2.3	46.4	2.6	52.6	4.5	47.2	2.4	46.6	2.3	46.0	2.3
4363	0.6	0.8	0.6	0.3	0.0	1.1	5.9	3.7	1.7	0.3	1.5	0.3	0.8	0.4
4471	4.3	1.2	4.1	0.6	3.7	1.0	1.5	3.7	3.6	0.6	3.8	0.6	3.5	0.4
4861	100.0	5.1	100.0	5.0	100.0	5.1	100.0	6.2	100.0	5.0	100.0	5.0	100.0	5.0
4959	25.9	1.8	44.4	2.3	67.8	3.5	13.9	3.8	35.7	1.9	43.7	2.3	41.5	2.1
5007	77.9	4.1	134.3	6.7	207.1	10.4	52.8	4.6	107.9	5.4	132.6	6.7	125.0	6.3
5200	0.7	1.2	0.0	0.5	0.6	1.0	0.9	3.7	0.4	0.5	0.5	0.5	0.3	0.4
5755	1.0	0.6	0.3	0.2	0.2	0.7	1.2	5.2	0.4	0.3	0.8	0.3	0.9	0.2
5876	9.5	0.7	10.9	0.6	11.4	0.9	11.9	5.2	11.3	0.6	12.7	0.7	11.6	0.6
6300	10.4	0.8	1.4	0.2	5.8	0.8	1.1	5.2	6.8	0.4	2.8	0.3	3.0	0.3
6312	0.1	0.6	1.2	0.2	1.9	0.7	0.0	5.2	1.8	0.3	1.6	0.3	1.4	0.2
6548	17.0	1.0	10.8	0.6	11.1	0.7	22.5	2.0	17.0	0.9	15.2	0.8	14.7	0.8
6563	282.6	14.1	293.5	14.7	274.9	13.8	295.4	14.9	285.3	14.3	293.5	14.7	291.9	14.6
6584	49.5	2.5	31.3	1.6	34.5	1.8	50.4	3.0	49.6	2.5	44.7	2.2	43.3	2.2
6678	2.3	0.4	3.0	0.2	3.1	0.4	2.8	1.7	3.1	0.3	3.0	0.3	3.2	0.3
6716	72.0	3.6	33.8	1.7	50.1	2.5	119.4	6.2	81.8	4.1	67.1	3.4	66.7	3.3
6731	50.3	2.6	23.5	1.2	35.0	1.8	83.0	4.5	57.5	2.9	47.4	2.4	47.2	2.4
7065	1.9	0.4	1.8	0.2	1.9	0.4	3.2	1.7	2.0	0.3	2.1	0.3	2.1	0.3
7136	6.7	0.5	8.5	0.5	9.5	0.6	6.3	1.7	9.3	0.6	9.7	0.5	9.4	0.5
9069	17.5	1.2	21.9	1.1	23.6	1.6	11.9	2.8	19.7	1.2	19.5	1.1	22.2	1.1
η'	2.6	0.4	2.9	0.5	1.5	0.2	1.8	0.3	2.0	0.3	1.7	0.3	1.8	0.3
$R23$	6.5	0.9	5.7	0.7	7.0	0.7	6.6	1.0	7.3	1.0	6.7	0.8	6.2	0.8
$S23$	1.84	0.11	1.34	0.09	1.68	0.11	2.44	0.18	2.08	0.12	1.83	0.11	1.92	0.12
c	0.00	0.05	0.00	0.05	0.00	0.05	0.00	0.05	0.00	0.05	0.00	0.05	0.00	0.05

TABLE 2—*continued*

	D301.SW6				D323.C1									
line (Å)	ap10	err	ap11	err	ap13	err	ap 6	err	ap 7	err	ap 8	err	ap 9	err
3727	603.8	30.2	434.0	21.7	348.0	17.5	369.5	18.5	146.5	7.3	119.7	6.0	241.4	12.1
3869	14.0	0.9	9.7	1.1	13.5	1.6	8.7	0.5	14.6	0.8	17.6	0.9	17.1	0.9
4069	5.3	0.7	3.7	1.0	2.5	1.4	1.6	0.3	0.7	0.2	0.7	0.3	1.2	0.3
4076	1.2	0.6	2.1	1.0	0.1	1.4	0.2	0.3	0.1	0.2	0.2	0.3	0.3	0.2
4101	27.6	1.5	25.8	1.6	24.2	1.9	25.0	1.3	25.4	1.3	25.1	1.3	24.9	1.3
4340	48.2	2.4	47.2	2.4	44.3	2.6	44.3	2.2	45.1	2.3	44.5	2.2	44.7	2.2
4363	1.5	0.3	1.5	0.3	1.1	1.4	0.6	0.2	1.4	0.2	1.5	0.2	1.5	0.1
4471	4.1	0.6	3.4	0.6	4.5	1.5	2.9	0.4	4.1	0.5	3.7	0.4	3.7	0.5
4861	100.0	5.0	100.0	5.0	100.0	5.2	100.0	5.0	100.0	5.0	100.0	5.0	100.0	5.0
4959	42.5	2.2	44.5	2.3	84.1	4.5	59.2	3.0	96.4	4.8	108.0	5.4	96.6	4.9
5007	128.8	6.5	134.5	6.7	250.0	12.6	176.4	8.8	288.2	14.4	321.9	16.1	288.5	14.4
5200	0.3	0.5	0.0	0.5	0.0	1.5	0.2	0.4	0.0	0.4	0.0	0.4	0.0	0.5
5755	0.7	0.5	0.5	0.4	0.0	1.3	0.2	0.2	0.0	0.1	0.0	0.1	0.1	0.1
5876	12.1	0.8	12.6	0.7	11.0	1.4	9.4	0.5	12.0	0.6	12.2	0.6	11.4	0.6
6300	4.1	0.5	0.0	0.4	0.0	1.3	0.4	0.2	0.0	0.2	0.0	0.1	0.2	0.1
6312	1.9	0.5	2.2	0.4	0.3	1.3	0.9	0.2	1.0	0.2	1.2	0.1	1.3	0.2
6548	18.6	1.0	13.1	0.7	8.5	0.9	9.5	0.5	3.2	0.2	2.9	0.2	5.0	0.3
6563	295.9	14.8	280.2	14.0	276.9	13.9	289.3	14.5	289.1	14.5	298.0	14.9	283.6	14.2
6584	50.8	2.6	38.5	1.9	23.3	1.4	27.0	1.4	8.2	0.4	7.5	0.4	14.1	0.7
6678	5.1	0.4	3.1	0.3	3.5	0.8	2.5	0.2	3.3	0.2	3.4	0.2	3.1	0.2
6716	77.4	3.9	57.6	2.9	20.5	1.3	22.7	1.1	5.3	0.3	5.6	0.3	13.9	0.7
6731	54.3	2.7	40.4	2.0	13.7	1.0	16.1	0.8	3.7	0.2	4.0	0.2	9.9	0.5
7065	3.7	0.4	2.0	0.3	1.3	0.8	1.5	0.2	1.9	0.1	1.9	0.2	1.8	0.2
7136	11.4	0.7	9.1	0.5	10.2	0.9	8.2	0.4	9.6	0.5	10.0	0.5	10.1	0.5
9069	20.6	1.1	22.3	1.3	26.9	1.6	26.2	1.3	24.1	1.2	24.2	1.2	23.6	1.2
η'	1.9	0.3	1.9	0.3	2.9	0.5	3.7	0.6	3.6	0.6	2.5	0.4	2.2	0.4
$R23$	7.8	1.0	6.1	0.7	6.8	0.6	6.1	0.6	5.3	0.3	5.5	0.3	6.3	0.5
$S23$	2.04	0.12	1.76	0.11	1.28	0.09	1.30	0.09	0.93	0.07	0.94	0.07	1.06	0.08
c	0.00	0.05	0.00	0.05	0.08	0.05	0.08	0.05	0.16	0.05	0.08	0.05	0.16	0.05

TABLE 2—*continued*

	D323.C1						D323.C2							
line (Å)	ap10	err	ap11	err	ap12	err	ap 5	err	ap 6	err	ap 7	err	ap 8	err
3727	327.2	16.4	393.8	19.7	458.9	23.1	584.6	29.4	495.4	24.9	271.9	13.6	270.1	13.5
3869	9.9	0.7	5.2	0.5	7.7	1.7	1.5	2.0	5.7	1.7	10.4	0.7	12.1	0.8
4069	1.7	0.5	1.8	0.4	3.0	1.7	3.9	2.0	2.8	1.6	1.6	0.5	1.1	0.5
4076	0.2	0.4	0.7	0.4	0.3	1.7	0.9	2.0	0.0	1.6	0.1	0.5	0.3	0.4
4101	23.8	1.3	24.4	1.3	23.7	2.0	26.4	2.4	26.2	2.1	25.8	1.4	25.4	1.3
4340	43.9	2.2	44.2	2.2	45.8	2.4	43.8	2.5	44.8	2.3	45.0	2.3	44.2	2.2
4363	1.0	0.2	0.9	0.1	0.8	0.6	1.1	1.1	1.3	0.6	1.0	0.3	1.4	0.3
4471	3.5	0.5	3.7	0.6	3.9	0.9	2.8	0.9	5.0	0.9	4.0	0.5	3.9	0.4
4861	100.0	5.0	100.0	5.0	100.0	5.1	100.0	5.1	100.0	5.1	100.0	5.0	100.0	5.0
4959	63.2	3.2	48.4	2.5	37.8	2.1	16.0	1.2	34.4	1.9	70.2	3.5	76.1	3.8
5007	188.7	9.4	145.2	7.3	111.9	5.7	48.3	2.6	104.2	5.3	209.5	10.5	228.5	11.4
5200	0.3	0.4	0.0	0.5	0.0	0.9	1.3	0.9	0.0	0.8	0.0	0.5	0.2	0.4
5755	0.2	0.2	0.4	0.1	0.4	0.4	0.6	0.7	0.7	0.7	0.4	0.2	0.3	0.2
5876	11.2	0.6	11.5	0.6	10.5	0.7	5.1	0.7	9.4	0.8	11.3	0.6	10.8	0.6
6300	0.2	0.2	0.7	0.1	1.8	0.5	5.4	0.7	0.0	0.7	0.3	0.2	0.6	0.2
6312	1.1	0.2	1.3	0.1	0.5	0.4	1.0	0.7	2.0	0.7	1.2	0.2	1.4	0.2
6548	7.7	0.4	9.4	0.5	10.8	0.6	17.6	1.0	13.5	0.8	6.3	0.3	6.6	0.4
6563	295.6	14.8	304.3	15.2	275.2	13.8	299.2	15.0	283.3	14.2	291.3	14.6	289.6	14.5
6584	22.4	1.1	27.5	1.4	31.6	1.6	50.6	2.6	37.1	1.9	17.7	0.9	18.4	0.9
6678	3.0	0.2	3.2	0.2	2.7	0.4	1.5	0.5	2.5	0.4	3.2	0.2	3.0	0.2
6716	21.6	1.1	26.8	1.3	33.2	1.7	57.7	2.9	30.5	1.6	16.7	0.8	18.4	0.9
6731	15.3	0.8	19.5	1.0	23.7	1.2	40.1	2.1	21.0	1.1	11.8	0.6	13.1	0.7
7065	1.8	0.2	2.0	0.2	1.3	0.4	1.0	0.5	1.7	0.4	1.8	0.1	1.8	0.2
7136	9.2	0.5	10.4	0.5	7.9	0.5	3.8	0.5	7.5	0.5	9.1	0.5	8.9	0.5
9069	23.5	1.2	28.9	1.5	24.1	1.3	19.4	1.1	23.1	1.2	24.8	1.2	22.1	1.1
η'	2.9	0.5	4.4	0.7	4.5	0.7	6.3	1.0	5.6	0.9	2.9	0.5	2.2	0.4
$R23$	5.8	0.6	5.9	0.7	6.1	0.8	6.5	1.0	6.3	0.8	5.5	0.5	5.7	0.5
$S23$	1.19	0.08	1.47	0.10	1.41	0.09	1.66	0.10	1.32	0.09	1.15	0.08	1.09	0.07
c	0.16	0.05	0.16	0.05	0.16	0.05	0.08	0.05	0.16	0.05	0.16	0.05	0.16	0.05

TABLE 2—*continued*

							D323.C2							
line (Å)	ap 9	err	ap10	err	ap11	err	ap12	err	ap13	err	ap 0	err	ap 0	err
3727	261.7	13.1	239.4	12.0	131.6	6.6	161.9	8.1	225.3	11.4	0.0	0.0	0.0	0.0
3869	16.4	0.9	19.7	1.0	21.8	1.2	16.8	1.0	15.3	1.5	0.0	0.0	0.0	0.0
4069	1.3	0.2	1.1	0.3	0.6	0.5	0.8	0.5	0.0	1.3	0.0	0.0	0.0	0.0
4076	0.4	0.2	0.3	0.3	0.5	0.5	0.2	0.5	0.0	1.3	0.0	0.0	0.0	0.0
4101	25.0	1.3	25.0	1.3	25.5	1.4	25.0	1.3	27.2	1.9	0.0	0.0	0.0	0.0
4340	43.9	2.2	44.0	2.2	44.4	2.2	43.7	2.2	44.3	2.3	0.0	0.0	0.0	0.0
4363	1.4	0.2	1.9	0.2	1.9	0.3	1.5	0.2	2.4	0.6	0.0	0.0	0.0	0.0
4471	3.9	0.4	3.8	0.4	4.1	0.5	3.8	0.5	4.2	0.6	0.0	0.0	0.0	0.0
4861	100.0	5.0	100.0	5.0	100.0	5.0	100.0	5.0	100.0	5.0	0.0	0.0	0.0	0.0
4959	90.6	4.5	109.6	5.5	122.0	6.1	102.0	5.1	93.7	4.7	0.0	0.0	0.0	0.0
5007	272.2	13.6	328.5	16.4	364.3	18.2	307.0	15.4	279.6	14.0	0.0	0.0	0.0	0.0
5200	0.1	0.4	0.1	0.4	0.0	0.5	0.0	0.5	0.2	0.6	0.0	0.0	0.0	0.0
5755	0.3	0.1	0.3	0.1	0.1	0.2	0.3	0.1	0.5	0.6	0.0	0.0	0.0	0.0
5876	11.4	0.6	11.6	0.6	12.1	0.6	11.8	0.6	11.8	0.9	0.0	0.0	0.0	0.0
6300	0.7	0.1	0.1	0.1	0.0	0.2	0.0	0.1	0.0	0.6	0.0	0.0	0.0	0.0
6312	1.2	0.1	1.4	0.1	1.5	0.2	1.0	0.1	0.7	0.6	0.0	0.0	0.0	0.0
6548	6.4	0.3	5.6	0.3	3.2	0.2	4.1	0.3	5.2	0.5	0.0	0.0	0.0	0.0
6563	284.4	14.2	298.8	14.9	293.6	14.7	295.1	14.8	295.2	14.8	0.0	0.0	0.0	0.0
6584	18.0	0.9	15.7	0.8	8.5	0.4	11.3	0.6	15.4	0.9	0.0	0.0	0.0	0.0
6678	3.1	0.2	3.3	0.2	3.2	0.2	3.3	0.2	2.6	0.4	0.0	0.0	0.0	0.0
6716	18.3	0.9	15.7	0.8	8.7	0.5	10.3	0.5	17.0	0.9	0.0	0.0	0.0	0.0
6731	13.0	0.7	11.1	0.6	6.2	0.3	7.3	0.4	12.6	0.7	0.0	0.0	0.0	0.0
7065	1.9	0.2	2.0	0.1	2.0	0.2	1.9	0.2	1.8	0.4	0.0	0.0	0.0	0.0
7136	9.7	0.5	11.0	0.6	10.5	0.5	9.9	0.5	10.0	0.6	0.0	0.0	0.0	0.0
9069	23.4	1.2	26.9	1.4	24.1	1.2	26.2	1.3	26.9	1.5	0.0	0.0	0.0	0.0
η'	1.9	0.3	1.9	0.3	1.5	0.2	2.1	0.3	1.9	0.3	0.0	0.0	0.0	0.0
$R23$	6.2	0.5	6.8	0.5	6.2	0.4	5.7	0.4	6.0	0.4	0.0	0.0	0.0	0.0
$S23$	1.13	0.08	1.21	0.09	0.99	0.07	1.09	0.08	1.24	0.09	0.00	0.00	0.00	0.00
c	0.08	0.05	0.08	0.05	0.08	0.05	0.08	0.05	0.00	0.05	0.00	0.00	0.00	0.00

Table 3
Dereddened line intensities for spatially integrated positions[a]

	D199.496W240		D243.2(tot)		D243.2(no SNR)		D301.SW6[b]		D323.140		D323.140N30N		D323.140N30S	
line (Å)	ap24	err	ap 1	err	ap 2	err	ap12	err	ap16	err	ap16	err	ap13	err
3727	185.6	9.4	265.6	13.3	261.2	13.1	539.1	27.0	277.0	13.9	332.0	16.6	256.9	12.9
3869	30.4	2.0	9.8	0.8	8.7	0.8	12.5	1.0	13.5	0.8	10.2	0.8	16.5	1.0
4069	0.2	1.2	4.4	0.7	2.1	0.7	5.0	0.8	1.1	0.5	0.9	0.7	1.2	0.5
4076	1.1	1.2	1.3	0.6	0.7	0.7	1.5	0.7	0.5	0.5	1.0	0.7	0.4	0.5
4101	27.7	1.9	23.9	1.3	24.2	1.4	25.2	1.5	24.8	1.3	24.2	1.4	24.7	1.3
4340	48.3	2.5	45.7	2.3	46.0	2.3	46.4	2.3	44.2	2.2	43.8	2.3	44.5	2.2
4363	1.1	0.7	1.7	0.4	1.5	0.5	1.8	0.3	1.4	0.3	1.1	0.5	1.1	0.2
4471	0.7	0.6	2.0	0.5	1.8	0.6	3.6	0.5	3.3	0.4	3.4	0.6	3.5	0.4
4861	100.0	5.0	100.0	5.0	100.0	5.0	100.0	5.0	100.0	5.0	100.0	5.0	100.0	5.0
4959	125.0	6.3	51.8	2.6	52.7	2.7	43.5	2.2	83.5	4.2	63.1	3.2	90.8	4.6
5007	376.5	18.8	155.4	7.8	158.1	7.9	131.0	6.6	250.2	12.5	188.5	9.4	271.5	13.6
5200	0.0	0.6	0.9	0.5	0.0	0.5	0.1	0.4	0.0	0.4	0.0	0.6	0.2	0.4
5755	0.5	0.4	0.6	0.3	0.5	0.3	0.6	0.3	0.1	0.2	0.7	0.4	0.1	0.2
5876	9.6	0.7	8.8	0.5	9.1	0.6	12.1	0.7	11.2	0.6	11.4	0.7	11.4	0.6
6300	0.0	0.5	13.0	0.7	1.9	0.3	3.1	0.3	0.0	0.2	0.2	0.4	0.1	0.2
6312	0.7	0.4	0.5	0.3	0.4	0.3	1.4	0.3	1.0	0.2	0.9	0.4	1.1	0.2
6548	5.8	0.5	9.2	0.6	7.7	0.7	14.7	0.8	7.0	0.4	7.8	0.4	6.2	0.3
6563	272.0	13.6	299.4	15.0	295.6	14.8	285.5	14.3	300.9	15.0	303.1	15.2	297.7	14.9
6584	18.7	1.0	27.6	1.4	23.2	1.3	43.6	2.2	19.2	1.0	23.8	1.2	17.6	0.9
6678	3.0	0.4	2.8	0.5	2.9	0.6	3.2	0.3	3.0	0.2	3.1	0.3	3.2	0.2
6716	22.8	1.2	36.3	1.9	22.0	1.2	67.7	3.4	18.2	0.9	20.5	1.0	16.8	0.8
6731	15.4	0.9	35.3	1.8	16.8	1.0	47.8	2.4	12.8	0.7	14.6	0.8	11.8	0.6
7065	2.0	0.4	1.6	0.4	1.5	0.5	2.3	0.3	1.8	0.2	1.4	0.2	2.0	0.1
7136	9.9	0.6	6.6	0.5	7.4	0.6	9.5	0.5	9.7	0.5	8.8	0.5	10.1	0.5
9069	20.8	1.9	17.0	1.1	18.5	1.2	19.2	1.1	25.1	1.4	26.2	1.4	24.8	1.3
η'	0.7	0.1	1.1	0.2	2.1	0.3	1.8	0.3	2.4	0.4	3.4	0.6	2.1	0.4
$R23$	6.9	0.4	4.7	0.5	4.7	0.5	7.1	0.9	6.1	0.5	5.8	0.6	6.2	0.5
$S23$	1.11	0.08	1.31	0.08	1.04	0.07	1.83	0.11	1.19	0.08	1.27	0.09	1.15	0.08
c	0.11	0.05	0.08	0.05	0.08	0.05	0.07	0.05	0.16	0.05	0.16	0.05	0.16	0.05

[a]Relative to Hβ.

[b]Spatial integration over stationary position.

Table 4
KBFM H ii regions

Object	Alt. ID	Sp. Type	symbol	Reference[a]
		Galaxy		
S212		O7 f	3	HM90
S237		B0 V	4	HM90
M42	NGC 1976	O7	3	Oudmaijer et al. (1997)
S255	IC 2162	B0 V	4	HM90
S271		B0 V	4	HM90
S288		O9: V	4	HM90
RCW 5	S298	WN4	1	Esteban et al. (1993)
RCW 8	S305	B0 V	4	HM90
S307		B0 V	4	HM90
RCW 48	NGC 3199	WN5	1	Esteban et al. (1993)
S148		B0 V	4	HM90
S152		O9 V	4	HM90
S156	IC 1470	O6.5 V:	3	HM90
		LMC		
DEM L34	N11 B	O3	2	Parker et al. (1992)
DEM L152	N44	O5	3	Oey & Massey (1995)
DEM L174	N138 D,B	WN4p	1	Breysacher (1981)
DEM L192	N51 D	WC5, O4 III	1	Oey & Smedley (1998)
DEM L231	N57 C	WN4	1	Breysacher (1981)
DEM L263	30 Dor	WN4.5	1	Massey & Hunter (1998)

[a]HM90 = Hunter & Massey (1990)

Table 5
Empirical calibration of $T_\star$ diagnostics[a]

Sp. type	log [Ne III]λ3869/Hβ	log η'
WR	> -0.6	< 0.2
O3 – O4	–0.9 to –0.6	...
O5 – O8	> 0, to –0.9	...
O9 and later	0	> 1.0

[a]For LMC metallicity, based on Figure 14.

REFERENCES

Ali, B., Blum, R. D., Bumgardner, T. E., Cranmer, S. R., Ferland, G. J., Haefner, R. I., & Tiede, G. P., 1991, PASP, 103, 1182
Anders, E. & Grevesse, N., 1989, Geochim. Cosmochim. Acta, 53, 197
Baldwin, J. A., Ferland, G. J., Martin, P. G., Corbin, M. R., Cota, S. A., Peterson, B. M., & Slettebak, A., 1991, ApJ, 374, 580
Bresolin, F., Kennicutt, R. C., & Garnett, D. R., 1999, ApJ, 510, 104
Breysacher, J., 1981, AAS, 43, 203
Christensen, T., Petersen, L, & Gammelgaard, P., 1997, AA, 322, 41
Chu, Y-H. & Kennicutt, R. C., 1988, AJ, 95, 1111
Chu, Y-H. & Mac Low, M-M., 1990, ApJ, 365, 510
Crowther, P. A., 1999, in *Wolf-Rayet Phenomena in Massive Stars and Starburst Galaxies,* IAU Symp. 193, K. A. van der Hucht, G. Koenigsberger, & P. R. J. Eenens, eds., (San Francisco: ASP), in press
Crowther, P. A., Pasquali, A., De Marco, O., Schmutz, W., Hiller, D. J., & de Koter, A., 2000, AA, in press
Davies, R. D., Elliott, K. H., & Meaburn, J., 1976, Mem. RAS, 81, 89
Díaz, A. I. & Pérez-Montero, E., 1999, MNRAS, in press
Dickel, J. R., Milne, D. K., Junkes, N., & Klein, U., 1993, AA, 275, 265
Dinerstein, H. L. & Shields, G. A., 1986, ApJ, 311, 45
Dopita, M. A., 1979, ApJS, 40, 455
Dopita, M. A., Ford, V. L., McGregor, P. J., Mathewson, D. S., & Wilson, I. R., 1981, ApJ, 250, 103
Dopita, M. A. & Sutherland, R. S., 1995, ApJ, 455, 468
Dopita, M. A. & Sutherland, R. S., 1996, ApJS, 102, 161
Esteban, C., Smith, L. J., Vílchez, J. M., & Clegg, R. E. S., 1993, AA, 272, 299
Ferland, G. et al. , 1995, in *The Analysis of Emission Lines,* R. Williams & M. Livio, eds., (Cambridge: Cambridge Univ. Press), 83
Garmany, C. D., Massey, P., & Parker, J. W., 1994, AJ, 108, 1256
Garnett, D. R., 1989, ApJ, 345, 282
Garnett, D. R., 1999, in *New Views of the Magellanic Clouds,* IAU Symp. 190, Y.-H. Chu, N. Suntzeff, J. Hesser, & D. Bohlender, eds., (San Francisco: ASP), in press
Garnett, D. R. & Kennicutt, R. C., 1994, ApJ, 426, 123
Gräfener, G., Hamann, W.-R., Hillier, D. J., & Koesterke, L., 1998, AA, 329, 190
Hamann, W-R. & Koesterke, L., 1998, AA, 333, 251; HK98
Hamuy, M., Walker, A. R., Suntzeff, N. B., Gigoux, P., Heathcote, S. R., & Phillips, M. M., 1992, PASP, 104, 533
Hummer, D. G. & Mihalas, D. M., 1970, MNRAS, 147, 339
Hunter, D. A. & Massey, P., 1990, AJ, 99, 846
Henize, K. G., 1956, ApJS, 2, 315
Kennicutt, R. C., Bresolin, F., French, H., & Martin, P., in preparation (KBFM)
Kingsburgh, R. L. & Barlow, M. J., 1995, AA, 295, 171
Kurucz, R. L., 1991, in Stellar Atmospheres: Beyond Classical Models, L. Crivellari, I. Hubeny, & D. G. Hummer, eds., NATO ASI Series C, Vol. 341, 441
Lasker, B., 1977, ApJ, 212, 390
Levenson, N. A., Kirshner, R. P., Blair, W. P., & Winkler, P. F., 1995, AJ, 110, 739
Liu, X-W., Danziger, J., 1993, MNRAS, 263, 256.
Lucke, P. B. & Hodge, P. W., 1970, AJ, 75, 171
Massey, P., Garmany, C. D., Silkey, M., & DeGioia-Eastwood, K., 1989, AJ, 97, 107
Massey, P. & Hunter, D. A., 1998, ApJ, 493, 180
Massey, P., Lang, C. C., DeGioia-Eastwood, K., & Garmany, C. D., 1995, ApJ, 438, 188
Mathewson, D. S., Ford, V. L., Dopita, M. A., Tuohy, I. R., Long, K. S., Helfand, D. J., 1983, ApJS, 51, 345
Mathis, J. S., 1985, ApJ, 291, 247
McCall, M. L., Rybski, P. M., & Shields, G. A., 1985, ApJS, 57, 1
McGaugh, S. S., 1991, ApJ, 380, 140
Moffat, A. F. J., Niemela, V. S., & Marraco, H. G., 1990, ApJ, 348, 232
Oey, M. S., 1996a, ApJ, 465, 231
Oey, M. S., 1996b, ApJ, 467, 666
Oey, M. S. & Kennicutt, R. C., 1993, ApJ, 411, 137
Oey, M. S. & Kennicutt, R. C., 1997, MNRAS, 291, 827
Oey, M. S. & Massey, P., 1995, ApJ, 452, 210
Oey, M. S. & Shields, J. C., 2000, ApJ, in preparation (Paper II)
Oey, M. S. & Smedley, S. A., 1998, AJ, 116, 1263
Osterbrock, D. E., 1989, *Astrophysics of Gaseous Nebulae and Active Galactic Nuclei,* (Mill Valley: University Science Books)
Oudmaijer, R. D., Drew, J. E., Barlow, M. J., Crawford, I. A., & Proga, D., 1997, MNRAS, 291, 110
Parker, J. W., Garmany, C. D., Massey, P., & Walborn, N. R., 1992, AJ, 103, 1205
Peimbert, M., 1967, ApJ, 150, 825
Peimbert, M. & Costero, R., 1969, Bol. Obs. Tonantzintla y Tacubaya, 5, 2
Peimbert, M., Sarmiento, A., & Fierro, J., 1991, PASP, 103, 815
Pagel, B. E. J., Edmunds, M. G., Blackwell, D. E., Chun, M. S., & Smith, G., 1979, MNRAS, 189, 95
Rosado, M., Georgelin, Y. P., Georgelin, Y. M., Laval, A., & Monnet, G., 1981, AA, 97, 342
Savage, B. D. & Mathis, J. S., 1979, ARAA, 17, 73
Schaerer, D. & de Koter, A., 1997, AA, 322, 598
Schmutz, W., 1997, AA 321, 268
Schmutz, W. & de Marco, O., 1999, in *Wolf-Rayet Phenomena in Massive Stars and Starburst Galaxies,* IAU Symp. 193, K. A. van der Hucht, G. Koenigsberger, & P. R. J. Eenens, eds., (San Francisco: ASP), in press
Schmutz, W., Leitherer, C., & Gruenwald, R., 1992, PASP, 104, 1164; SLG92
Sellmaier, F. H., Yamamoto, T., Pauldrach, A. W. A., & Rubin, R. H., 1996, AA, 305, L37
Shull, P., 1983, ApJ, 275, 592
Simpson, J. P., Colgan, S. W. J., Rubin, R. H., Erickson, E. F., Haas, M. R., 1995, ApJ, 444, 721
Simpson, J. P., Rubin, R. H., Erickson, E. F., & Haas, M. R., 1986, ApJ, 311, 895
Skelton, B. P., Waller, W. H., Geiderman, R. F., Brown, L. W., Woodgate, B. E., Caulet, A., & Schommer, R. A., 1999, PASP, 111, 465
Skillman, E. D., 1989, ApJ, 347, 883
Smith, R. C. & MCELS Team, 1998, PASA, 15, 163
Stasińska, G. & Schaerer, D., 1997, AA, 322, 615
Stevenson, C. C., 1994, MNRAS, 267, 904
Stone, R. P. S. & Baldwin, J. A., 1983, MNRAS, 204, 347
Sutherland, R. S. & Dopita, M. A., 1993, ApJS, 88, 253
Vílchez, J. M. & Pagel, B. E. J., 1988, MNRAS, 231, 257
Walter, D. K., Dufour, R. J., & Hester, J. J., 1992, ApJ, 397, 196
Westerlund, B. E. & Mathewson, D. S., 1966, MNRAS, 131, 371